Report
R-19-12
June 2019

Modelling of concrete degradation – Hydro-chemo-mechanical processes

Report for the safety evaluation SE-SFL

Andrés Idiart
Marcelo Laviña
Emilie Coene

SVENSK KÄRNBRÄNSLEHANTERING AB

SWEDISH NUCLEAR FUEL
AND WASTE MANAGEMENT CO

Box 3091, SE-169 03 Solna
Phone +46 8 459 84 00
skb.se

SVENSK KÄRNBRÄNSLEHANTERING

ISSN 1402-3091
SKB R-19-12
ID 1590478

June 2019

Modelling of concrete degradation – Hydro-chemo-mechanical processes

Report for the safety evaluation SE-SFL

Andrés Idiart, Marcelo Laviña, Emilie Coene

Amphos 21 Consulting S. L.

Summary

In a previous work, a study of concrete degradation in the BHK vault of the proposed repository concept for the SFL repository was conducted based on 2D and 3D reactive transport modelling. The models, implemented in iCP, encompassed fluid flow, solute transport, and chemical reactions. The main conclusions of that work were that the main process that is expected to drive the degradation of the concrete barriers is calcium leaching.

It is well-known that the dissolution of cement paste hydrates by calcium leaching affects not only porosity and transport properties (hydraulic conductivity, diffusion coefficient), but also the mechanical behaviour of the cementitious systems. Chemically-induced damage can decrease the mechanical performance of the barriers, both in terms of stiffness and strength.

To study these coupled processes, a hydro-chemo-mechanical (HCM) model is developed and implemented in iCP, starting from the previous reactive transport models. The HCM model is used to analyse the effect of calcium leaching on the mechanical stability of the BHK vault, studied with 2D models of a cross-section. A range of sensitivity cases is used to evaluate the influence of mechanical boundary conditions and material parameters on the results.

In addition, the effect of a sulphate-rich groundwater potentially reaching the repository on the mechanical stability of the system is also assessed with the HCM model. To this end, the model for calcium leaching is extended to account for external sulphate attack, where expansions may rise due to precipitation of sulphate-bearing minerals in the cement matrix.

Sammanfattning

Betongdegradering i bergssalen BHK, i det föreslagna förvarskonceptet för SFL, har tidigare studerats med 2D och 3D reaktiv transportmodellering. Modellerna, implementerade i iCP, omfattade vätskeflöde, transport av lösta ämnen och kemiska reaktioner. Den huvudsakliga slutsatsen från det arbetet var att den process som framförallt förväntas leda till nedbrytningen av betongbarriärerna är kalciumutlakning.

Det är välkänt att upplösningen av cementhydrater genom kalciumutlakning inte bara påverkar cementkonstruktioners porositet och transportegenskaper (hydraulisk konduktivitet, diffusionskoefficient) utan även deras mekaniska egenskaper. Denna kemiska process skadar betongbarriärer och sänker deras mekaniska prestanda, både avseende styvhet och styrka.

För att studera dessa kopplade processer utvecklas och implementeras en hydrokemomekanisk (HCM)-modell i mjukvaran iCP, med utgångspunkt från tidigare reaktiva transportmodeller. HCM-modellen används för att analysera effekten av kalciumutlakning på BHK-salens mekaniska stabilitet, där ett tvärsnitt av salen modelleras i 2D. Resultatens känslighet mot mekaniska randvillkor och materialparametrar har utvärderats i en serie beräkningsfall.

HCM-modellen har dessutom använts för att utvärdera hur systemets mekaniska stabilitet påverkas av sulfatrikt grundvatten, som potentiellt kan nå förvaret. För detta ändamål utvidgas modellen för kalciumutlakning till att ta hänsyn till yttre sulfatangrepp, där materialexpansion kan uppstå på grund av utfällning av sulfatmineraler i cementmatrisen.

Contents

1 Introduction

SKB plans to dispose of long-lived low and intermediate level waste in a deep geological repository called SFL. Possible repository concepts for SFL have been evaluated and Elfwing et al. (2013) proposed a repository concept to be analysed in an evaluation of post-closure safety (SE-SFL). This report focusses on the repository concept proposed for metallic waste, which relies on extensive use of cementitious materials for constructing the engineered barrier system.

The long-lived low and intermediate level waste from the nuclear power plants consists of neutron-irradiated components and control rods. The total quantity of long-lived waste planned for SFL is estimated to approximately 16 000 m^3, of which about one third originates from the nuclear power plants. The remainder comes from AB SVAFO and Studsvik Nuclear AB, who manage the legacy waste and the waste from hospitals, industry and research.

In the proposed concept (Elfwing et al. 2013), SFL is considered as a deep geological repository with two storage vaults:

- one vault for the metallic waste from the nuclear power plants (BHK), and
- one vault for legacy waste from AB SVAFO and Studsvik Nuclear AB (BHA).

The vault for the metallic waste (BHK) is planned to be backfilled with concrete, which acts as a barrier against groundwater flow and contributes to a low diffusion rate and high sorption of many radionuclides. The concrete also creates an alkaline environment in the repository vault, reducing the corrosion rate of the steel and limiting the release rate of radionuclides. Over time, the concrete barrier will however transform and its ability to retain radionuclides will be affected. In order to assess the potential of the repository concept it is therefore essential to be able to simulate the evolution of concrete properties, under repository conditions and considering long time scales.

Individual processes related to chemical and physical degradation of concrete have been intensively studied in concrete technology since the 1970's and are relatively well understood when studied independently from each other. Degradation processes are however interdependent and need to be considered simultaneously in order to improve the reliability of predictive simulations of concrete evolution. This requires considerable additional efforts.

The present work aims to address concrete degradation and long-term performance of the BHK vault of he SFL repository by advanced hydro-chemo-mechanical models. These models include groundwater flow, solute transport, chemical reactions within the concrete barriers, and chemo-mechanical processes to predict physical degradation of the concrete barriers (hydraulic, transport, and mechanical properties). Reactive transport models of the BHK vault have been already implemented in iCP (Nardi et al. 2014) in previous work (Idiart and Shafei 2019). iCP is a software interface between Comsol Multiphysics and PhreeqC. In the present study, the two-dimensional reactive transport models of a cross-section of the BHK vault are extended to include chemo-mechanical couplings. In particular, the effect of calcium leaching on the mechanical integrity of the BHK vault is explored. This degradation mechanism was identified as the most plausible (Idiart and Shafei 2019). In addition, the potential impact of sulphate-rich groundwater on the development of ettringite and subsequent mechanical degradation is also addressed. In this case, calcium leaching and sulphate attack act simultaneously and need to be treated in a single numerical model.

1.1 The BHK vault

The proposed design of the concrete vault (BHK) of the SFL repository has been described elsewhere (Grahm et al. 2013 and Elfwing et al. 2013). The main components of the engineered barrier system are shown in Figure 1-1 and Figure 1-2. The waste is segmented, after which the parts are deposited in steel tanks and stabilized with grout. The steel tanks are emplaced in compartments of reinforced concrete with a thickness of ~0.5 m. The volume outside the concrete compartments will be backfilled with concrete.

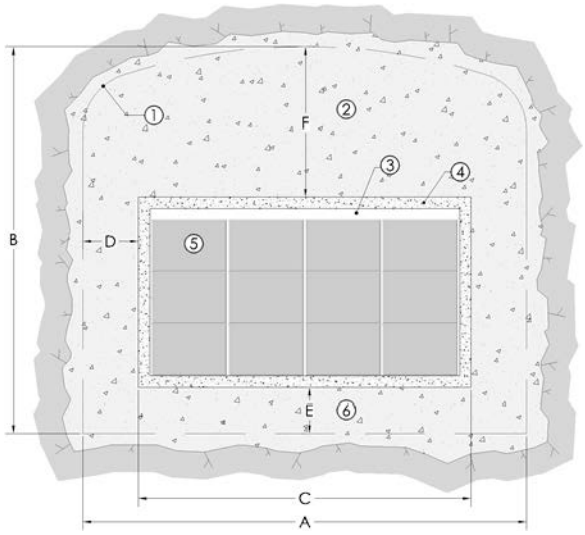

Figure 1-1. *Schematic cross-sectional layout of the BHK vault for metallic waste (from Elfwing et al. 2013). Legend: 1. Theoretical tunnel contour. 2. Concrete backfill. 3. Grout. 4. Concrete structure. (0.5 m). 5. Steel tanks. 6. Concrete. Approximate dimensions: A = 20.6 m, B = 19.6 m, C = 15 m, D = 2.8 m, E = 2.4 m, F = 8.8 m.*

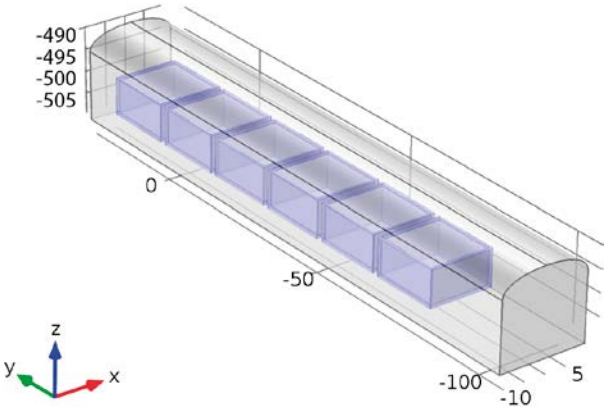

Figure 1-2. *Schematic view of the BHK vault showing the six waste compartments (in blue) and the concrete backfill (light grey). Dimensions are in meters.*

1.2 Key outcomes from reactive transport modelling of concrete degradation in SFL

Idiart and Shafei (2019) studied concrete degradation in the BHK vault as a result of the interaction with groundwater using reactive transport models. The goal was to investigate the long-term chemically-driven degradation of concrete under in-situ conditions for the proposed repository concept for the SFL repository. Models with geometry representations in 2D and 3D considered coupled groundwater flow, solute transport, and chemical reactions. The main source of coupling between chemical and physical processes was the feedback between porosity and mineral dissolution/precipitation.

A Base Case was considered, where concrete degradation was simulated in a cross-section of the BHK vault using a 2D reactive transport model. In addition, a number of sensitivity cases were solved to evaluate the influence of various assumptions on the results. The sensitivity cases considered the:

- Type of boundary conditions used for the fluid flow and solute transport.
- Treatment of concrete and waste domains as homogeneous or heterogeneous porous media.
- Chemical composition of inflow groundwater.
- Coupling between physical and chemical processes (coupled versus non-coupled scenarios).
- Initial concrete chemical setup and mineral assemblage of the domains (full and simplified chemistry cases).

In summary, the main concrete degradation process is driven by leaching of calcium which leads to the gradual dissolution of the main cement hydrates. The alkalis are leached relatively fast, followed by portlandite dissolution. The consumption of portlandite is much slower and is mainly driven by diffusion, due to the slow groundwater flow. Once portlandite is leached at a given region, C-S-H starts to degrade. Calcite formation due to carbonate-rich groundwater is the main secondary mineral that forms, limiting the local increase in porosity to a maximum of ~0.25 after complete degradation.

For all the considered simulation cases the rate of degradation is shown to be very slow, with limited impact even after 100 000 years. This is due to the limited flow of water into the repository, together with a low initial diffusion coefficient of the concrete backfill. Concrete degradation was also simulated using 3D reactive transport models at the compartment-scale and at the entire vault-scale. Overall, the results compare relatively well with the respective 2D model. However, due to higher and heterogeneous Darcy velocities in the 3D models compared to the 2D cases, faster chemical degradation is predicted. After 50 000 years, portlandite dissolution is faster in the compartment-scale model, by a factor of two, compared to the corresponding 2D model. The compartment- and vault-scale models lead to similar conclusions regarding the driving degradation processes.

2 Objectives

The goal of the present work is to evaluate the long-term degradation of concrete in BHK from a chemical and physical point of view, by means of numerical modelling. Both the chemical and mechanical stability of the system is in focus, and models consider simultaneous effects of mechanical loads and chemically-driven degradation processes. Long-term chemical degradation of the concrete barriers in the BHK vault has been studied using reactive transport models in Idiart and Shafei (2019). These models are further developed by considering the coupling between chemical degradation and mechanical behaviour. The objectives of the work are listed below.

- Implementation of a mechanical model in Comsol Multiphysics (Comsol) of the system comprised by the BHK vault and the surrounding rock.
- Implementation of the regularized mechanical damage model by Mazars (1986) in Comsol to allow the study of failure and post-failure situations.
- Implementation of a chemical-damage model to study the impact of mineral precipitation and dissolution processes on mechanical properties.
- Implementation of an expansion model to represent sulphate attack, i.e. expansions due to ettringite precipitation.

The focus is on the calcium leaching degradation process (see Section 1.2). However, the potential of sulphate attack due to sulphate rich waters is also explored.

3 Literature review of chemo-mechanical models of concrete degradation

3.1 Degradation by calcium leaching

3.1.1 Physical and chemical processes

The interaction of groundwater with underground concrete structures leads to a gradual leaching of calcium from the cement paste. Calcium leaching is a very slow process by which part of the cement hydrates are dissolved. First, the readily soluble alkalis in the cement porewater are released to the groundwater. This does not affect the mechanical stability of the material. Second, the calcium in solution start to be leached, causing a gradual dissolution of the portlandite to maintain equilibrium with the porewater. Dissolution of ettringite, AFm phases, and C-S-H decalcification follow (Adenot and Buil 1992, Faucon et al. 1996). Degradation fronts with mineral zonation are developed, as shown in Figure 3-1. The degradation depth as well as the cumulative amount of calcium leached are proportional to the square root of time when diffusive transport prevails (Le Bescop and Solet 2006, Nguyen et al. 2007a).

Severe portlandite dissolution and C-S-H decalcification can induce a substantial increase in porosity, permeability, and diffusivity (Yokozeki et al. 2004, Haga et al. 2005, Babaahmadi 2015). and a decrease in the mechanical properties such as compression strength and Young's modulus (Le Bellégo et al. 2003, Heukamp et al. 2005, Nguyen et al. 2007a, Babaahmadi et al. 2015). The calcium leaching rate obviously depends on the chemical composition of groundwater.

3.1.2 Modelling damage induced by calcium leaching

Numerous models have been proposed in the literature to study the impact of calcium leaching on the mechanical properties of cementitious materials. An exhaustive analysis of each of these models is out of the scope of this study.

Table 3-1 summarizes the main features of these models. Coupling between calcium leaching and mechanical behaviour requires taking the following processes into account:

1. Dissolution of cement hydrates due to chemical disequilibrium.
2. Transport of dissolved species out from the system.
3. A chemical damage model to account for the impact of the dissolution on the mechanical properties.
4. A mechanical model of concrete to account for the impact of mechanical loads.

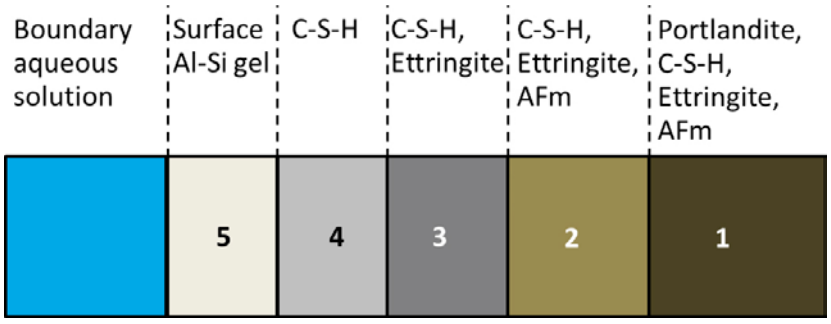

Figure 3-1. *Degradation fronts illustration of the different degradation fronts in a hardened cement paste (from Sidborn et al. 2014).*

The first two processes have been considered in most of the existing models as a simple non-linear diffusion-reaction equation. In some cases, an advective term is added to the equation. In the present study, and similar to Stora et al. (2010), a reactive transport framework is used (Idiart and Shafei 2019). The advantage of using reactive transport modelling is that cement chemistry is considered with a more sophisticated geochemical model.

The effect of the dissolution process on the mechanical properties is in most cases considered through a chemical damage parameter (d_c). This non-dimensional scalar parameter, varying between 0 and 1, is a measure of the level of chemical degradation due to calcium leaching. Isotropic damage is typically considered in all models. Several models are proposed to define chemical damage, although most of these rely upon an empirical function that depends on the calcium concentration in the pore solution. However, different empirical functions are used by each author, see e.g. Figure 3-2 (top) from Gérard et al. (1998), or Hu et al. (2014). These models are limited to the case where the initial state is governed by portlandite, i.e. not including the alkalis Na and K. This is because the Ca concentration in pore solution is not monotonically decreasing with the leaching process, Figure 3-2 (bottom). On the contrary, Ca concentration is reduced in the presence of alkalis, increases substantially when the latter are leached, and then gradually decreases with the leaching process. For a large concrete structure, as in the BHK vault, alkalis are present even in the long-term and therefore their effect on Ca concentration may last for a prolonged period of time. In such a case, Ca in pore solution does not appear to be a suitable choice for the state variable governing chemical damage in a reactive transport framework.

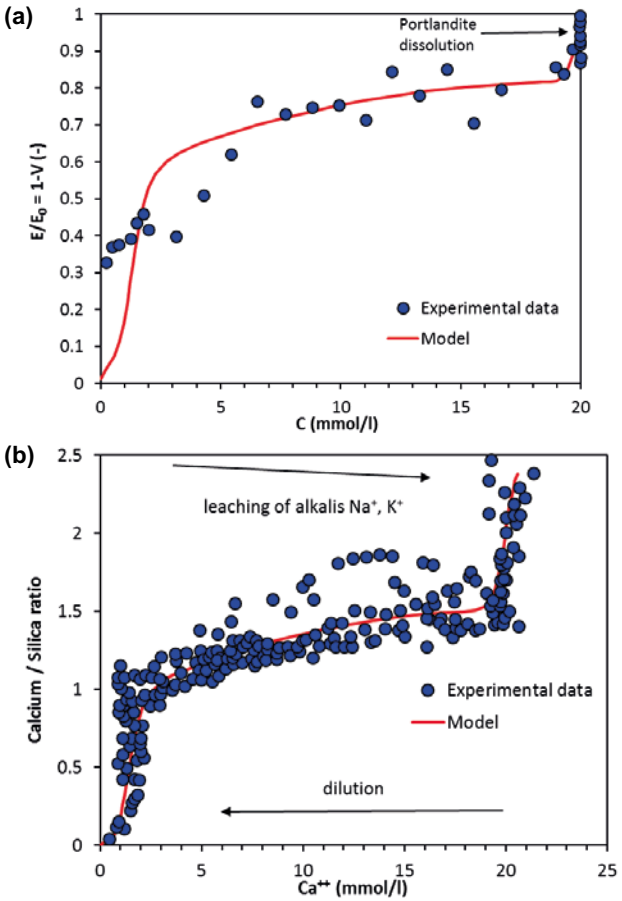

Figure 3-2. *(a) Chemical damage parameter (V) evolution as a function of calcium concentration in pore solution: proposed empirical function and experimental results from micro-hardness measurements (adapted from Gérard et al. 1998). (b) Experimental data of the calcium to silica ratio (C/S) in the solid phase as a function of calcium concentration in pore solution (adapted from Gérard et al. 2002).*

Stora et al. (2010) proposed to calculate the evolution of the elastic properties of concrete during calcium leaching by treating the material as a composite with several solid phases. These phases are characterized by the volume fractions of the different cement hydrates. To this end, an advanced multi-scale homogenization model was proposed. From the resulting effective elastic properties, a chemical damage can be easily calculated. One of the advantages of this model is that it overcomes the above-mentioned problem of using aqueous concentrations as a state-variable for chemical damage. More details about this model are presented in Section 5.2.

In most of the models, chemical damage is used to reduce the stiffness tensor, as with traditional damage mechanics (Gérard et al. 1998, Le Bellégo et al. 2003, Cuomo and Nicolasi 2006, Torrenti et al. 2008):

$$\boldsymbol{E} = (1 - d_c) \cdot \boldsymbol{E_0} \tag{3-1}$$

where $\boldsymbol{E_0}$ and $\boldsymbol{E}$ (GPa) are the initial and damaged stiffness tensors. These tensors are fully defined when the material is isotropic by two parameters: Young's modulus E (MPa) and Poisson's ratio ν (–). The stiffness tensor relates the strain tensor ($\boldsymbol{\varepsilon}$) to the stress tensor ($\boldsymbol{\sigma}$, MPa):

$$\boldsymbol{\sigma} = \boldsymbol{E}\colon \boldsymbol{\varepsilon} \tag{3-2}$$

Other models use the chemical damage to update additional mechanical parameters, which are needed for more sophisticated mechanical models. Some of these models encompass damage mechanics, plasticity, and creep (i.e. time-dependent deformation), see e.g. Cuomo and Nicolasi (2006), Sellier et al. (2011), and Hu et al. (2014).

As outlined above, mechanical models that account for the impact of mechanical loads differ substantially. The choice of the model depends on the specific features of the material behaviour that are important for a given application. Classical models make use of damage mechanics theory (Kachanov 1958), where a mechanical damage variable (d_m), also varying between 0 and 1, is defined (see Figure 3-3). In the simplest case, an isotropic scalar damage variable is considered. In these cases, the stiffness tensor reads:

$$\boldsymbol{E} = (1 - d_m) \cdot (1 - d_c) \cdot \boldsymbol{E_0} \tag{3-3}$$

where a multiplicative decomposition approach of chemical and mechanical damage is used. Several mechanical damage models are proposed in the literature, differing in the way to calculate the damage variable. One of the most widespread damage models, perhaps due to its simplicity, is the one proposed by Mazars (1986). This model defines an isotropic scalar damage variable with contributions from tensile and compressive damage, depending on the stress state. More details about Mazars' damage model can be found in Jirásek (2011) and in Section 5.1.1.

One important feature of mechanical damage models is that the results are typically mesh-dependent, i.e. they do not converge to a single solution upon refinement. To overcome this, several regularization methods have been proposed in the literature (integral-type nonlocal models, gradient-enhanced models, etc.). One common feature of these methods is that they typically rely upon the definition of a characteristic length of the concrete member. The local strain tensor at a given point depends in this framework on the strain in neighbouring points. These methods are thus usually referred to as nonlocal damage models. Table 3-1 indicates that five out of nine damage models do not make use of regularization methods. More details about gradient-enhanced damage models are presented in Section 5.1.2.

Gawin et al. (2008) proposed a model where the only damage accounted for is chemically-induced by calcium dissolution, while the mechanical model only considers elastic and creep strains. On the other hand, several models propose to decompose the strain tensor into an elastic, a plastic (i.e. irreversible strain), and a creep contribution to the total deformation (Cuomo and Nicolasi 2006, Sellier et al. 2011, Hu et al. 2014). In this way, mechanical damage accumulates, thus reducing the stiffness of the material, while irreversible strains are accounted for by a plasticity model. A schematic representation of plasticity, damage, and coupled damage-plasticity models is depicted in Figure 3-3. Under monotonic increasing load (imposed displacement or deformation), all models may yield the same result. However, under cyclic loading/unloading, damage models show no residual strain. Plasticity models, on the other hand, have a residual strain that is too large for concrete, as the unloading path follows the slope defined by the initial stiffness. A more realistic result is obtained with coupled damage-plasticity models (Cuomo and Nicolasi 2006, Hu et al. 2014), where residual strain upon unloading is more accurately captured. Those authors adopt the Drucker Prager plasticity criterion in their models.

In turn, time-dependent deformations under constant stress, which is an important phenomenon in concrete, are considered through a creep model. Again, different creep models have been proposed in the literature, with different levels of sophistication. For example, Torrenti et al. (2008) used a description in the form of a Dirichlet series of basic creep (Bazant and Chern 1985), while Gawin et al. (2008) made use of the solidification theory to model creep strains (Bazant et al. 1997). Sellier et al. (2011) used a sophisticated creep model that considers the decomposition of creep strains into spherical and deviatoric components. A simpler model, which considers a linear relation between basic creep strains and stress, is proposed by Hu et al. (2014). It is noted that in the context of deep geological disposal, where concrete structures can be considered as fully water saturated in the long-term, basic creep models are sufficient. Basic creep can be defined as a time-dependent deformation under constant load occurring at constant humidity conditions (i.e. the material has a homogeneous distribution of moisture content). Under unsaturated conditions, drying creep, i.e. deformation in excess to basic creep observed when the same material is exposed to drying while under load, would also need to be considered.

Most of the models are formulated in terms of total stresses, in which the impact of water pressure gradients is not considered. Some models consider a decomposition of the stress tensor to account for effective stresses (Gawin et al. 2008, Cuomo and Nicolasi 2006):

$$\boldsymbol{\sigma}' = \boldsymbol{\sigma} + b \cdot p \cdot \boldsymbol{I} \tag{3-4}$$

where $\boldsymbol{\sigma}'$ (MPa) is the Biot's effective stress, p is the pore pressure (MPa), b (–) is the Biot's coefficient, and $\boldsymbol{I}$ is the second order identity tensor. The Biot's coefficient ($0 < b < 1$) is introduced to account for the different values of bulk modulus for solid phase (grain) and the skeleton, K_s and K_T:

$$b = 1 - \frac{K_T}{K_S} \tag{3-5}$$

A formulation in terms of effective stresses is more appropriate in the cases where pronounced water pressure gradients are active and where the Biot's coefficient is relatively large (as in soils). For the present study, focusing on long-term degradation processes, water pressure gradients are not expected to play a significant role. The reason is that the analysis starts after the process of resaturation of the BHK vault after closure is completed. Under these conditions, water pressure gradients will practically vanish. Moreover, the Biot's coefficient for concrete is known to be below ~0.5 (Bary et al. 2000, Gawin et al. 2006, Cuomo and Nicolasi 2006, Cefis and Comi 2017). Some of the reported values are as low as ~0.2 (e.g. Gawin et al. 2006 on the basis of drying shrinkage measurements and modelling). This means that the effect of the pore pressure on the mechanical analysis is reduced by between 2 and 5 times with respect to the case where the Biot's coefficient is 1, as in plastic clays. Therefore, the use of a simpler model in terms of total stresses, as in most of the proposed models for concrete, seems to be supported also in the present study.

Table 3-1. Summary of main features of chemo-mechanical models proposed in the literature for the simulation of calcium leaching in cementitious materials.

Reference	Software	Chemical damage model	Mechanical damage model	Regularization technique	Plasticity model	Creep model	Stresses	Chemistry
Hu et al. (2014)	Comsol	As a function of dissolved Ca (M)	Tensile-compressive damage	No	Yes ***	Yes	Total	Diffusion-reaction eq.
Sellier et al. (2011)**	Cast3m	Empirical law as a function of Ca (M) and portlandite	Tensile-compressive damage	Yes	No	Yes	Effective	Diffusion-reaction eq.
Stora et al. (2010)	Alliances	Homogenization model	IDD damage model	No	No	No	Total	Reactive transport model
Torrenti et al. (2008)	Not specified	As a function of dissolved Ca (M)	Mazars' damage model	No	No	Yes	Total	Not modelled (empirical equation used)
Gawin et al. (2008)	COMES-LEACH	As a function of Ca (M) in solid	Not considered	-	No	Yes	Effective	Diffusion-advection-reaction eq.
Nguyen et al. (2007b)	CESAR-LCPC	E(Ca), W(Ca) *	Gradient damage model	Yes	Yes ***	No	Total	Diffusion-reaction eq.
Cuomo and Nicolasi (2006)	Not specified	As a function of dissolved Ca (M)	Isotropic damage	No	Yes	No	Effective	Diffusion-advection-reaction eq.
Kuhl et al. (2004)	Not specified	As a function of dissolved Ca (M)	Equivalent strain based	No	No	No	Total	Diffusion-reaction eq.
Le Bellégo et al. (2003)	Not specified	As a function of dissolved Ca (M)	Mazars' damage model	Yes	No	No	Total	Diffusion-reaction eq.
Gérard et al. (1998)	Cast3m	As a function of dissolved Ca (M)	Mazars' damage model	Yes	No	No	Total	Diffusion-reaction eq.

* E(Ca), W(Ca) stand for the elastic modulus and the initial damage threshold, both depending on the concentration of Ca (M).

** See also Lacarriere et al. (2006).

*** The Drucker Prager plasticity model is adopted in these models.

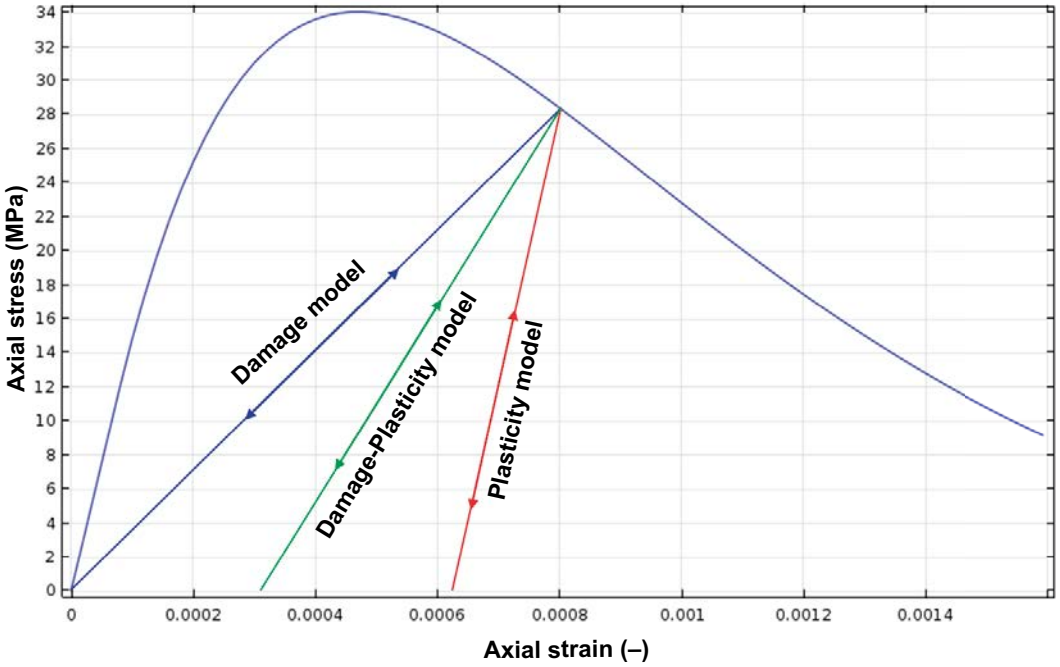

Figure 3-3. *Stress-stress diagram for a uniaxial compression test: schematic loading/unloading paths for a damage model, a plasticity model, and a damage-plasticity model.*

3.2 Degradation by external sulphate attack

3.2.1 Physical and chemical processes

The process of calcium leaching was presented in the previous section. The presence of other species in groundwater may trigger additional coupled chemo-mechanical degradation processes. In sulphate attack sulphate ions react with calcium aluminates in the cement paste leading to the formation of expansive ettringite and gypsum in the bulk material (Santhanam et al. 2002, Lothenbach et al. 2012). Ettringite and gypsum precipitation is accompanied by a reduction in the total porosity. However, in the event of substantial expansion, the concrete structure could be severely cracked and spalled, with negative impact on the transport properties and degradation rate (Brown and Taylor 1998, Idiart et al. 2011). It is noted that even for sulphate resistant cement there is evidence that delayed expansion due to external sulphate attack may still occur. Gypsum formation requires sulphate concentrations much higher than encountered under field conditions, making this process less relevant.

The presence of carbonates in groundwater can lead to the precipitation of calcite (Lagerblad and Trägårdh 1994, Idiart and Shafei 2019). This can lead to a reduction of porosity due to the higher molar volume of calcite compared to the reactants (Galíndez and Molinero 2010, Grandia et al. 2010a). Severe damage in concrete can originate from a combined attack by sulphate and carbonate at low temperatures (4–15°C). The process can lead to thaumasite ($Ca_3Si(OH)_6(SO_4)(CO_3)\cdot 12H_2O$) formation by reaction with AFm/AFt phases where silica from C-S-H-gel has replaced aluminate. Thaumasite has a very similar structure and morphology to ettringite, where alumina is replaced by silicon and carbonate partly substitutes sulphate. Since thaumasite formation does not involve aluminium, the use of sulphate-resisting Portland cement (with low alumina content) is not an effective measure against thaumasite formation. Furthermore, low temperatures would favour the stability of thaumasite. The formation of thaumasite requires a source of calcium silicate (mainly C-S-H phases), sulphate, carbonate and humidity (Schmidt 2010, and references therein). As it forms, concrete turns into a friable material which comes apart rather easily.

The presence of chlorides in groundwater in addition to sulphates may be beneficial for the durability of concrete, as expansive ettringite formation is mitigated to some extent (Zuquan et al. 2007, Santhanam 2011, Zhang et al. 2013). This positive effect, especially for high w/c ratios is thought to be due to the preferential precipitation of chloroaluminate compounds such as Friedel's salt, a reduced amount of sulphate products (due to the increased solubility of ettringite and gypsum in chloride-bearing solutions), and a reduced expansivity of the secondary ettringite. However, it has been suggested that thaumasite formation is amplified by the presence of chlorides (Torres et al. 2003).

Although sulphate attack is a classical type of deterioration that has been widely described in the literature (Neville 2004, Skalny et al. 2002), important issues aspects of the degradation mechanisms remain unclear. One fundamental aspect is the expansion mechanism itself and how to relate the abundance of mineral phases formed and expansion. Ettringite, gypsum, and thaumasite precipitation tends to increase the mineral volume and reduce porosity, but the relation with expansions is not straightforward (e.g. Odler and Colán-Subauste 1999). Moreover, porosity is not entirely filled with sulphate-bearing minerals when expansions are measured. Several interpretations of these observations can be found in the literature, as described in the next section.

Another important issue is the effect of mechanical stresses on the expansion mechanism. In standard laboratory experiments sample specimens are simply submerged in sulphate solutions, with no load applied. Expansions measured in such tests may therefore not be representative of field conditions, since concrete in underground structures is subject to different types of loads (see Section 6). Not much attention has been given to the effect of mechanical loads on expansions due to sulphate attack. Existing experiments of the simultaneous action of a sulphate solution and compressive stresses on concrete samples indicate that the expansions can be significantly reduced (Piasta and Schneider 1992, Živica and Szabo 1994).

3.2.2 Modelling expansions due to sulphate attack

Several models of mechanical behaviour of concrete under sulphate attack can be found in the literature. As for calcium leaching, an exhaustive analysis of each of these models is out of the scope of this work. The modelling of sulphate attack requires that the following processes are considered:

1. Dissolution of cement hydrates and precipitation of secondary minerals.
2. Transport of sulphates into and of dissolved species out from the system.
3. A chemical damage model to account for the impact of chemical reactions on the mechanical properties.
4. A mechanical model of concrete to account for the impact of mechanical loads.
5. A model to calculate expansions as a function of ettringite volume fraction or oversaturation.

The first two processes, i.e. chemical reactions and transport of sulphates, have been considered in most existing models as a non-linear diffusion-reaction equation for sulphate (Tixier and Mobasher 2003, Basista and Weglewski 2009, Idiart et al. 2011) or sulphate and calcium (Bary 2008). Similar to Bary et al. (2014), a reactive transport framework is used here (Idiart and Shafei 2019). Therefore, the coupling between sulphate attack and calcium leaching, at least from a chemical point of view, is naturally included in the model.

The chemical damage model is an important feature in calcium leaching models. However, most of the existing sulphate attack models do not include a chemical damage model. This is due to the fact that for the modelling of sulphate attack (short-term) experiments, the key feature is the calculation of expansions. However, in the long-term chemical damage is expected to play a significant role as a result of calcium leaching. The exceptions are the models where homogenization theory has been used to calculate the effective elastic properties (Bary 2008, Bary et al. 2014). Homogenization theory is also used herein to derive a chemical damage scalar variable (Section 5.2).

With respect to the mechanical models, different damage models have been used in most cases (Tixier and Mobasher 2003, Bary 2008, Bary et al. 2014, Cefis and Comi 2014), while a discrete fracture mechanics model has been used by Idiart et al. (2011) to model external sulphate attack at a mesoscopic level.

In classical models, expansions are considered proportional to the increase in volume as a result of ettringite formation (Clifton and Pommersheim 1994, Tixier and Mobasher 2003, Basista and Weglewski 2009, Idiart et al. 2011):

$$\boldsymbol{\varepsilon_v} = \frac{1}{3} \cdot \langle \alpha_s C_{reacted} - \beta\phi \rangle_+ \boldsymbol{I} \tag{3-6}$$

where $\boldsymbol{\varepsilon_v}$ (–) is the volumetric expansion tensor, $\boldsymbol{I}$ is the identity matrix, α_s is a scalar coefficient that takes into account the difference in volume between reactants and products, $C_{reacted}$ is the amount of cement minerals (hydrates, clinker) that have reacted to form ettringite, ϕ is the porosity, β is a factor (between 0 and 1) representing the fraction of porosity that needs to be filled before any expansion is

predicted, and $\langle\rangle_+$ are the Macaulay brackets to avoid the occurrence of shrinkage. One of the main concerns with this type of model is the sensitivity of the results on the β factor and the relatively large variation in the values for fitting different experimental observations. Indeed, values used in the literature to fit numerical models of sulphate attack to experimentally measured expansions range between 0.05 and 0.5, i.e. an order of magnitude difference (Tixier and Mobasher 2003, Basista and Weglewski 2009, Idiart et al. 2011).

More recent views consider that expansion is due to pressure exerted by ettringite crystal growth in small pores within the C-S-H matrix (Bary 2008, Flatt and Scherer 2008). The crystal growth in an oversaturated solution can be related to the pressure needed to suppress such growth according to Correns' equation:

$$p_c = \frac{RT}{V_m} ln(IAP/K_{s0}) \quad (3\text{-}7)$$

where p_c (Pa) is the crystallization pressure, R is the gas constant (8.31 J/K/mol), T (K) is the temperature, V_m (cm^3/mol) is the molar volume of the forming crystal, IAP is the ion activity product, and K_{s0} is the equilibrium solubility product of the chemical reaction of ettringite formation. The ratio IAP/K_{s0} is usually referred to as the saturation index. Thus, for p_c to be larger than zero, the saturation index needs to be also larger than zero. This oversaturation can only be achieved if a kinetic constraint is introduced for ettringite precipitation. So far, predicted expansions using this theory are very far from experimentally observed values (e.g. Bary et al. 2014). One of the main concerns is how to realistically upscale the crystallization pressure calculated at the micro- or nano-scale to the macroscopic level. This point is also related to the issue of how to deal with downscaling of solution concentrations from the continuum scale (i.e. the scale of thermodynamic modelling and reactive transport) to the micro- or nano-scale (or vice versa).

It is noted that none of the existing models deal with the effect of external mechanical loads on the expansions due to sulphate attack. In all cases, expansions under laboratory conditions (i.e. free of mechanical load) are modelled as an imposed volumetric strain, independently of the stress level. Application of existing models to concrete structures has so far not been attempted, except for the recent work by Cefis and Comi (2017). These authors modelled an experimental test of a reduced scaled tunnel in a sulphate rich soil and found a relatively good agreement between modelled and experimental measurements of settlements and tunnel convergence. The effect of compressive loads on reducing expansions by sulphate attack could be one of the reasons why this degradation process is seldom observed in the field.

3.3 Coupling between damage and transport properties

The effect of chemical damage resulting from dissolution/precipitation of minerals on the transport properties of the concrete material is traditionally treated using empirical relations between diffusivity and/or permeability and porosity (e.g. Sellier et al. 2011, Idiart and Shafei 2019). A different approach is to use homogenization schemes similar to those used for calculating the effective elastic properties to derive effective transport properties. This has already been proposed for calculating the effective diffusion coefficient in cementitious materials (Bary 2008, Stora et al. 2010). In this work, following the previous reactive transport study by Idiart and Shafei (2019), the following empirical functions are used:

- Archie's law for the diffusion coefficient, with an exponent of 3.5.
- Kozeny-Carman equation (Carman 1937) for hydraulic conductivity.

To determine the impact of mechanical damage on transport properties is not straight-forward, however. Permeability and diffusivity are functions of the level of micro- and macro-cracking of concrete, although the former is much more sensitive to the presence of cracks. Therefore, transport properties depend on the crack patterns, which are related to the type of loading that provoked these cracks (compressive or tensile loads, thermal loads, drying shrinkage, etc.).

The impact of mechanical damage on water and especially gas permeability has been characterised by many authors in several ways. Some authors studied the effect on permeability induced by mechanical damage under compressive loads (e.g. Picandet 2001, Bourdarot 1991, Djerbi et al. 2013). The impact

of damage caused by thermal loads has been studied by (Dal Pont 2004, Gawin et al. 2005, Travis and Mobasher 2010), while Wardeh et al. (2011) used frost cycles to generate mechanical damage. A summary of these studies is given in Table 3-2. Even though experiments are mostly gas permeability tests, they are used to derive the intrinsic permeability, which can then be used to model water permeability. The different relations proposed are plotted in Figure 3-4 assuming in all cases that the undamaged water permeability is 8.3×10^{-17} m^2, which corresponds to the initial value used in previous SKB studies (e.g. Höglund 2014, Idiart and Shafei 2019). For the present study, damage from mechanical compression tests seems to be more appropriate. However, even for a similar damage mode with similar crack patterns the scatter between different relations is significant. Therefore, the determination of a general relation between mechanical damage and permeability is subject to a high level of uncertainty. In all cases, a significant increase in permeability is observed even for moderate values of mechanical damage.

Table 3-2. Summary of available relations between mechanical damage of different sources and permeability.

Reference	Measured permeability	Type of damage
Bourdarot (2001)	-	Mechanical compression tests
Picandet (2001)	Gas permeability	Mechanical compression tests
Djerbi et al. (2013)	Gas permeability	Mechanical compression tests
Wardeh et al. (2011)	Gas permeability	Frost cycles damage
Dal Pont (2004)	Gas permeability	Thermo-mechanical damage
Gawin et al. (2005)	-	Thermo-mechanical damage
Travis and Mobasher (2010)	Gas permeability	Thermo-mechanical damage

In the case of the effective diffusion coefficient, the effect of single cracks has been studied experimentally by many authors (e.g. Wang et al. 1997, Djerbi et al. 2008, Ismail et al. 2008). However, relations between the effective diffusion coefficient and mechanical damage based on experimental results are largely missing. Two different relations have been used in existing modelling studies (Gérard et al. 1998, Hu et al. 2014), as shown in Figure 3-5. These expressions, however, have not been derived from experimental data.

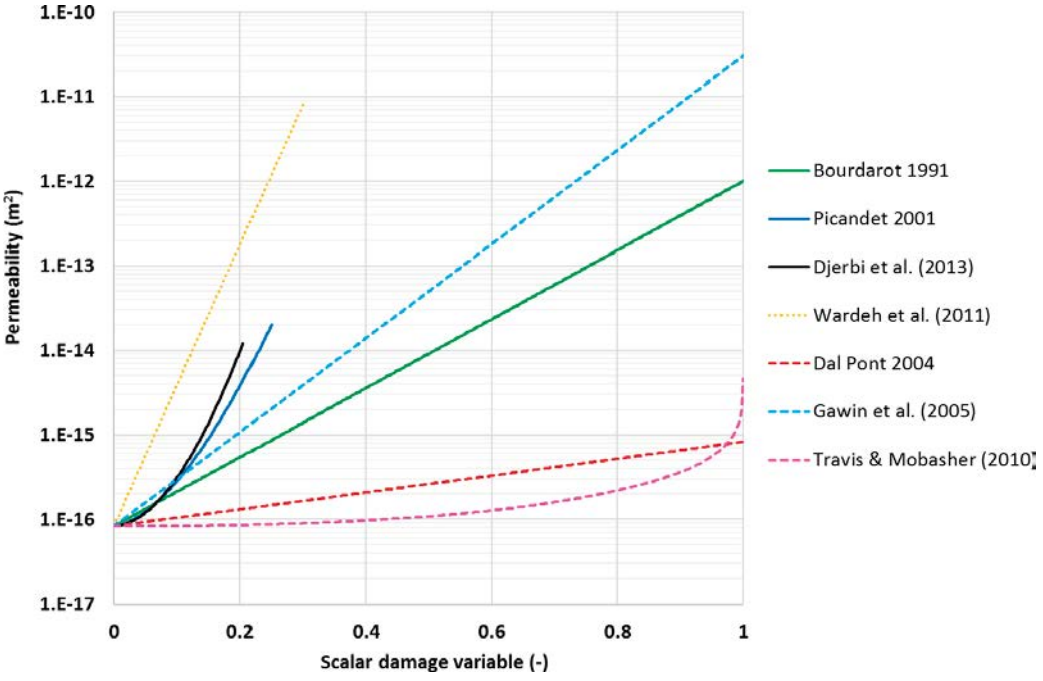

Figure 3-4. *Relations between mechanical damage (–) and permeability (m^2) proposed by different authors based on experimental results. Solid lines correspond to experiments where damage is caused by compressive stress tests, dashed lines correspond to thermo-mechanical experiments, while the dotted line corresponds to damage caused by frost cycles.*

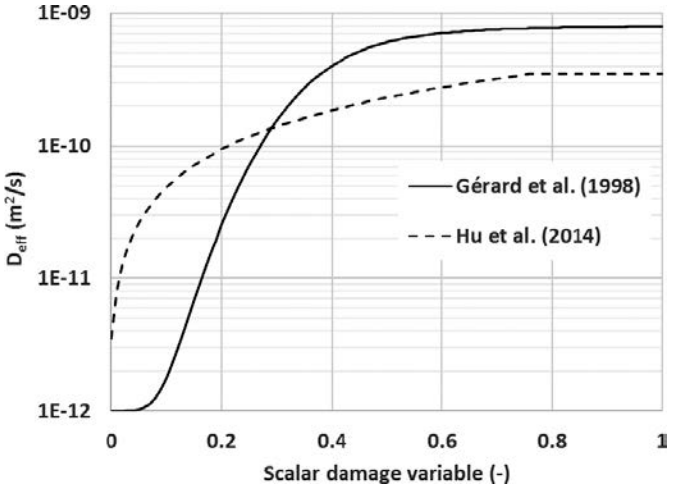

Figure 3-5. *Relations between mechanical damage (–) and effective diffusion coefficient (m^2/s) proposed by different authors for modelling studies.*

As shown above, for the cases where mechanical damage is significant, coupling with the transport properties can accelerate the chemical degradation process substantially. Where mechanical damage is substantial, the approach adopted in this study for water permeability follows from the relations of Picandet (2001) and Djerbi et al. (2013) for low levels of damage and that of Bourdarot (2001) for higher levels. These expressions were derived based on results of damage caused by cracking due to compressive stresses. When concrete is completely damaged, the value of permeability resembles that of pure ballast (~10^{-12} m^2). The proposed relation is therefore:

$$K_h = K_{h0} \cdot 10^{a \cdot \left(1 - \frac{1}{1 + \left(\frac{d}{d_{cr}}\right)^n}\right)} \tag{3-8}$$

where K_h (m^2) is the permeability of damaged concrete and K_{h0} (m^2) is the permeability of intact concrete. In this work, a value of 8.3×10^{-17} m^2 is used as the initial permeability even though this value considers the effect of traversing fractures (see Höglund 2014). Furthermore, a, n, and d_{cr} (–) are model parameters, and d (–) is the mechanical damage variable. This function is fitted to the expressions proposed by different authors based on experimental results in Figure 3-6. The model parameters are: a = 4.16, n = 2.6, and d_{cr} = 0.22.

In turn, for relating the effective diffusion coefficient and mechanical damage, the S-function proposed by Gérard et al. (1998) is used:

$$D_e = D_0 + D_{max} \cdot \left(1 - \frac{1}{1 + \left(\frac{d}{d_{cr}}\right)^n}\right) \tag{3-9}$$

where D_0 and D_{max} are the diffusion coefficients of intact concrete and for a completely damaged concrete, respectively, and n and d_{cr} are model parameters (n = 5, d_{cr} = 0.4). The value of D_{max} is 0.8×10^{-9} m^2/s (Gérard et al. 1998).

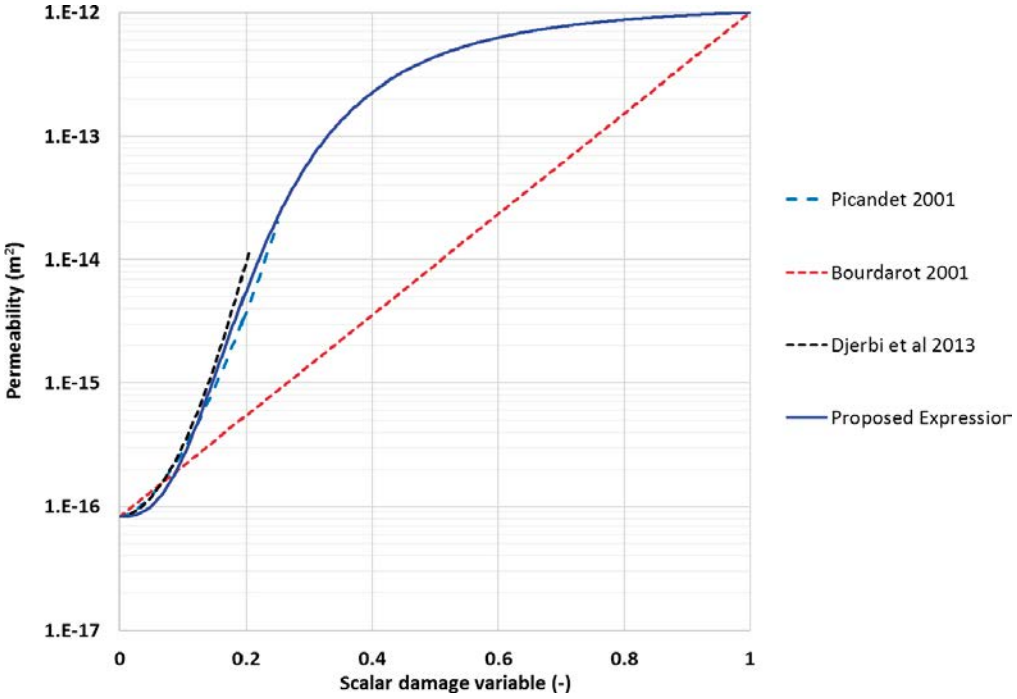

Figure 3-6. *Relations between mechanical damage (–) and water permeability (m^2): comparison between the proposed expression (solid line) and the relations proposed by different authors based on experiments where damage is caused by compressive stress tests (dashed lines).*

3.4 Conclusions

Several chemo-mechanical models have been proposed in the literature to study calcium leaching and sulphate attack. Similar processes, as listed in Sections 3.1.2 and 3.2.2, need to be taken into account to model each process. The main difference is that for sulphate attack expansions due to ettringite formation need to be added to the model. Reactive transport models, as used in the present study, are suitable to study both degradation processes in a coupled way. Moreover, homogenization models appear as flexible mechanistic tools to calculate chemical damage instead of the more problem-specific empirical relations between chemical damage and calcium concentration in the pore solution. Therefore, an existing homogenization model is implemented (Stora et al. 2010, Bary et al. 2014) and used to model calcium leaching and sulphate attack.

The mechanical models proposed to study calcium leaching and sulphate attack are diverse, although models based on damage mechanics are preferred. Among these models, Mazars' damage model has been selected in this study. The reasons are that it is conceptually simple, relatively easy to implement in Comsol, it is robust, and finally that it consists of one of the most popular damage models for concrete. However, as any other damage model, the results obtained with this model are mesh dependent. Therefore, a regularization technique is important to eliminate the mesh dependence. The details of the regularization method are presented in Section 5.1.2.

The review of the physico-chemical processes and existing models of expansions due to sulphate attack shows that there is a relatively high degree of uncertainty. Existing models able to simulate similar expansions as observed experimentally are based on imposing a volumetric strain that results from the difference in volume between reactants and reaction products. The parameterization of these models is not easy, because the magnitude of the expansion and deformation patterns depend on the β factor. The way to cope with this problem is to fit the value of β with measured expansions in a laboratory test using a similar concrete. However, these tests are typically performed without any mechanical load. Thus, the validity of expansion models for field conditions is not straightforward. A few sulphate attack experiments performed under compressive load indicate that expansions would be substantially reduced. In this work, expansions are modelled under field conditions using a volumetric strain approach. The value of the β factor is first derived from experimental tests on a similar concrete (Section 5.3.3).

Finally, a review of how to consider the effect of mechanical damage on the transport properties (effective diffusion coefficient and permeability) shows a noteworthy degree of uncertainty. For intrinsic permeability, several experimental studies have been published that propose different relations with mechanical damage. Herein, it is reasonably assumed that the experiments based on compression can be used to derive a new relation (Equation 3-8). The impact of mechanical damage on diffusion has received less attention, and only a few empirical relations are available in the literature. The expression proposed by Gérard et al. (1998) is used in our model.

4 Methodology

The goal of the present work is to perform a preliminary assessment of the coupling between potential degradation processes of the concrete barriers in the BHK vault and the mechanical behaviour of the concrete structure. As described in Idiart and Shafei (2019), degradation is driven by the interaction of the barriers with groundwater. The impact of mechanical stresses due to active loads at repository depth and the chemo-mechanical couplings due to interaction with groundwater are explicitly considered and quantified.

The methodology followed to study the influence of chemical degradation of the concrete barriers on their mechanical stability is based on two-dimensional (2D) simulations of a cross-section of the BHK vault. To this end, 2D hydro-chemo-mechanical (HCM) models of a cross-section are developed. The models consider coupled hydro-chemo-mechanical (HCM) processes, as discussed in Section 3. These HCM models, implemented using iCP (Nardi et al. 2014), consider the following coupled processes: fluid flow, solute transport, chemical reactions, and mechanical deformations. A more detailed description of the models is presented in Section 5. A summary of the simulations cases presented in this report is given in Table 4-1.

Table 4-1. Summary of simulation cases of calcium leaching and external sulphate attack (ESA), including a Base Case and a set of sensitivity cases. EW (GPa) and ER (GPa) stand for waste and rock stiffness (Young's modulus).

Study number	Description	Depth (m)	Rotation (°)	Glaciation stresses	E_W (GPa)	E_R (GPa)	Number of simulations	Coupling
1	Base Case	500	0	No	1	70	1	$\varphi \longrightarrow (D_{eff},K)$
2	Effect of depth	700	0	No	1	70	1	$\varphi \longrightarrow (D_{eff},K)$
3	Effect of orientation	700	15	No	1	70	1	$\varphi \longrightarrow (D_{eff},K)$
4	Effect of glaciation	700	0	Yes	1	70	1	$\varphi \longrightarrow (D_{eff},K)$
5	Effect of E_w	500	0	No	0.04–213	70	9	$\varphi \longrightarrow (D_{eff},K)$
6	Effect of E_R	700	0	No	1	25–70	4	$\varphi \longrightarrow (D_{eff},K)$
7	ESA-one-way-coupled	700	0	No	1	70	1	$\varphi \longrightarrow (D_{eff},K)$
8	ESA-fully-coupled	700	0	No	1	70	1	$d_m \longrightarrow (D_{eff},K)$
						Total	19	

4.1 2D HCM model of calcium leaching

The simulations presented here are based on a previous reactive transport modelling study of the BHK vault (Idiart and Shafei 2019). The Base Case (Case I), as defined in Idiart and Shafei (2019), is used in this study. As described in Section 1.2, one of the main outcomes of the reactive transport models in Idiart and Shafei (2019) was that the degradation processes are mainly driven by calcium leaching out of the concrete backfill. Therefore, the HCM model considers specific features of the coupling between mechanically-driven and chemically-driven damage when concrete is subject to calcium leaching. A schematic representation of the coupling between different processes considered in the HCM model is shown in Figure 4-1.

An analysis of the uncertainty linked to reactive transport processes is presented in Idiart and Shafei (2019) and is therefore not considered further in this study. Instead, the model is used to test the sensitivity of the results to certain key rock mechanics parameters.

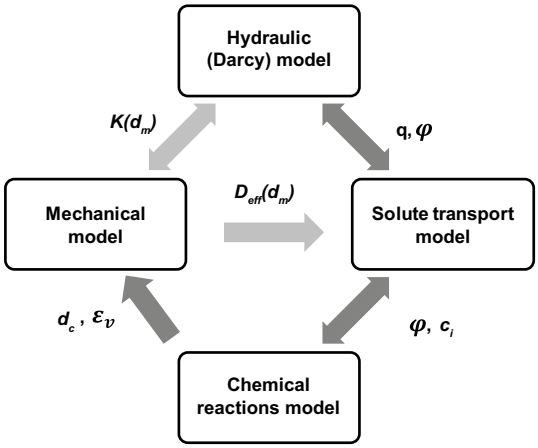

Figure 4-1. *Schematic representation of coupling between the different physical and chemical processes in the model. d_c = chemical damage; d_m = mechanical damage; ε_v is the volumetric expansion resulting from ettringite/thaumasite formation; $K(d_m)$ and $D_{eff}(d_m)$ are empirical relations of hydraulic conductivity and effective diffusivity as a function of mechanical damage; q is the Darcy velocity; c_i is the concentration of species; φ is the porosity.*

4.1.1 Repository depth

In the proposed concept for SFL, the repository is situated in granitic rock. The depth of the repository is still not precisely defined and could range between approximately 300 to 700 m. The Base Case (Case I), as defined in Idiart and Shafei (2019), assumes a repository depth of 500 m. Thus, the sensitivity of the results of the HCM model to a change in depth from 500 to 700 m is studied.

The effect of repository depth on groundwater flow through the barriers and waste was quantified in the work by Abarca et al. (2016). With an increase in depth, groundwater flow was systematically reduced in all simulated cases, due to reduction of the hydraulic conductivity of the host rock. The groundwater flow through BHK was reduced by a factor of 3 to 6 when going from 500 to 700 m depth (see Figure 4-2). This is not considered significant and for the present work it is assumed that the groundwater flow in BHK is constant with depth.

In-situ stresses in the host rock are a function of depth and act as loads on the repository structures. In the Laxemar area, this dependency has been determined to be (Hakami et al. 2008):

$$\sigma_H = 0.039(MPa/m) \cdot z(m) + 3\ (MPa) \quad (4\text{-}1)$$

$$\sigma_h = 0.022(MPa/m) \cdot z(m) + 1\ (MPa) \quad (4\text{-}2)$$

$$\sigma_v = 0.027(MPa/m) \cdot z(m) \quad (4\text{-}3)$$

where σ_H and σ_h (MPa) are the maximum and minimum horizontal in-situ stresses, respectively, and σ_v (MPa) is the vertical in-situ stress. The depth z (m) is given by positive values. The estimated uncertainty in the mean values is ±20 % for horizontal stresses and ±3 % for vertical stresses. The orientation of the maximum principal stress is 135° from the North (and the minimum horizontal stress at 45°), with an uncertainty of ±15°.

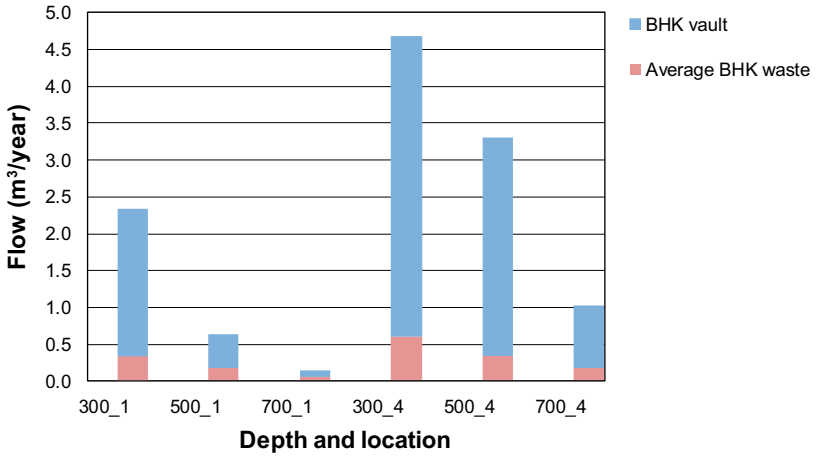

Figure 4-2. *Groundwater flow in (m^3/year) reaching the BHK vault and the waste domains at different depths and at two different locations, 1 and 4 (adapted from Abarca et al. 2016).*

4.1.2 Repository orientation

In Abarca et al. (2016), the effect of changing the repository orientation on groundwater flow through the barriers and waste was quantified. A modest correlation of orientation to vault flow was shown (Figure 4-3). Therefore, a reasonable assumption is that groundwater flow through BHK is independent with orientation in a horizontal plane. The results of the reference orientation (0°) have been used to calculate the groundwater flow.

On the other hand, the orientation of the vault axis is very important in terms of rock mechanics stability criteria. Active loads from the rock on the underground structures depend on the orientation of the repository. In the Laxemar area, the maximum horizontal stress is oriented at 135° from the North and the minimum horizontal stress at 45°. To minimise the risk of mechanical instabilities, the axis of the vault should be parallel to the direction of the highest horizontal in-situ stress. The HCM model has been used for a preliminary quantification of the mechanical stability due to loads at different repository orientations (Section 6.3.2.2).

Given the estimated uncertainty of ±15° in the orientation of σ_H, two scenarios are simulated: a Base Case considering the axis of the vault parallel to the σ_H orientation and another case with a 15° deviation of the axis. This is schematically showed in Figure 4-4 and quantitatively in Figure 4-5. It can be observed that a 15° rotation leads to higher horizontal stresses perpendicular to the vault axis. It is noted that the vertical stress remains constant and independent of the rotation of the vault in the horizontal plane. Therefore, the rotated case can be regarded as one scenario with vertical load under higher horizontal confinement, compared to the Base Case. Horizontal shear stresses at the concrete-rock interface arising from the rotation of the vault are not considered in the model (estimated at ~2.6 MPa for a 15° rotation).

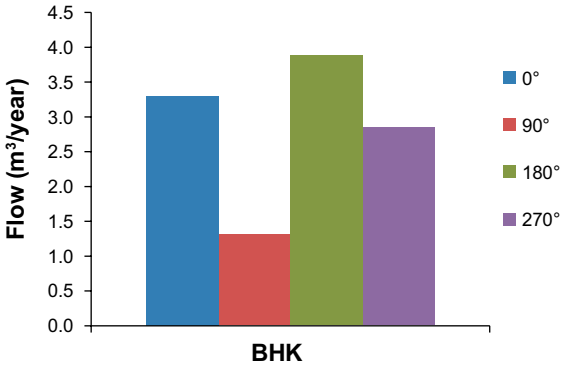

Figure 4-3. *Groundwater flow (mainly horizontal) reaching the repository at location 500_4: results in (m^3/year) through the BHK vault for the different rotation cases (adapted from Abarca et al. 2016). Variations in flow are 4 times at the most.*

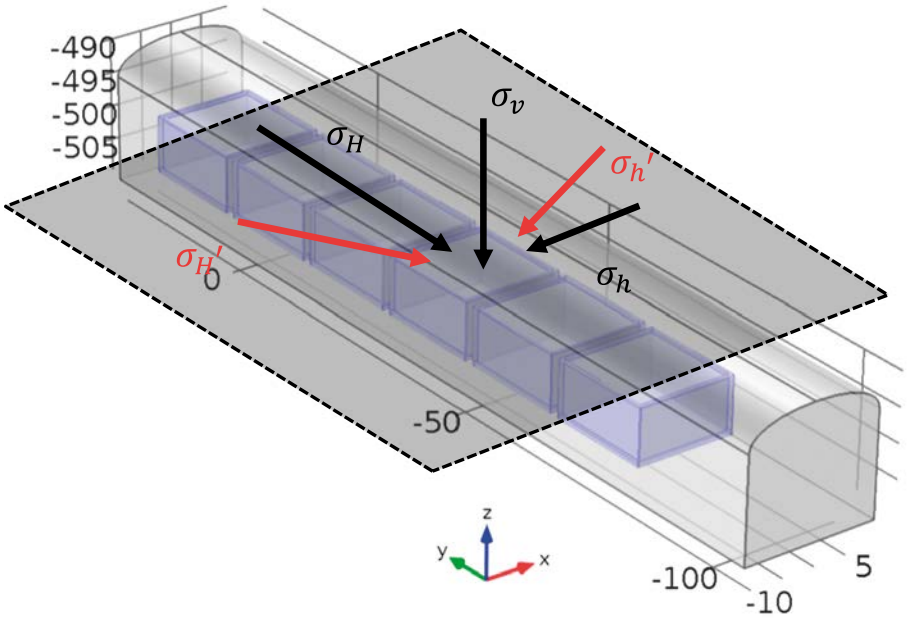

Figure 4-4. *Schematic representation of a rotation of 15° in the horizontal plane of the BHK vault axis with respect to the maximum and minimum in-situ horizontal stresses.*

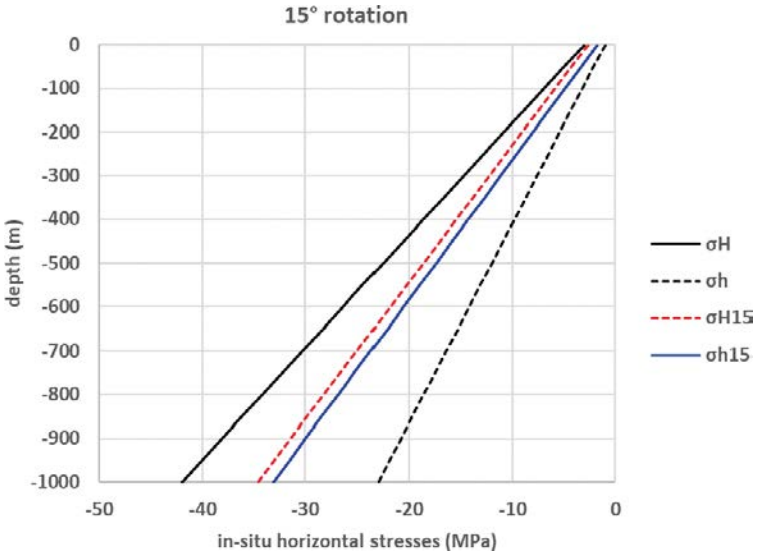

Figure 4-5. *Maximum (σ_H) and minimum (σ_h) in-situ horizontal stresses (MPa) in the Laxemar area as a function of depth (m) (black lines), and stresses parallel (sub index "H") and perpendicular (sub index "h") to the BHK vault axis when considering a 15° rotation (sub index "15").*

4.1.3 Glaciation and permafrost

The SFL repository will eventually be subject to a glaciation (e.g. SKB 2006). The ice sheet that is formed will significantly increase the mechanical load on the repository vaults. This increase is due to (1) the additional weight of the ice itself and (2) to the flexural response of the Earth's lithosphere. The latter induces horizontal stresses that can be of the same magnitude as the vertical stress due to the weight of the ice (Lund et al. 2009). Stresses in the Laxemar area induced by the Weichselian glaciation have been modelled in three dimensions using ice and earth models (Lund et al. 2009). Several scenarios were considered with different model assumptions. The results of the model T9 are used in the present work to assess the effect of an increase in the in-situ stresses on the mechanical stability of the BHK vault. That model fits rather well the GPS and sea-level data, while the lithospheric elastic structure is in general agreement with the Fennoscandian seismic investigations. The induced stresses are presented in Figure 4-6.

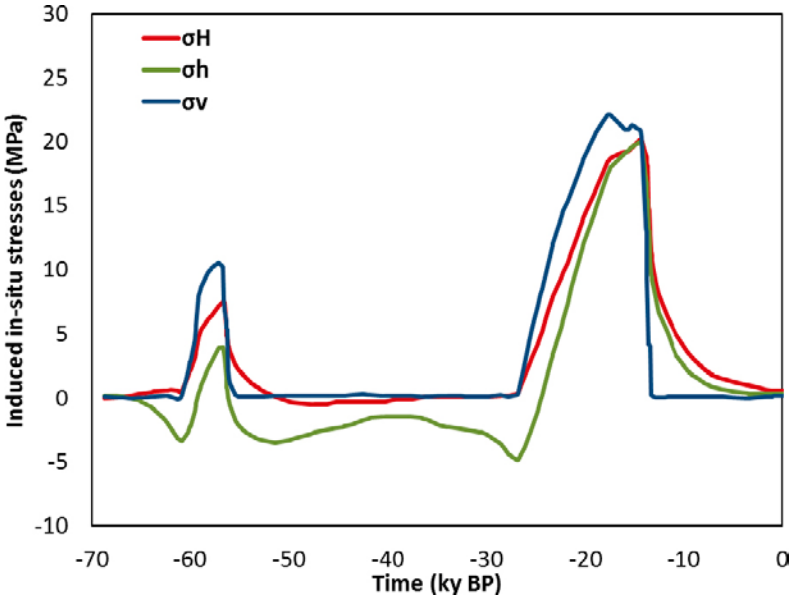

Figure 4-6. *Temporal evolution of the induced maximum horizontal (σ_H), minimum horizontal (σ_h) and vertical (σ_v) in-situ stresses at 500 m depth in Oskarshamn during glaciation. Results corresponding to the horizontally stratified model T9 (digitized from Lund et al. 2009). X-axis represents time before present (BP), expressed in thousands of years (kyr).*

4.1.4 Stiffness of the waste and rock domains

The mechanical behaviour of the waste constitutes a source of uncertainty when calculating the mechanical stresses in BHK. In the model, this domain is treated as a homogeneous continuous medium. Its effective properties in terms of the composition and amount of cementitious materials have been assessed by Pękala et al. (2015) and used in Idiart and Shafei (2019). However, there is no information regarding the mechanical properties. The density of the waste domain, needed to calculate the self-weight load, can be approximated as 2 890 kg/m^3 from the weight and volume of individual waste packages.

The stress state of the concrete backfill will depend on the stiffness of the waste domain. If the stiffness of the waste domain is changed, a redistribution of stresses in the concrete backfill and the rock in the vicinity of the vault is expected. Therefore, the effect of the stiffness of the waste domain on the stresses in the concrete backfill is assessed with the HCM model.

The stiffness of the fractured rock mass is also subject to uncertainty given its heterogeneity. A decrease in the values of the rock stiffness will translate into an increase in the stresses concrete vault. The effect of changes in the rock stiffness is assessed through a sensitivity study to this value. With an average value of 70 GPa, load transfer to the concrete backfill (stiffness of 42 GPa) will be relatively low. The most extreme sensitivity case considered assumes a stiffness of the rock of 25 GPa, which leads to a much higher load transfer efficiency. This value has been previously used by Malm (2012) to indirectly account for rock settlements and creep deformations.

4.2 2D HCM model of sulphate attack

In the reactive transport models in (Idiart and Shafei 2019), a groundwater with a sulphate concentration of 5.25×10^{-4} M (0.05 g/l) was used. This groundwater corresponds to an old-meteoric water, see Pękala et al. (2015) and references therein. Under these low sulphate concentrations, degradation of concrete due to sulphate attack is not expected to play a role. Reactive transport simulations (Idiart and Shafei 2019) confirmed that no ettringite precipitates within the concrete barrier as a result of interaction with groundwater. This is in line with most building codes, where the allowed maximum sulphate concentration for using any type of cement and concrete ranges between 1.6 mM to 6 mM, as shown in Table 4-2.

Table 4-2. Sulphate concentration limits defined in different building codes. These limits correspond to thresholds below which any kind of cement or concrete composition can be used without compromising durability.

Limit according to	ppm	mol/kgw
ACI Committee 201	150	0.0016
European standard (EN206-1:2000)	200	0.0021
British code	400	0.0042
Spanish code	600	0.0062

However, the composition of groundwater in the Laxemar area may have substantially higher sulphate concentrations. Figure 4-7 shows measured sulphate concentrations from boreholes, taken from the Laxemar site descriptive model (Kalinowski 2009). Concentrations exceeding the thresholds defined in building codes can be found in samples obtained at repository depth or lower. With these concentrations (> 2 mM), ettringite may form in the presence of a source of alumina in the cement paste. Consequently, sulphate attack (see Section 3.2) cannot be ruled out *a priori*. The potential damage caused by sulphate attack in the BHK vault is assessed with the HCM model, as discussed in Section 3.2.2. The model is similar to the one used for calcium leaching, with the addition of an expansion term in the calculation of stresses, as described in Section 5.1.3. A sulphate concentration of 0.01 M is used as a reasonable value of Laxemar groundwater at large depth.

Even though the sulphate concentration in groundwater is important for ettringite formation, the source of aluminates in cement determines the maximum ettringite concentration that can form in the matrix. In the models presented in Section 7, the source of aluminates is the initial amount of hydrogarnetSi and hydrotalciteOH (Table 6-2). The maximum ettringite concentration that can form is therefore the sum of the initial concentration (0.012 mol/litre of medium) plus the ettringite formed from the dissolution of these two phases (0.1215 mol/litre of medium): 0.1335 mol/litre of medium (or 0.094 volume fraction, assuming a molar volume of 0.707 litre/mol, see Appendix A).

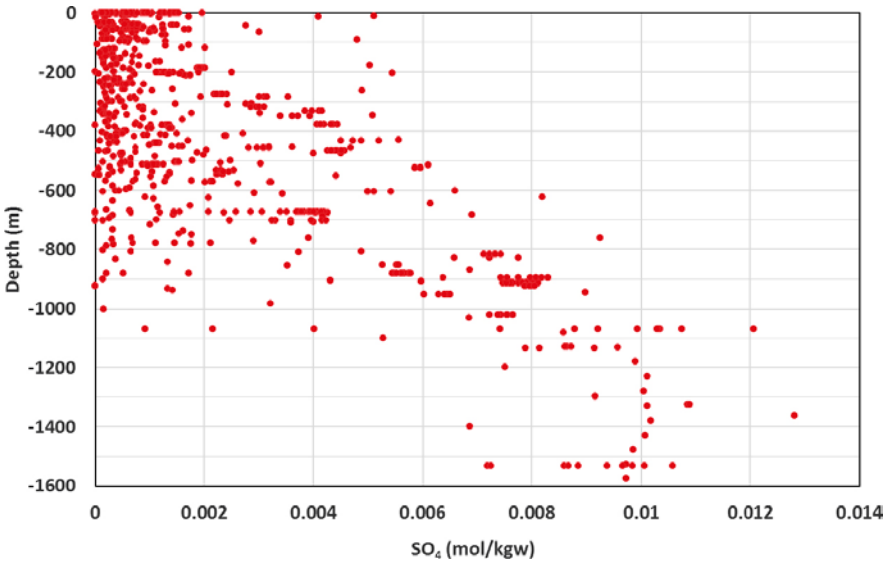

Figure 4-7. *Sulphate concentrations measured in groundwater samples from different boreholes of the Laxemar site as a function of depth (data from Kalinowski 2009).*

This ettringite concentration can be obtained with different groundwater compositions. Depending on the cement mineralogical composition and the groundwater composition, the stability of ettringite will evolve as a function of the solid/liquid ratio (e.g. Damidot and Glasser 1992). Different groundwater compositions are analysed, starting with a sulphate concentration of 0.01 M (Table 7-1) and then evaluating decreasing concentrations (0.0075, 0.0060, 0.0050, 0.0025, and 0.0010 M). Charge balance is obtained by adjusting Na and Mg concentrations. Increasing the amount of groundwater in contact with a given mineralogical composition of concrete is equivalent to study the effect of increasing pore volume replacements. The results for the different cases analysed in terms of ettringite volume fraction for different pore volume replacements are shown in Figure 4-8.

It may be observed that the maximum ettringite volume fraction of 0.094 is obtained not only for a sulphate concentration of 0.01 M, but also for 0.0075 M. However, more pore volume replacements are needed to reach this value in the latter case. Additional pore volume replacements gradually dissolve ettringite when its chemical stability conditions are no longer met. Reducing the sulphate concentration to between 0.0060 and 0.0025 M leads to a reduced amount of maximum ettringite, while a value of 0.001 M leads to gradual dissolution instead of precipitation. Therefore, the value of 0.01 M adopted in this study falls within the range of sulphate concentration that is sufficient to transform all the aluminates in cement into ettringite. This range is between ~0.0075 and 0.01 M.

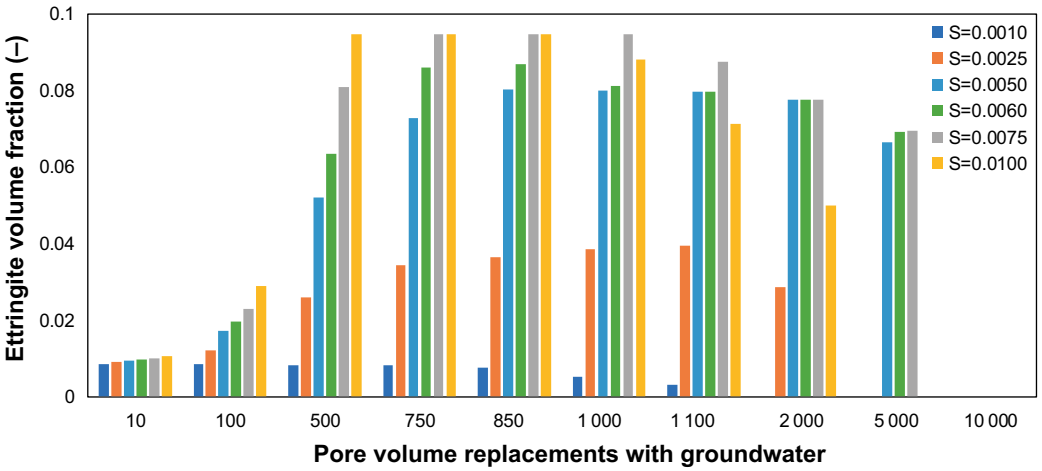

Figure 4-8. *Ettringite volume fraction (–) as a function of the number of pore volume replacements with groundwater of different compositions. S refers to sulphate concentration expressed in M.*

5 Model implementation

As a conclusion from the literature review in Section 3, the model implemented in this study accounts for the following processes and constitutive relations:

- A mechanical damage model, following the work by Mazars (1986).
- A regularization method to eliminate mesh dependence of the results of the damage model.
- Expansions due to sulphate attack, following the approach based on an increase in solid volume.
- A chemical damage model that is calculated using a multi-scale homogenization model developed by Stora et al. (2010).

In this section, the different components of the model are described in greater detail.

5.1 Constitutive laws for concrete mechanical behaviour

The constitutive laws for solid mechanics' models fully describe the stress-strain relationship. Non-linear constitutive models are used to capture the behaviour of concrete under tension and compression. Stresses increase under increasing deformation in non-linear models for concrete, reaching a peak stress and then gradually decreasing following a softening curve.

5.1.1 Mazars' damage model

In the damage model proposed by Mazars (1986), the damage variable defined in Equation 3.3 is described by the evolution laws for tension and compression. The total mechanical damage, d_m, is calculated as a linear combination of compressive and tensile damage contributions:

$$d_m = \alpha_c d_{m,c} + \alpha_t d_{m,t} \tag{5-1}$$

where $d_{m,c}$ and $d_{m,t}$ are the compressive and tensile damage variables (varying between zero and 1), respectively, and α_c and α_t are the compressive and tensile weights, respectively. The evolution laws for tensile and compressive damage are given by

$$d_{m,t}(\tilde{\varepsilon}) = 1 - \frac{\varepsilon_0}{\kappa} \cdot (1 - A_t) - A_t e^{-B_t(\tilde{\varepsilon} - \varepsilon_0)} \tag{5-2}$$

$$d_{m,c}(\tilde{\varepsilon}) = 1 - \frac{\varepsilon_0}{\kappa} \cdot (1 - A_c) - A_c e^{-B_c(\tilde{\varepsilon} - \varepsilon_0)} \tag{5-3}$$

where A_t, B_t and A_c, B_c are model material parameters that define the nonlinear stress-strain relation under tension and compression, respectively, ε_0 is a material parameter that defines the linear elastic limit or damage threshold (deformation at which damage starts to accumulate). The mechanical damage model parameters are subject to the following constraint to ensure a continuous variation of the slope of the stress-strain curve under compression (Jirásek 2011):

$$A_C B_C \varepsilon_0 = A_C - 1 \tag{5-4}$$

Variable κ is a history variable that stores the maximum value of the equivalent strain, $\tilde{\varepsilon}$, defined by the principal strains in tension, ε_1, ε_2, and ε_3:

$$\tilde{\varepsilon} = \sqrt{\langle \varepsilon_1 \rangle^2 + \langle \varepsilon_2 \rangle^2 + \langle \varepsilon_3 \rangle^2} \tag{5-5}$$

In Equation 5-5, $\langle \varepsilon \rangle$ refers to the positive part of ε. The compressive and tensile weights are calculated as a function of the tensile principal strains

$$\alpha_t = \sum_{i=1}^{3} \frac{\varepsilon_{ti} \langle \varepsilon_i \rangle}{\tilde{\varepsilon}^2} \tag{5-6}$$

$$\alpha_c = \sum_{i=1}^{3} \frac{\varepsilon_{ci} \langle \varepsilon_i \rangle}{\tilde{\varepsilon}^2} \tag{5-7}$$

where ε_{ti} are principal strains due to positive (tensile) stresses and ε_{ci} are compressive strains calculated as the difference between the principal strains and ε_{ti}.

As discussed by Jirásek (2011), this damage model leads to a good approximation of the experimentally-measured biaxial failure envelope of concrete under biaxial tension and tension-compression. However, under biaxial compression, the model underestimates the stresses at which failure occurs. As will be shown in Section 6.3, biaxial compression is the main stress-regime in the concrete backfill of BHK. The use of the Mazars' damage model in this case can be regarded as a conservative assumption. Jirásek (2011) describes how to partially remedy this deficiency, which will be attempted in future work.

The Mazars damage model is already included in Comsol Multiphysics as an External Material Functions in the Structural Mechanics Module, available in Comsol version 5.2. The External Material Function is implemented as a function programmed in C. The use of an External Material Function has the disadvantage that other constitutive models, built-in in Comsol, cannot be combined in a single model. Moreover, the monitoring of variables in the model is not as straightforward as with built-in functionalities.

In this work, the Mazars's damage model has been implemented in Comsol using a generic physics (Domain Ordinary Differential Equation) and a specific solver configuration to allow for storing the history variables. The main feature of the implementation is the definition of two history variables needed in the mechanical damage model. Two additional degrees of freedom (DOFs) are added through this new physics. Section 5.3.1 shows a comparison of the two implementation methods for a compression test with a loading/unloading function that confirms that both methods yield the same results. The main advantages of the new implementation are that: (1) it can be fully coupled with other physics and any other constitutive law, (2) all variables are available thus facilitating the post-process of results, and (3) the mechanical damage model is easier to adjust or reformulate in the physics tree, without the need of code compilation.

The Mazars' damage model has certain limitations that must be considered:

- Failure in the model only occurs when extension of the material in some direction exists. Therefore, no failure under triaxial compression is predicted by the model (e.g. Pijaudier-Cabot and Mazars 2001).
- Under biaxial loading (plane stress), the strength in the compression-compression regime is lower than observed in experiments (e.g. Jirásek 2011).
- As any other damage model, there is no residual or plastic strain upon unloading. Therefore, the model is not suitable for cases where loading/unloading cycles are applied.

5.1.2 Regularization method

The use of damage models for cementitious materials (quasi-brittle materials) has the disadvantage that the results are mesh dependent. To remedy this, several methods have been proposed in the literature to regularize the solution so that the results converge to a single solution upon mesh refinement. The regularization methods need to be solved simultaneously with the constitutive law and incorporate a characteristic length to prevent localization of strain into an arbitrarily small volume. The models are non-local, in the sense that the stress at a given point depends not only on the state variables at that point, but also account for a neighbouring region defined by the characteristic length.

A gradient-enhanced model has been implemented in Comsol following an implicit gradient formulation (Peerlings et al. 1996, Simone 2007). This model consists of a Helmholtz type differential equation in terms of the equivalent strain, $\tilde{\varepsilon}$ defined by Equation 5-5:

$$\bar{\varepsilon} - l^2 \nabla^2 \bar{\varepsilon} = \tilde{\varepsilon} \tag{5-8}$$

where l (m) is the characteristic length and $\tilde{\varepsilon}$ is the nonlocal variable that results from solving this equation together with the following boundary condition applied on the entire physical boundary:

$$n \cdot \nabla \bar{\varepsilon} = 0 \tag{5-9}$$

where n is the vector normal to the boundary surface. The history variable κ is calculated with this nonlocal variable instead of the equivalent strain.

The regularization of Mazars's damage model has been implemented in Comsol using the built-in Helmholtz equation physics. In Section 5.3.1 an application of the regularized model to a notched concrete beam is presented as a verification case.

5.1.3 Expansions due to sulphate attack

As discussed in Section 3.2, existing models of external sulphate attack are subject to a relatively high degree of uncertainty when used for predictive purposes. This is especially true under field conditions, where there may be a large effect of mechanical loads on overall expansions due to sulphate attack. Herein, expansions are considered proportional to the increase in volume due to ettringite formation. Furthermore, it is considered that compressive stresses do not impact these volumetric expansions.

Volumetric expansions are calculated using the following expression

$$\boldsymbol{\varepsilon_v} = \frac{1}{3} \cdot \left\langle \Delta\vartheta_{ettr} - \Delta\vartheta_{ht} - \Delta\vartheta_{hg} - \beta\varphi^* \right\rangle_+ \boldsymbol{I} \tag{5-10}$$

where ϑ (m^3/m^3) are volume fractions, β is a material parameter, φ^* (m^3/m^3) is the actual porosity, $\boldsymbol{I}$ is the second order identity matrix, and *ettr*, *ht*, and *hg* stands for ettringite, hydrotalcite, and hydrogarnet, respectively. The expression accounts for the fact that ettringite forms at the expense of the dissolution of these two cement hydrates. In Equation (5-10),

$$\Delta\vartheta_i = \vartheta_i - \vartheta_{i,0}, i = ettr, ht, hg \tag{5-11}$$

where index 0 refers to the initial volume fraction at time 0. The actual porosity is calculated from mineral volume fractions, but neglecting the porosity reduction of secondary ettringite precipitating:

$$\varphi^* = \begin{cases} if\ \vartheta_{ettr} > \vartheta_{ettr,0}\ then\ \varphi + \Delta\vartheta_{ettr} \\ else\ \varphi \end{cases} \tag{5-12}$$

where φ is the porosity at any given time. Porosity is calculated from the reactive transport model as

$$\varphi = 1 - \sum_{i=1}^{n} \vartheta_i - \vartheta_{inert} \tag{5-13}$$

where n is the number of reactive minerals and ϑ_{inert} (m^3/m^3) is the volume fraction of inert minerals and aggregates. It is noted that most of the existing models consider the initial porosity, φ_0 (m^3/m^3). However, these models are typically used for simulating laboratory tests of short duration. In the present work, focusing on long-term degradation, porosity will change significantly over time due to calcium leaching. Therefore, an updated value of porosity is assumed in our model.

The model parameter β (varying between 0 and 1) represents the fraction of porosity that needs to be filled before any expansion is predicted. This parameter needs to be fitted with experimental data on a similar concrete, as presented in Section 5.3.

In some cases, where a source of carbonates is available in addition to a source of sulphates, thaumasite may form as well (Section 3.2). At present, thaumasite formed from sulphate attack has not been simulated with any of the models presented in Section 3.2. Thaumasite is expected to form to some extent in this study due to the presence of sulphate and carbonate in groundwater. As a first approximation, expansions due to thaumasite formation are modelled using a similar approach as for ettringite precipitation. To this end, the term $\Delta\vartheta_{ettr}$ in Equations 5-9 and 5-11 is replaced by $\Delta\vartheta_{ettr}+\Delta\vartheta_{thaum}$ (sub-index 'thaum' stands for thaumasite).

Expansions due to ettringite and thaumasite precipitation are implemented in Comsol as an imposed volumetric strain using the Hygroscopic Swelling feature of Comsol (COMSOL 2016).

5.2 Homogenization model for chemical damage

In the reactive transport models developed herein, the chemical composition of the concrete backfill varies with time as a result of interaction with groundwater. Consequently, it is expected that its mechanical properties will be modified as well. If dissolution of cement hydrates occurs, due to for instance calcium leaching, porosity will increase, while the stiffness and strength of the material will decrease. This degradation process has been defined in Section 3.1 as chemical damage. In this work, chemical damage is modelled using a multi-scale micro-mechanical model based on homogenization theory. It describes the effective properties at different material scales based on information about the morphology of the structure at a lower scale and the volume fractions of the different constituents. To this end, the model makes use of the results of reactive transport in terms of the solid composition of concrete.

Concrete may be regarded as a composite material at different scales. The scale of the largest heterogeneities in concrete is typically referred to the meso-scale. At this level, concrete can be treated as a continuous matrix made of mortar with large aggregate inclusions. In turn, mortar is made of a continuous matrix of hardened cement paste with embedded sand particles. An important component is the so-called interfacial transition zone (ITZ) that develops at the interface between sand particles and cement paste. This zone has a much more porous structure than bulk cement paste and is responsible for many features of the macroscopic behaviour of concrete (see e.g. Mehta and Monteiro 2006). At the microscopic level, hardened cement paste can also be regarded as a composite. At this scale, calcium silicate hydrates (C-S-H gel) that typically have the largest hydrate volume fraction, form a matrix that surrounds inclusions of the remaining hydrates and capillary porosity. These hydrates form from mixing water and (unhydrated) clinker such as C_2S, C_3S, C_4AF and C_3A particles. Upon hydration, part of the clinker is consumed, and cement hydrates are formed surrounding these particles.

These heterogeneities at multiple scales define the macroscopic properties (e.g. Constantinides and Ulm 2004). In particular, the elastic mechanical properties of concrete at the macroscopic scale can be defined as effective values starting from the elastic properties of its constituents, their volume fraction, and the morphology of the microstructure. That is the main purpose of homogenization theory, which is based on obtaining closed form solutions to the effective macroscopic properties of composites. Herein, the elastic mechanical properties of concrete at the macroscopic scale are obtained from its evolving chemical composition and the mechanical properties of the hydrates and aggregates.

A multi-scale approach is followed here, where heterogeneities are defined at four different levels: C-S-H, hardened cement paste (referred to hereafter as HCP), mortar, and concrete. Each level is treated as a heterogeneous medium at a different scale, ranging from the nano- to the macro-scale. To this end, the model originally proposed by Stora (2007), and further developed by Stora et al. (2010) and Bary et al. (2014), is implemented in iCP. Figure 5-1 and Figure 5-2 show a scheme of the multi-scale structure of concrete as a composite material considered in this model. Each level considers two or more phases that need to be homogenized to obtain the effective mechanical properties of the whole. The homogenized effective properties at a given scale serve as input to the properties of the corresponding constituent at the following larger scale.

At the nano-scale, the C-S-H gel level consists of inclusions of cement hydrates and capillary pores embedded in a C-S-H matrix. The coatings of HCP surrounding anhydrous particles and the ITZ of mortar surrounding sand particles are treated as composites. The second level is HCP that has three phases: an anhydrous core and inner and outer coatings. The third level is mortar, which is formed by spherical sand particles surrounded by an ITZ and embedded in a matrix of HCP. Finally, the fourth level is concrete, which consists of a mortar matrix with inclusions of the largest fraction of aggregates (> 8 mm). Three different homogenization schemes are used to better adapt the modelled microstructure at a given scale to experimental observations.

Each of these scales of analysis and their constituents are detailed in the following sections. The procedure used for calculating the constituent volume fractions of each phase is not straightforward. Therefore, only the main assumptions used in these calculations are given in the following paragraphs, while a more detailed description of how the volume fraction data are obtained is given in Appendix B.

5.2.1 Inner coating, outer coating, and ITZ

These three phases are very similar in the sense that they have similar components, although in different proportions.

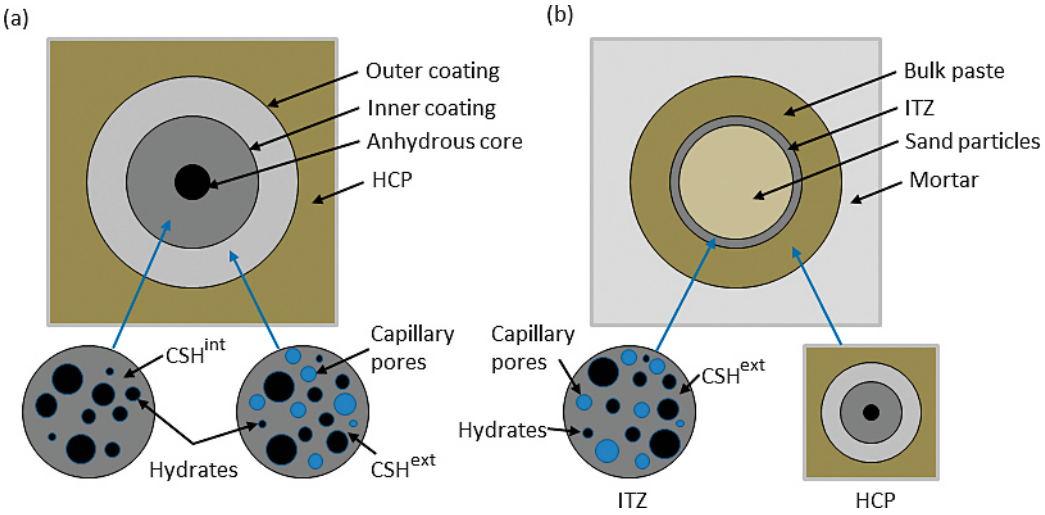

Figure 5-1. *Microstructural scheme and their phases, as considered in the multi-scale homogenization model for mortar (adapted from Bary et al. 2014). (a) hardened cement paste (HCP, top) and C-S-H (bottom) levels, showing the anhydrous particles surrounded by an inner coating and an outer coating. Size of HCP level: 10^{-6}–10^{-3} m. Size of C-S-H level: 10^{-9}–10^{-6} m. (b) Mortar level, showing the sand particles surrounded by a porous ITZ (size of the domain: 10^{-3}–10^{-1} m).*

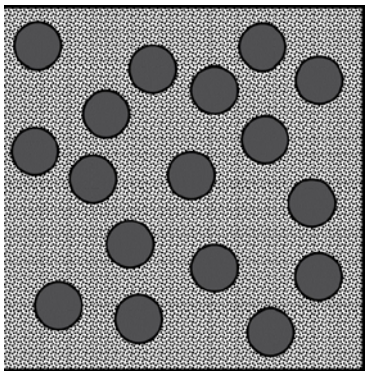

Figure 5-2. *Scheme of the concrete level (size of the domain: 10^{-1}–10^{0} m), composed of large spherical aggregate particles surrounded by a matrix of mortar.*

The **inner coating** consists of a high-density C-S-H matrix, or C-S-H^{int}, with inclusions of hydrates such as portlandite, ettringite, hydrotalcite, etc. Porosity at this level is only defined as gel porosity (< ~10 nm), i.e. porosity of the C-S-H treated as a porous structure. Larger capillary pores are not present at this level. Table 5-1 presents the composition of the inner coating used in the simulations. A value of 0.26 m^3_{gp}/m^3_{CSH} is used for gel porosity (gp), after Bary et al. (2014).

Table 5-1. Initial phase composition in volume fractions of the HCP inner coating constituents.

Constituent	Volume Fraction in Inner Coating (m^3/m^3_{IC})
C-S-H matrix	0.582
Inclusions (other cement hydrates)	0.418
Gel porosity (included in C-S-H)	0.151
Capillary Porosity	0.0
Total Porosity	0.151

The **outer coating** consists of a low-density C-S-H matrix, or C-S-H^{ext}, with inclusions of other cement hydrates and capillary pores. The difference between the high and low-density C-S-H matrices is their gel porosity volume, which is higher for C-S-H^{ext}. Table 5-2 presents the composition of the outer coating used in the simulations. A value of 0.38 m^3_{gp}/m^3_{CSH} is used for gel porosity (gp), after Bary et al. (2014).

Table 5-2. Initial phase composition in volume fractions of the HCP outer coating constituents.

Constituent	Volume Fraction in Outer Coating (m^3/m^3_{oc})
C-S-H matrix	0.511
Inclusions (other cement hydrates)	0.308
Gel porosity (included in C-S-H)	0.194
Capillary Porosity	0.182
Total Porosity	0.376

The interfacial transition zone (ITZ) develops between the sand particles and the hardened cement paste at the mortar level. It is composed of a more porous cement paste structure. Overall, it has a similar structure as the outer coating, but with a higher capillary porosity, as shown in Table 5-3.

Table 5-3. Initial phase composition in volume fractions of the ITZ constituents.

Constituent	Volume Fraction in ITZ (m^3/m^3_{ITZ})
C-S-H matrix	0.294
Inclusions (other cement hydrates)	0.177
Gel porosity (included in C-S-H)	0.112
Capillary Porosity	0.528
Total Porosity	0.640

The homogenization scheme used for these three phases is of the type matrix-inclusion and is based on the interaction direct derivative (IDD) scheme, assuming spherical inclusions (Stora et al. 2009, Zheng and Du 2001). The initial volume fractions are calculated considering the following assumptions:

- The distribution of C-S-H between low-density (64.3 %) and high-density (35.6 %) is calculated based on the cement hydration model by Tennis and Jennings (2000) and using a water-to-cement ratio of 0.47 (Höglund 2001).
- The volume fractions of low-density C-S-H and capillary porosity were distributed between the outer coating and the ITZ such that the total porosity of the ITZ equals 64 %, as proposed in Bary et al. (2014).

With this model, the mechanical properties of the three phases change with time as a function of the volume fraction of its constituents, as given by the reactive transport model. For these phases, the constituents are C-S-H, other cement hydrates and porosity. Volume changes resulting from mineral dissolution and precipitation impact the capillary porosity. In turn, gel porosity is also modified if the volume fraction of C-S-H is altered. In this way, the model yields not only the evolution of total porosity, but also of the bimodal pore size distribution (gel and capillary pores).

5.2.2 Hardened cement paste (HCP)

As mentioned above, the homogenization scheme used for hardened cement paste is based on the Generalized Self-Consistent Scheme or GSCS (Stora et al. 2009, Christensen and Lo 1979) and is composed of an unhydrated clinker core, surrounded by an inner and an outer coating. The volume fractions considered in this study are given in Table 5-4. The value for unhydrated clinker was obtained with the Tennis and Jennings (2000) hydration model mentioned before.

Table 5-4. Initial phase composition in volume fractions of the HCP constituents.

Constituent	Volume Fraction in HCP (m^3/m^3_{HCP})
Unhydrated Clinker	0.049
Inner Coating	0.315
Outer Coating	0.636
Gel Porosity	0.171
Capillary Porosity	0.116
Total Porosity	0.287

5.2.3 Mortar

Mortar is composed of sand particles surrounded by an ITZ layer and a HCP matrix. The volume fractions of the three phases used in the simulations are given in Table 5-5. The homogenization scheme used in this case is also the GSCS, as in the case of HCP.

The volume fraction of ITZ is assumed to be 0.09, as assumed in Bary et al. (2014).

Table 5-5. Initial phase composition in volume fractions of the mortar constituents.

Constituent	Volume Fraction in Mortar (m^3/m^3_{mortar})
Sand	0.531
ITZ	0.090
HCP	0.379

5.2.4 Concrete

Finally, concrete is homogenized using the classical matrix-inclusion type Mori-Tanaka scheme (Mori and Tanaka 1973), which has been used before for cementitious composites (Bary 2008, Pichler et al. 2008). Concrete composition is given in Table 5-6. In this table, the composition of the cement paste fraction of concrete corresponds to the full chemistry case in Idiart and Shafei (2019). The list of secondary minerals included in the reactive transport model (i.e., minerals that are allowed to precipitate), and their elastic properties are given in Table A-1 of Appendix A.

The fraction of sand and aggregates in mortar and concrete were calculated with the data given by Höglund (2001, 2014), and are gathered in Table 5-7. The mechanical properties of the inert phases in concrete (that is, unhydrated clinker, sand, and aggregates) are given in Table A-1 of Appendix A.

Table 5-6. Initial phase composition in volume fractions of the concrete constituents.

Constituent	Volume Fraction in Concrete (m^3/m^3_{concr})
Large aggregates	0.3460
Mortar	0.6540
Cement hydrates	
Portlandite	0.0529
CSHjen	0.0943
Ettringite	0.0085
HydrogarnetSi	0.0149
Thaumasite	0.0116
HydrotalciteOH	0.0037

Table 5-7. Ballast (sand and aggregates) size distribution and mixing proportions (kg/m3) in concrete (Höglund, 2001, 2014).

Size of ballast	Mixing proportion (kg/m^3)	Density (kg/m^3)	Volume fraction in concrete (m^3/m^3_{HCP})
0–8 mm (sand)	920	2648	0.347
8–32 mm (aggregates)	909	2630	0.346

The final distribution of porosity types at different homogenization levels resulting from the model are summarized in Figure 5-3. As a summary, the different homogenization levels considered in the model of chemical damage at the concrete level are graphically shown in Figure 5-4, together with their corresponding homogenization schemes and components.

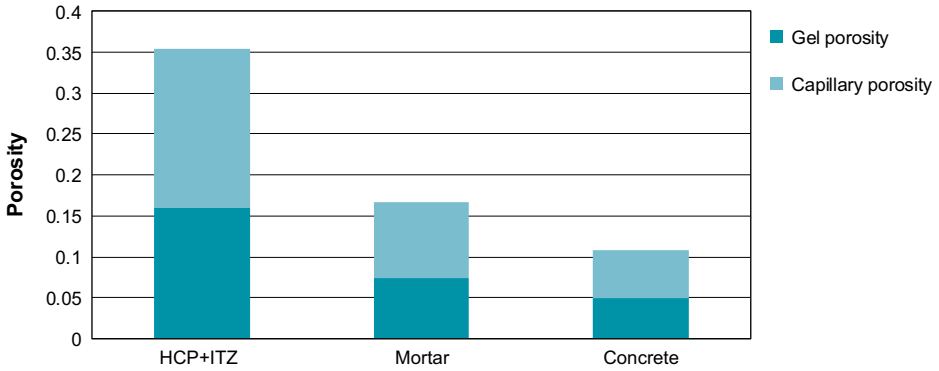

Figure 5-3. *Summary of the distribution of total porosity into gel and capillary porosity at different homogenization levels. The water-to-cement ratio is 0.47.*

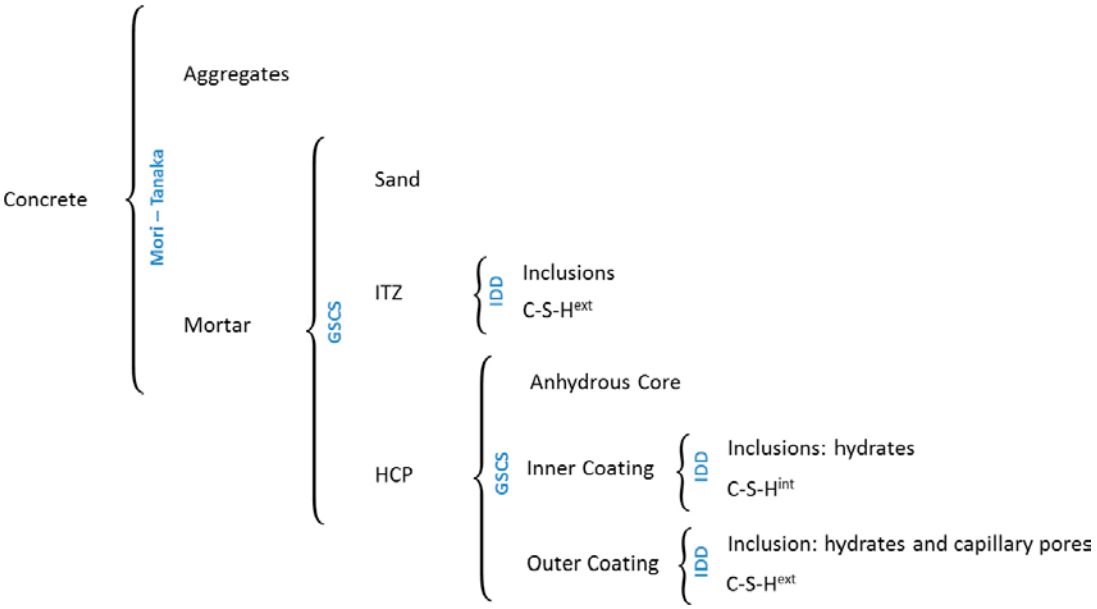

Figure 5-4. *Summary of the different homogenization levels considered in the HCM model and their corresponding schemes and components. The Mori-Tanaka and Interaction Direct Derivative (IDD) schemes are of the type matrix-inclusion. The Generalized Self-Consistent Scheme (GSCS) considers doubled-coated spheres.*

5.3 Verification cases

5.3.1 Regularized Mazars' damage model

The isotropic Mazars' damage model is used to simulate the nonlinear mechanical behaviour of concrete. This damage model is included in Comsol in version 5.2 as an External Material library. However, a new implementation scheme within Comsol is proposed, mainly motivated by the need of more flexibility to couple different processes in a single model, such as other mechanical constitutive laws. More details are given in Section 5.1.1.

5.3.1.1 Loading/unloading cycles in uniaxial compression test

A verification example is presented below to check the suitability and robustness of the new implementation and compare the results with the External Material Function approach. The example consists of a uniaxial compression test of a cylindrical concrete sample, simulated using an axisymmetric setup (Figure 5-5). The compressive load is applied as an imposed displacement on the top of the specimen to allow capturing of the softening branch. A sinusoidal variation of the imposed displacement as a function of time is imposed, with an amplitude that linearly depends on time, see Figure 5-5. This is done to model multiple loading/unloading cycles and check that the mechanical damage properly accumulates (slope of the unloading branch). The boundary conditions are as follows: axial symmetry in the inner edge, roller in the bottom surface, and prescribed displacement on the top surface. The external vertical boundary is free.

The elastic properties of the material and the parameters of the Mazars' damage model used in the simulation are shown in Table 5-8. The specimen has a height of 10 cm and a radius of 3 cm. The mesh consists of regular quadrilateral quadratic finite elements. A time dependent study is used to gradually impose displacement, although the mechanical model does not depend on time. The time dependent solver is also required to compute history variables (previous time step results are needed).

Table 5-8. Material properties and Mazars' damage model parameters used in the verification test.

Material properties	**Value**
Undamaged Young's module	30 (GPa)
Undamaged Poisson's ratio	0.2
Mazars' parameters	
ε_0	1.0×10^{-4}
A_t	1.0
B_t	15000
A_c	1.2
B_c	1500

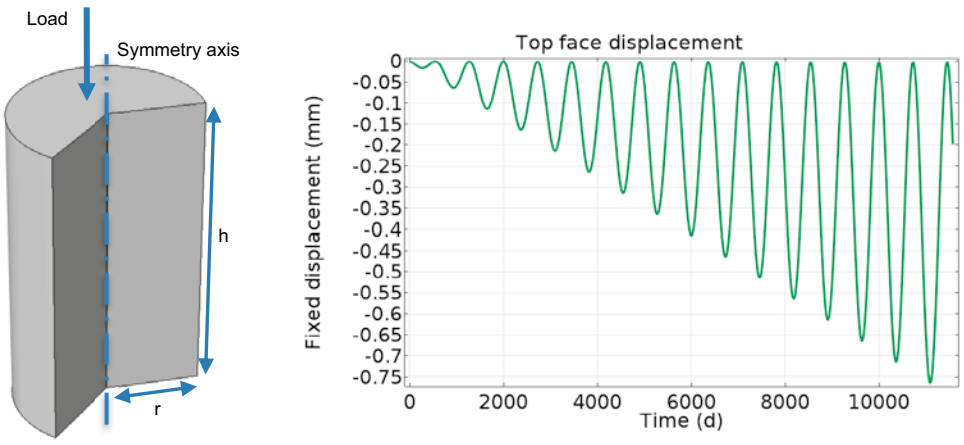

Figure 5-5. *Specimen geometry and description of used fixed displacement to simulate cyclic loading and unloading conditions. Dimensions of h and r are 10 and 3 cm, respectively.*

The comparison of the results obtained using the two different implementation approaches is presented in Figure 5-6 in terms of the stress-strain curve. Very good agreement is observed between the two sets of results. Therefore, it may be concluded that the new implementation correctly captures the nonlinear behaviour of Mazars' damage model. In the remaining of this report, all results presented are obtained using the new implementation method.

5.3.1.2 Biaxial loading under plane stress

Loading under biaxial stress states has also been tested with the model, ranging from tensile-tensile to compressive-compressive loading. It is known that the Mazars' damage model under plane stress underestimates the strength of concrete under biaxial compression (e.g. Jirásek 2011). The results of the Mazars' damage model implemented in Comsol under plane stress conditions for different biaxial loads are compared to classical experimental data from Kupfer et al. (1969) in Figure 5-7. The results are presented in terms of the maximum stress in each loading direction relative to the uniaxial compressive strength, f_c (negative sign corresponds to compressive stresses). It is clearly observed that under biaxial compression and plane stress conditions the model predicts a significantly lower concrete strength. The experiments show that the strength of concrete under biaxial compression is higher than the uniaxial compressive strength.

Importantly, it is noted that damage is only accumulated in the model in the event of positive strains (Equation 5-5). Under plane stress bi-compression, positive strains can develop in the out-of-plane direction in Figure 5-7 (right). The assumption of plane stress conditions ($\sigma_z = 0$, $\varepsilon_z \neq 0$), is a good approximation when the structure analysed resembles a slab (dimension in z-direction much smaller than the other two directions).

However, for a tunnel lining structure such as BHK, the dimension in the z-direction is much larger than the other two directions defining a cross-section. In such a case, the assumption of plane strain should be used instead ($\sigma_z \neq 0$, $\varepsilon_z = 0$). In this case, no positive strains are allowed in the z-direction when a cross-section is loaded under biaxial compression. This loading state can be regarded as a confined or triaxial compression stress-state. Therefore, no damage will be predicted by the model in this case (e.g. Pijaudier-Cabot and Mazars 2001), unless tensile stresses develop in some region of the concrete backfill. Stresses can nonetheless be monitored to verify whether the triaxial compressive strength at a given level of confinement is reached (e.g. Gabet et al. 2008, Mazars et al. 2015).

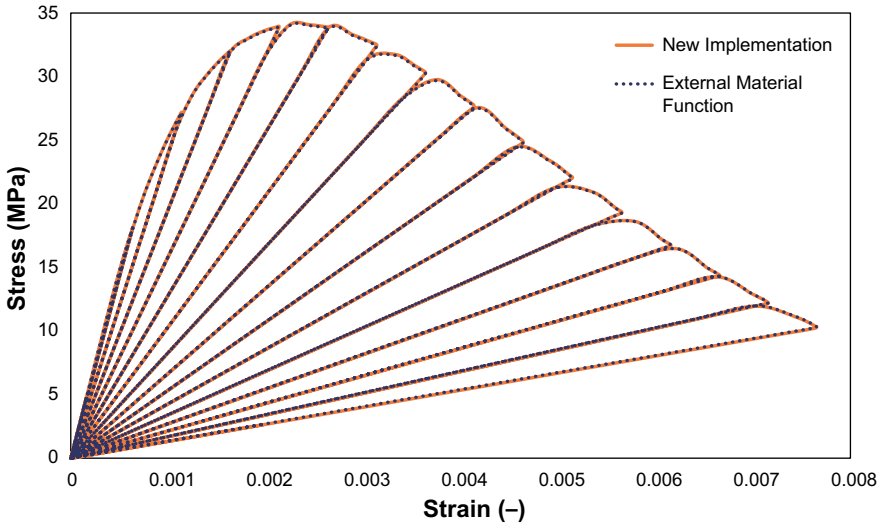

Figure 5-6. *Results of the verification test in terms of stress-strain curves using two different damage model implementations.*

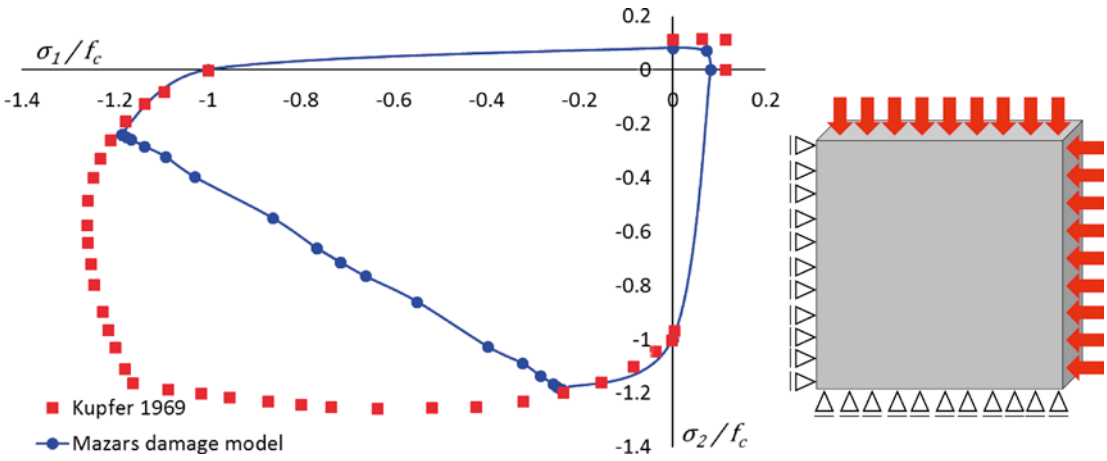

Figure 5-7. *Comparison of the results of several biaxial loading tests from Kupfer et al. (1969) and the implemented Mazars' damage model (left), showing an underestimation of the strength of concrete under biaxial compression. Schematic view of the test (right), showing the geometry and boundary conditions (imposed displacements, in the figure corresponding to compression-compression).*

5.3.1.3 Three-point bending tests

Another important aspect of the damage model and its implementation is the use of a regularization technique to minimize or eliminate mesh dependency of the results (Section 5.1.2). The implicit gradient formulation (Peerlings et al. 1996) described in Section 5.1.2 is tested with a set of 4 verification examples using the regularized Mazars's damage model. Three-point bending tests of notched and unnotched concrete beams are modelled using the regularized model and the model without any regularization. A total of four studies are analysed:

- Study 1: notched beam with local (non-regularized) damage model.
- Study 2: unnotched beam with local damage model.
- Study 3: notched beam with regularized damage model.
- Study 4: unnotched beam with regularized damage model.

For each case, several simulations are performed with different refinement of the finite element mesh. With these examples, both the Mazars' damage model implementation and its regularization scheme are tested.

The concrete beams have a square cross-section of 10×10 cm^2 and a length of 45 cm. The notched beam has a notch of 0.5 cm wide and 5 cm deep at bottom centre. This kind of tests has been widely studied experimentally and computationally by several authors (Kormeling and Reinhardt 1983, Jirásek 2011).

The simulations consider a 2D geometry, as shown in Figure 5-8. In all cases the load (imposed displacement) is applied from above, in the middle of the beam. The mechanical properties and damage model parameters are shown in Table 5-9, which are the same as those proposed by Jirásek (2011). Even though the parameters for notched and unnotched beams differ slightly, the goal is to compare the results of the models developed here with those obtained by Jirásek (2011).

The boundary conditions are set up as follows: bottom left corner is fixed; vertical displacement of bottom right corner is set to 0; all other boundaries are free, except for the loading point where vertical displacement is prescribed to simulate the loading process.

Table 5-9. Mechanical parameters and damage model parameters in the four beam tests.

Mechanical properties	Notched	Unnotched
Undamaged Young's module	20 (GPa)	
Undamaged Poisson's ratio	0.2	
Damage model parameters	**Notched**	**Unnotched**
ε_0	1.2×10^{-4}	0.9×10^{-4}
ε_f^*	0.007	0.003
A_c	1.09	
B_c	1 500	
l (mm)	0.6	1.0

** Equation 5-2 for computing tensile damage is replaced by* $d_t(\tilde{\varepsilon}) = 1 - \frac{\varepsilon_0}{\kappa} \cdot exp\left(-\frac{\kappa - \varepsilon_0}{\varepsilon_f - \varepsilon_0}\right)$.

Meshing is a key issue in the present set of examples. As shown in Figure 5-8, several subdomains are included in the geometry to increase control of the meshing process (Jirásek 2011). At least three different meshes are generated for each study to obtain an adequate number of solutions to draw meaningful conclusions. In the central part of the beam, where the nonlinearities occur, a refined mesh is used. At the leftmost and rightmost sides a coarser discretization is enough. The element size changes from coarse to fine in a transition region. All studies are carried out with quadrilateral quadratic elements. In some examples, slightly coarser elements are used for the unnotched beam. The finite element sizes used for the 4 studies are: 15 mm, 5 mm, 2.9 mm, 1.67 mm, and 0.55 mm. Results for each study are presented in terms of load (N) vs. displacement curves measured at the point where the load is applied.

The experimental results are shown in Figure 5-9 for the notched beam. For comparison, the model results from Jirásek (2011) are also included.

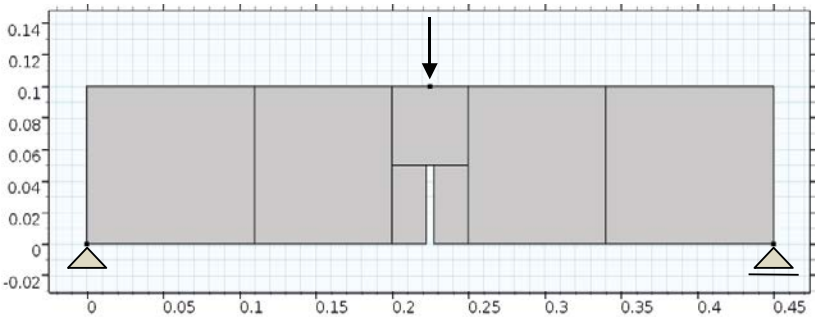

Figure 5-8. *Geometry of the notched beam under three-point bending, showing boundary conditions and auxiliary inner subdomains to improve meshing. Dimensions are in meters.*

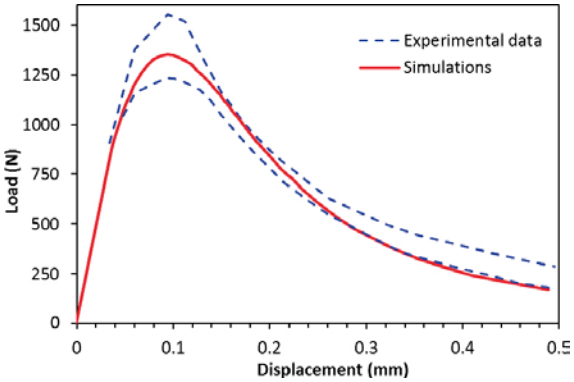

Figure 5-9. *Load (N) vs. displacement (mm) curves of the notched three-point beam test: model results adapted from Jirásek (2011) in solid line and experimental results (Kormeling and Reinhardt 1983) in dotted line.*

Next, the results of the 4 Comsol studies are presented, beginning with the local damage models to end with the regularized models. Study 1 shows how the results are highly dependent on the selected mesh when no regularization is used. Results are presented in Figure 5-10, where a qualitative comparison with the model results from Jirásek (2011) is also included. The solution using 5 mm elements is close to the experimental results of Figure 5-9. However, as mesh is refined the curve changes considerably. Both the peak load and the total dissipated energy (area under the curve) decrease as element size is reduced. These results clearly show the sensitivity of the model on mesh refinement and serve as an additional verification of the Mazars' damage model implementation. Although mesh dependence makes this local formulation unusable, comparison with other local damage models shows a very good agreement.

Figure 5-11 presents the results of Study 2 from which similar conclusions as for Study 1 can be drawn. Without regularization, the damage model results in different peak loads as mesh changes. The model convergence is also sensitive to the element size, resulting in stability problems in the post-peak regions for finer meshes (similar to Jirásek 2011, not shown). The loss of convergence is due to the abrupt change of the strain increment distribution from a smoothly distributed to highly localized (Jirásek 2011).

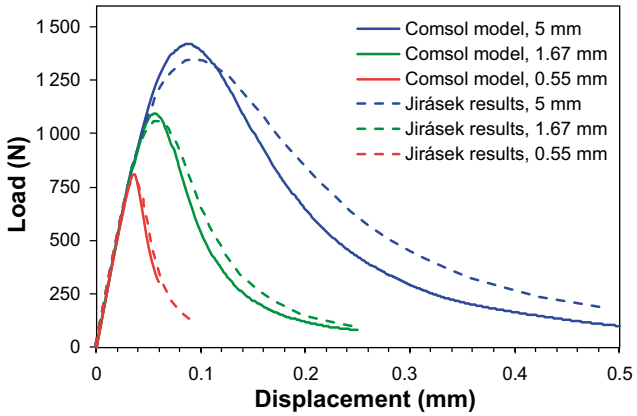

Figure 5-10. *Load (N) vs. displacement (mm) curves of the notched three-point beam test with no regularization method: results of the Comsol model for different mesh refinements and comparison with results from Jirásek (2011).*

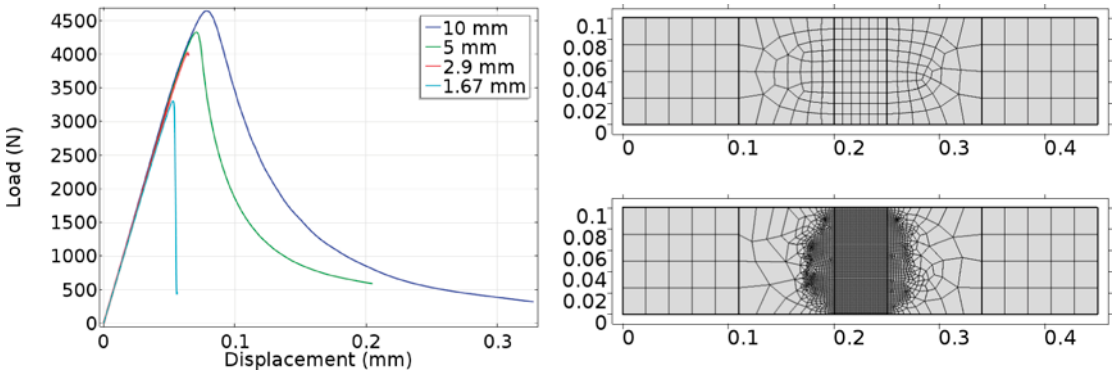

Figure 5-11. *(Left) Load (N) vs. displacement (mm) curve of the unnotched three-point beam test with no regularization method. Results are shown for different mesh refinements. (Right) Example of two meshes with different element size in the central area of 10 mm (top) and 1.67 mm (bottom).*

Studies 3 and 4 consider the regularized damage model. Results are presented in Figure 5-12. With the implicit gradient formulation, the results are much more objective and little mesh dependence is observed. In Study 3 the two finer meshes adequately match, although this does not hold for the coarsest mesh (5 mm element size). In the latter, the element size is substantially larger than the characteristic length used (l = 0.6 mm), which probably explains the disagreement between the results.

In contrast, Study 4 shows a remarkable agreement in the peak load and improved convergence of the total dissipated energy as element size is reduced. In this case, the characteristic length is larger (l = 1 mm), which may in part explain why coarser meshes agree better with finer ones.

The results in studies 3 and 4 correspond exactly with the regularized test reported by Jirásek (2011) when comparing load-displacement curves. Therefore, it is concluded that the regularized mechanical damage model implementation works properly. Finally, the mechanical damage evolution is compared to the results in Jirásek (2011) in Figure 5-13. The figure shows how mechanical damage is generated and propagated through the middle section of the unnotched beam at different load steps.

A similar analysis is performed with the notched beam (Figure 5-14). Similar conclusions as in the previous plot can be drawn: mechanical damage propagates through the notched plane of the beam reaching values close to 1 when the load-bearing capacity is almost exhausted.

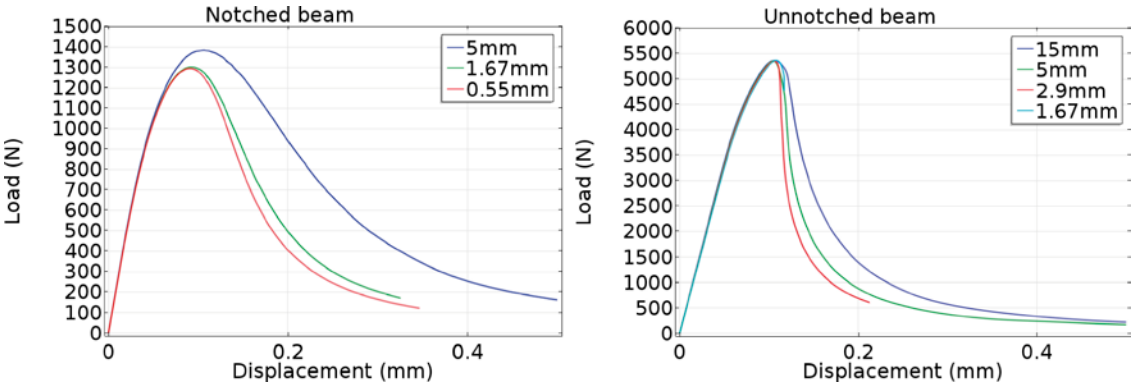

Figure 5-12. *Load (N) vs. displacement (mm) curves of the regularized damage model, notched (left) and unnotched (right) beam tests. Results are shown for different mesh refinements.*

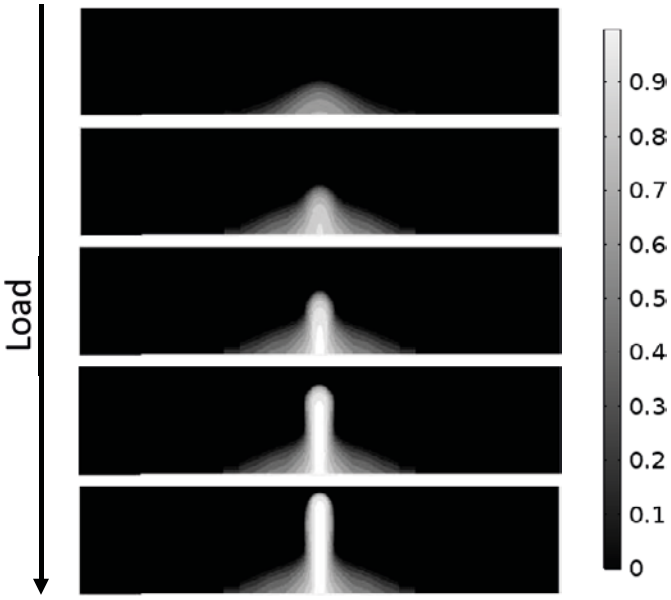

Figure 5-13. *Unnotched beam: results of the evolution of mechanical damage in the regularized damage model in Comsol (Study 4), results in good agreement with those presented in Jirásek (2011).*

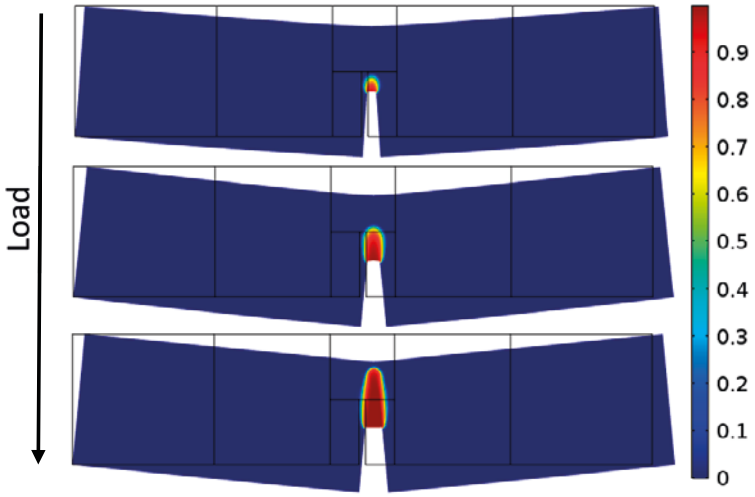

Figure 5-14. *Notched beam: evolution of mechanical damage with increasing load in Study 3.*

5.3.2 Calcium leaching

Calcium leach is one of the main degradation processes affecting concrete in deep geological repositories. In this section, the chemo-mechanical model for calcium leaching (see sections 5.1 and 5.2) is used to simulate laboratory experiments of accelerated calcium leaching recently carried out (Babaahmadi 2015). Calcium leaching is very slow, laboratory experiments are typically performed using aggressive leaching solutions, e.g. deionized water or different concentrations of ammonium nitrate (Adenot and Buil 1992, Faucon et al. 1996). Babaahmadi (2015) used an electrochemical migration apparatus with an aggressive solution of ammonium nitrate to accelerate the dissolution and transport of calcium ions in cement paste, mortar, and concrete specimens. Relatively large specimens could be used for macroscopic characterization tests. Cylindrical specimens were cast with a diameter of 50 mm and a length of 75 mm, except the concrete specimens used for measuring the tensile strength (using the splitting test based on the American standard ASTM C49). The cement used was Swedish structural ordinary Portland cement (CEM I 42.5N SR3/MH/LA). This cement is similar to the Degerhamn Anläggningscement used for concrete constructions in the in the SFR repository and planned to be used in the SFL repository (see Table 5-10). This cement was mixed with different water-to-cement ratios, although the present analysis is restricted to a ratio of 0.48 for concrete specimens and 0.5 for paste and mortar specimens.

Table 5-10. Chemical composition of cement used in experiments by Babaahmadi (2015) and Degerhamn Anläggningscement.

Component	Content % by weight	
	Babaahmadi (2015) experiments	Cement used in 1BMA
Ca	64	64
SiO_2	22.2	21
Al_2O_3	3.6	3.5
Fe_2O_3	4.4	4.6
MgO	0.94	0.7
K_2O	0.72	0.62
Na_2O	0.07	0.07
SO_3	2.2	2.2
Cl	0.01	< 0.1

Sample characterization was carried out before and during the aging process. Tests included microstructural characterization, macroscopic mechanical tests, and determination of hydraulic and transport properties (see Table 5-11). The accelerated leaching experiments were run until portlandite was entirely depleted. Only partial degradation of the C-S-H gel was observed. More details can be found elsewhere (Babaahmadi et al. 2015).

Table 5-11. Characterization techniques used in the experiments by Babaahmadi et al. (2015).

	Chemical properties				Transport properties						Mechanical properties			
Material	IC & PT	XRD	LA-ICP-MS	SEM-EDX	MIP & Gas Sorption	Freezable Water	Diffusion Cell Tests	Diffusion Adsorption Test	Gas Permeability	Water Permeability	Tensile Strength	Compressive Strength	Elastic Modulus	Resonant Frequency
HCP	✓	✓	✓	✓	✓	✓	✓	✓	X	X	X	✓	X	✓
Mortar	✓	✓	✓	✓	✓	✓	X	X	X	X	X	✓	X	✓
Concrete	✓	✓	✓	✓	✓	X	X	X	X	✓	X	✓	✓	✓
	✓	✓	✓	✓	✓	X	X	X	✓	X	✓	X	X	X

The leaching experiments are simulated using the chemo-mechanical model considering a 2D axisymmetric setup using iCP. The model considers solute transport, chemical reactions, a chemical damage model (based on homogenization), and a mechanical damage model. Two important differences between the model and experimental setup need to be mentioned:

- Electrochemical migration is not modelled: given that the experiments were accelerated by means of an imposed electrical current, a proper representation of this system should include the electrochemical migration effect, i.e. the Nernst-Planck equations, and adapted boundary conditions (e.g. Liu et al. 2012).
- Composition of the solution: in the experiments, ammonium nitrate is used to further accelerate the dissolution process. In this study, an actual groundwater composition is used.

The model does not intend to reproduce the accelerated experiments in terms of the time needed to reach an aged sample. The goal is rather to determine the acceleration factor obtained affecting leaching in the experimental setup. In addition, the outcome of the model in terms of chemical and physical properties of the aged samples can be compared to the experimental results.

For these experiments, solute transport is limited to Fickian diffusion. The initial effective diffusivity used for the concrete specimens is 2.8×10^{-12} m^2/s, which is close to typical values for intact concrete with a water-to-cement ratio of 0.5 (Costa and Appleton 1999, Nguyen et al. 2006, Zheng et al. 2009). Aqueous speciation and mineral dissolution/precipitation are calculated at chemical equilibrium using the PhreeqC format of the thermodynamic database CEMDATA07 (Lothenbach et al. 2008, Jacques 2009). Changes in porosity due to chemical reactions are explicitly considered as well as their impact on transport properties. Diffusion-driven leaching of concrete and cement paste samples is simulated in a 2D axisymmetric setup using a finite element mesh with a maximum element size of 2.5 mm. The porewater and boundary groundwater compositions are presented in Table 5-12 and the mineralogical composition in Table 5-13.

Table 5-12. Groundwater (from Pękala et al. 2015) and cementitious porewater composition used in the numerical simulations. The porewater is initially in equilibrium with the minerals in Table 5-13.

Component	Groundwater	Porewater
pH	8.64	12.975
Totals	Concentration (mol/L)	
Al	1.21×10^{-6}	5.54×10^{-7}
C	6.91×10^{-4}	1.00×10^{-5}
Ca	5.26×10^{-4}	3.68×10^{-3}
Cl	4.54×10^{-3}	5.55×10^{-5}
K	7.60×10^{-5}	8.84×10^{-2}
Mg	1.48×10^{-4}	2.53×10^{-8}
Na	4.79×10^{-3}	2.70×10^{-2}
S(VI)	3.73×10^{-4}	3.29×10^{-3}
Si	1.42×10^{-4}	4.52×10^{-5}

Table 5-13. Mineralogical composition of the cement paste used in the numerical simulations.

HCP minerals and porosities	Volume fractions
Portlandite	0.176
CSHjen	0.314
Ettringite	0.029
HydrogarnetSi	0.050
Thaumasite	0.039
HydrotalciteOH	0.012
Unhydrated Clinker	0.049
Gel porosity	0.163
Capillary porosity	0.167
Total Porosity	0.330

The C-S-H gel is modelled using two discrete phases with different Ca/Si ratios, i.e. CSHjen with Ca/Si = 1.66 and CSHtob2 with Ca/Si = 0.83 (see Appendices A and B for more details). Capillary porosity increases when decalcification of C-S-H takes place following the different molar volumes of the discrete phases (Appendix A). In turn, gel porosity is proportional to the volume of C-S-H in the cement paste. The inner (i.e. high-density) and outer (i.e. low-density) C-S-H gels have a gel porosity of 0.26 and 0.38 m^3_{gp}/m^3_{CSH}, respectively.

First, the evolution of the modelled and experimental results is compared in terms of the profile of the Ca/Si ratio along the cement paste sample axis. These results, whose aim is to verify the reactive transport model, are presented in Figure 5-15. As the experiments were accelerated due to electrochemical migration, the corresponding model times were found by comparing the time at which portlandite was completely leached: 53 days in the experiments and 11 000 years in the modelled results. The relation between model and experimental times was assumed to be linear. It can be seen that the initial and final times obtained with the reactive transport model offer a good fit with the experimental results. At intermediate times the tendency is similar, but the leaching depth differs slightly. A more accurate relation between modelled time and experimental time would probably lead to a better comparison.

Figure 5-16 shows the mineral composition of the cement paste sample expressed in volume fractions along the axis, obtained with the model after 7 264 years. The corresponding profile of Ca/Si ratio is presented in Figure 5-15. The portlandite dissolution front has advanced 45 mm, while ettringite is dissolved in the first 40 mm. CSHjen is gradually replaced by CSHtob in the first 30 mm. These mineralogical changes induce a porosity increase in the sample, from the initial 0.33 to a maximum of 0.63, and a decrease in Ca/Si ratio.

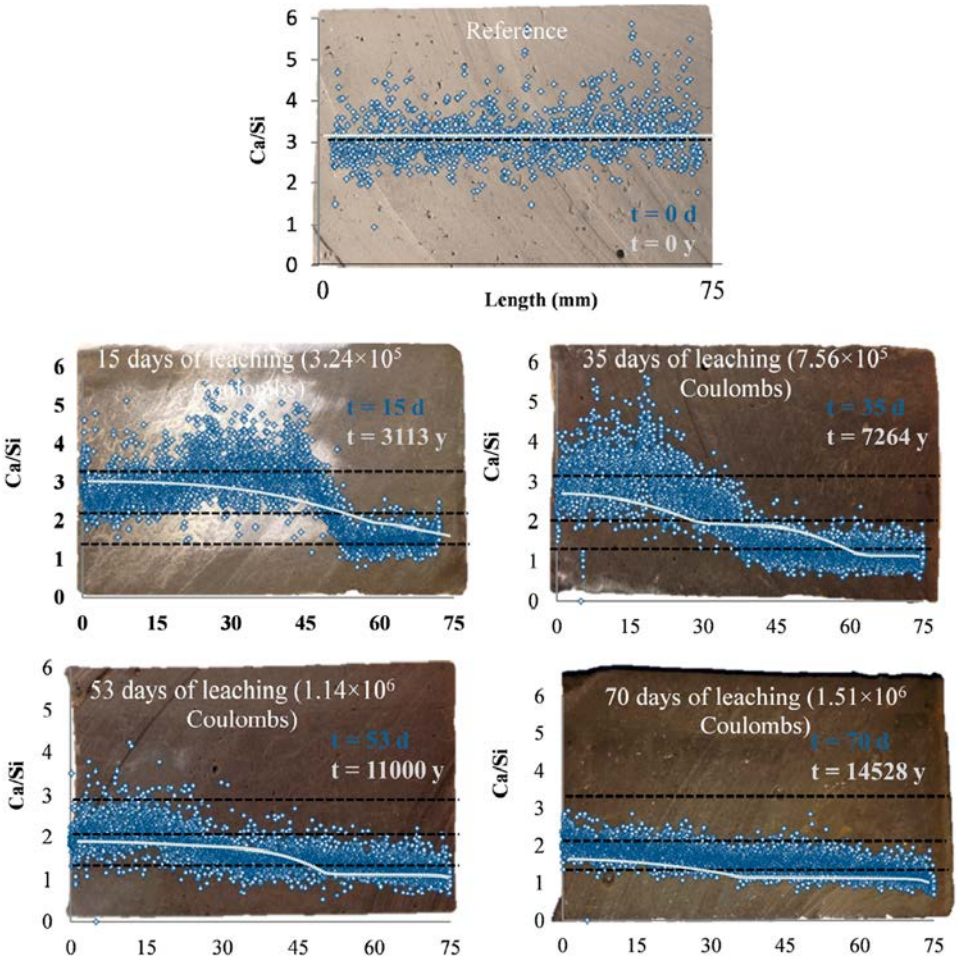

Figure 5-15. *Calcium-to-Silicon ratio profiles in the cement paste specimens obtained at different times from laboratory experiments (blue dots, adapted from Babaahmadi 2015) and the chemo-mechanical model (grey lines). Times in blue and light grey correspond to experimental data and model results, respectively. Horizontal dimension is given in mm.*

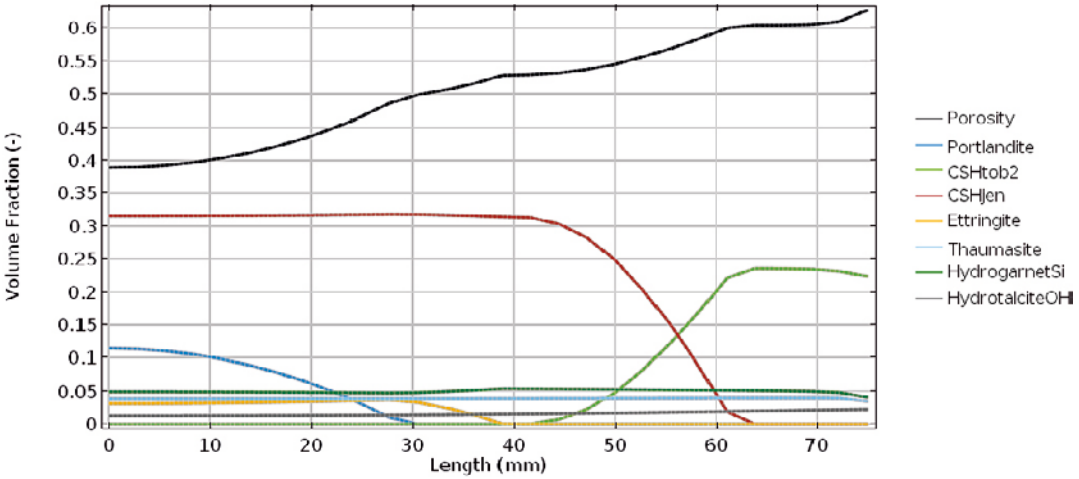

Figure 5-16. *Porosity and mineral volume fractions in hardened cement paste obtained with the chemo-mechanical model at time t = 7264 years.*

The homogenization model for simulating chemical damage is verified by comparing modelled and experimental results of the Young's modulus of the initial and leached specimens (Table 5-14). Experimental results from the leached specimens were obtained after about 53 days, when measurements indicated that all the portlandite had been leached out. The model results in Table 5-14 correspond to the Young's modulus of the leached specimen measured at the centre of the specimen, after the stiffness reaches a constant value (2400 years in Figure 5-17). Comparing the two plots in Figure 5-17, it is clear that during the first 1000 years of leaching, the Young's modulus decreases due to portlandite and ettringite dissolution and the induced increase in porosity. The next 1000 years the porosity keeps increasing as a result of C-S-H matrix degradation. This degradation induces a second phase of decrease in Young's modulus.

Overall, a good agreement between model and experimental results is found, both for initial and leached specimens (see Table 5-14). The main difference between experimental and modelled results is the initial Young's modulus of the HCP. A very low value (11 GPa) has been measured experimentally. However, reported experimental values by other authors at this w/c ratio and for an almost complete degree of hydration show systematically higher values, on the order of 20 GPa or more (e.g. Sanahuja et al. 2007, Haecker et al. 2005). In fact, this difference is reduced significantly for mortar and concrete. In particular, the results of the homogenization model at the concrete level at the initial and aged states show a very good agreement.

Table 5-14. Young's modulus of concrete, mortar and HCP before and after leaching and the percentage of decrease obtained by means of experiments (Babaahmadi 2015) and the calcium leaching model.

Sample		Initial Young's modulus (GPa)	Leached Young's modulus (GPa)	Chemical damage
Concrete	HCM Model	42.6	20.3	0.52
	Experimental	46.5	24.1	0.48
Mortar	HCM Model	37.7	13.2	0.65
	Experimental	30.4	15.2	0.50
HCP	HCM Model	26.6	5.95	0.78
	Experimental	11.4	6.24	0.45

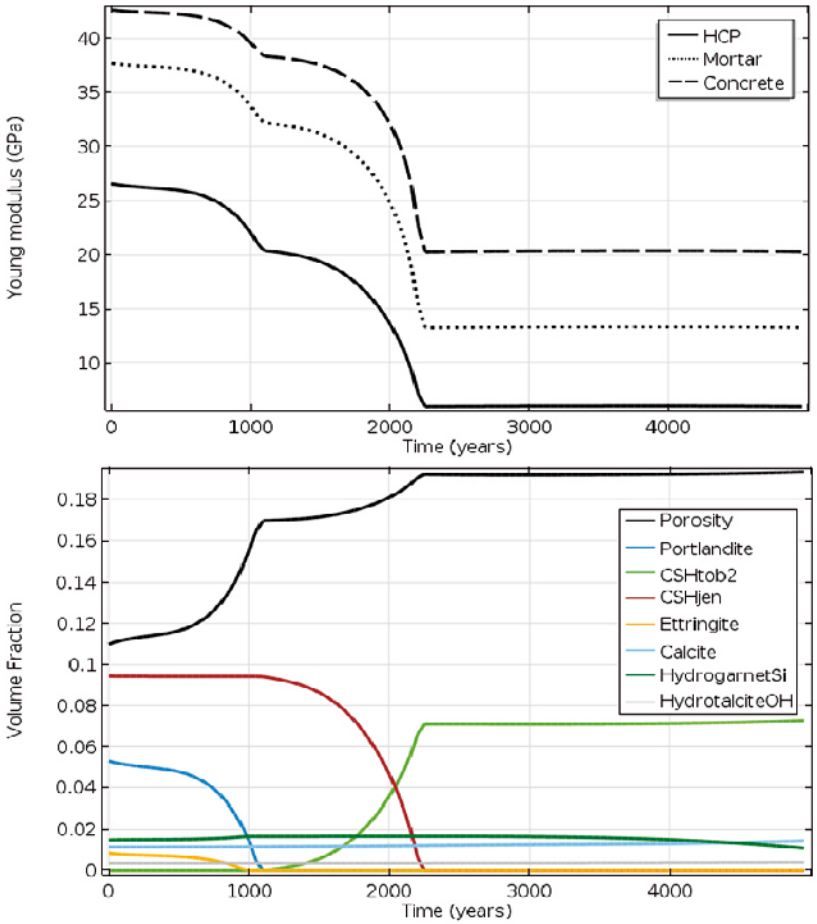

Figure 5-17. *Time evolution at the centre of the concrete specimen according to the chemo-mechanical model: (top) Young's modulus (GPa) at the concrete, mortar, and HCP levels, and (bottom) porosity and mineral volume fractions.*

Finally, the mechanical damage model of Mazars is used coupled to the chemical damage model to determine the compressive and tensile strength of intact and aged concrete specimens. The Mazars' model parameters are chosen such that the compressive and tensile strengths of concrete match those measured by Babaahmadi (2015), see Table 5-16. Moreover, the damage model parameters for compression are subject to the constraint given by Equation (5-4) (Jirásek 2011).

The fitted parameter values are listed in Table 5-15. The stress-strain curves are plotted in Figure 5-18 and Figure 5-19 for compressive and tensile tests, respectively. Comparison with experimental data is presented in Table 5-16 in terms of strength. The modelled compressive strength of the aged concrete is 17 MPa, whereas the experimental result is 12.7 ± 0.1 MPa. In turn, the modelled tensile strength of the aged sample is 4.4 MPa, while the experimental result is 2.8 ± 0.1 MPa. The modelled degraded strengths are thus between 30 and 60 % higher than the measured values.

The evolution of the effective diffusion coefficient is also compared to experimental data. The effective diffusion coefficient of the model increased from 2.8×10^{-12} to 11.3×10^{-12} m^2/s due to the increase in porosity resulting from mineral dissolution. The effective diffusion values reported by Babaahmadi et al. (2014) are significantly higher (roughly by an order of magnitude) and not typical of intact concretes with similar water-to-cement ratios. However, the ratio of diffusivities between aged and intact concrete specimens are very similar, as shown Table 5-16.

The results obtained from the simulation of the calcium leaching experimental tests presented in this section show that the chemo-mechanical model is able to capture the main features of the mechanical behaviour of intact and aged specimens. The chemical dissolution processes follow similar patterns, although the kinetics of degradation is completely different due to the acceleration method based on electrochemical migration and ammonium nitrate solution used in the experiments.

Table 5-15. Parameters used in Mazars' damage model.

Material properties	
Undamaged Young's module	42.6 (GPa)
Undamaged Poisson's ratio	0.22
Mazars' parameters	
ε_0	1.24×10^{-4}
A_t	1.36
B_t	2 135
A_c	0.95
B_c	2 200

Table 5-16. Uniaxial compressive and tensile strength of concrete samples for intact (reference) and aged states: comparison between experiments (Babaahmadi 2015) and model results. Tensile strength determined using the splitting test on concrete samples with 10 cm diameter and 5 cm height.

Concrete sample	**Compressive strength (MPa)**		**Tensile strength (MPa)**		**Effective diffusion coefficient aged/intact ratio**
	Intact	**Aged**	**Intact**	**Aged**	
HCM Model	43.17	16.98	10.20	4.37	4.05
Experimental	43 ± 0.3[1]	12.7 ± 0.1[1]	10.2 ± 0.1[1]	2.8 ± 0.1[1]	> 3.94[2]

1. Babaahmadi (2015); 2. Babaahmadi et al. (2014).

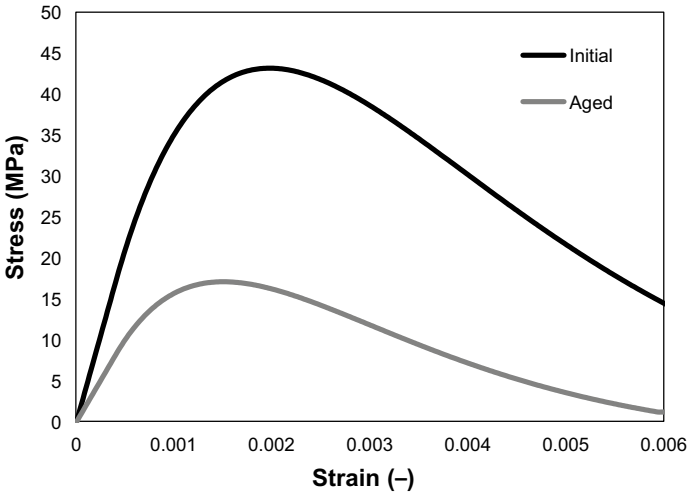

Figure 5-18. Modelled compression stress-strain curve of the concrete before and after leaching.

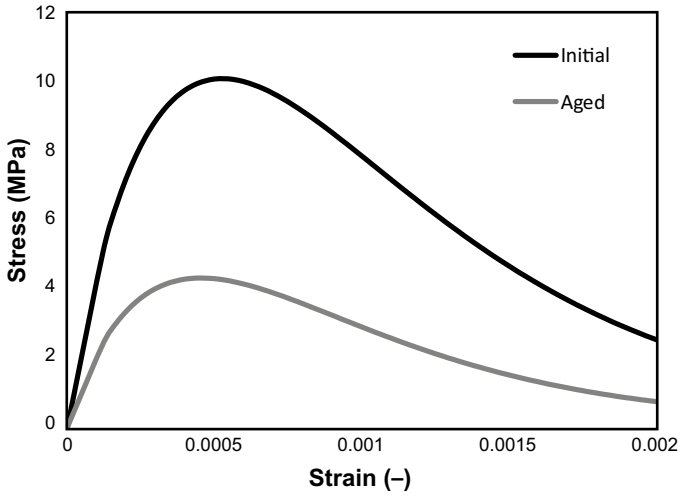

Figure 5-19. Modelled tensile stress-strain curve of the concrete before and after leaching.

5.3.3 Sulphate attack

The chemo-mechanical damage model coupled to the model of expansive reactions due to sulphate attack (see Sections 5.1 and 5.2) is verified in this section. The goal is not only to build confidence in the implementation of the models, but also to calibrate and adjust the value of the material parameter β (Equation 5-10). To this end, a laboratory experiment on a concrete sample is simulated with the HCM model. The experiments selected for the simulations have been carried out at the Swedish Cement and Concrete Research Institute (CBI) by Lagerblad (1999), using different types of cement. The main advantages of this experimental campaign compared to other published test results are the following:

- The tests were carried out using concrete specimens instead of mortar (as specified in the ASTM C 1012-89 standard).
- Two of the concrete mixes tested are very similar to the one used for constructions in the SFR repository, which is planned to be used in SFL. Cement compositions are given in Table 5-17. Water/cement ratios of 0.45 and 0.55 were used, similar to the concrete in SFR (0.47).
- The duration of the experiment is higher than four years, during which expansions were measured, much longer than the 6 months' duration of the ASTM C 1012-89 standard.

Some drawbacks may also be identified. Even though sulphuric acid was used to maintain the pH below 10, the solution was only renewed once a year. This could have implications on the boundary conditions used in the simulations (fixed concentration is used in the present model). Moreover, the uppermost part of the prisms was above the liquid surface to enhance sulphate ingress by capillarity. However, Lagerblad (1999) does not specify which part of the sample that was above the liquid surface. In addition, the samples were fully saturated right after curing. Drying will thus have a limited impact on the internal relative humidity of the sample over a period of 4 years. Therefore, the effect of capillarity is not expected to play a significant role with respect to sulphate ingress.

Concrete prisms of $300 \times 75 \times 75$ mm^3 were subjected to a 0.35 M sodium sulphate (Na_2SO_4) solution. The solution was renewed once a year and sulphuric acid was used to keep the pH below 10. Longitudinal expansions were periodically measured during a period of more than 4 years. Expansions were measured with a precision of around 0.05 mm.

Table 5-17. Chemical composition of cements: sulphate resistant (SR) Degerhamn Std cement used in the experiments (Lagerblad 1999), and Degerhamn Anläggningscement cement used in construction concrete in the SFR repository (Höglund 2001).

Component	Content % by weight	
	Lagerblad (1999)	Cement used in SFR
Ca	64.5	64
SiO_2	22.2	21
Al_2O_3	3.5	3.5
Fe_2O_3	4.7	4.6
MgO	1.0	0.7
K_2O	0.6	0.62
Na_2O	0.1	0.07
SO_3	2.0	2.2
Cl	N.S.	< 0.1
Free $CaCO_3$	0.8	0.9
Bogue composition (clinker)		
Tricalcium silicate, C_3S	51	64.4
Dicalcium silicate, C_2S	25	10.9
Tricalcium aluminate, C_3A	1.2	2.0
Tetracalcium aluminate ferrite, C_4AF	14	13.9
Calcium sulphate (gypsum), $C\hat{s}H_2$	N.S.	3.7
Alkali hydroxides, N + K	N.S.	0.7

N.S.: not specified.

The experiment corresponding to the concrete mix with sulphate resistant cement and a w/c ratio of 0.45 is simulated using the HCM model in 2D. Two symmetry planes are defined in the concrete prisms, so that only one quarter is explicitly discretized as shown in Figure 5-20. The sodium sulphate solution composition is given in Table 5-18.

Table 5-18. Sodium sulphate solution composition used in the simulation (same as in ASTM C 1012-89).

pH	7
Temperature (°C)	25
Species (totals)	**Concentration (M)**
Na	0.70
S(6)	0.35

The geometry is discretized with a mapped mesh of quadrilateral finite elements. Quadratic elements are used for the mechanical problem, while linear elements are used for reactive transport. The mesh is refined next to the external boundaries, where ettringite precipitation is expected (Figure 5-20). The total number of elements is 1 000 with a maximum element size of 3 mm and minimum of 0.66 mm on the top right corner.

A simulation time of 5 years is considered, with a constant temporal discretization for the operator splitting approach of 0.05 years per time step. This discretization satisfies the Von Neumann stability criterion that depends on the diffusion coefficient and the temporal and spatial discretization. The maximum time step following this criterion is shown in Figure 5-21.

For the reactive transport study, no flux is prescribed in the bottom and left boundaries, while on the top and right boundaries a constant sulphate solution concentration is set (Figure 5-20). For the mechanical analysis, symmetry is applied on the left and bottom boundaries while the other two boundaries are free to deform.

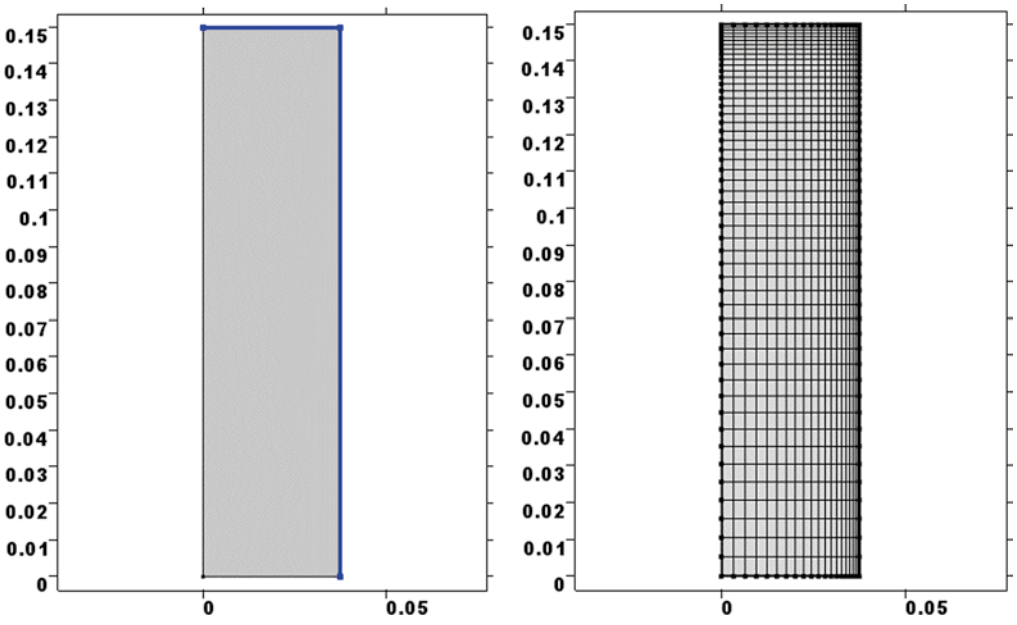

Figure 5-20. *(Left) Geometry and boundary conditions for the modelling of sulphate attack in concrete prisms. Only one quarter is discretized. Blue boundaries correspond to fixed concentration boundary conditions, while black boundaries are closed to diffusion. For the mechanical setup, the left and bottom boundaries are symmetry planes. (Right) Quadrilateral finite element mesh used in the simulations. Dimensions are in meters.*

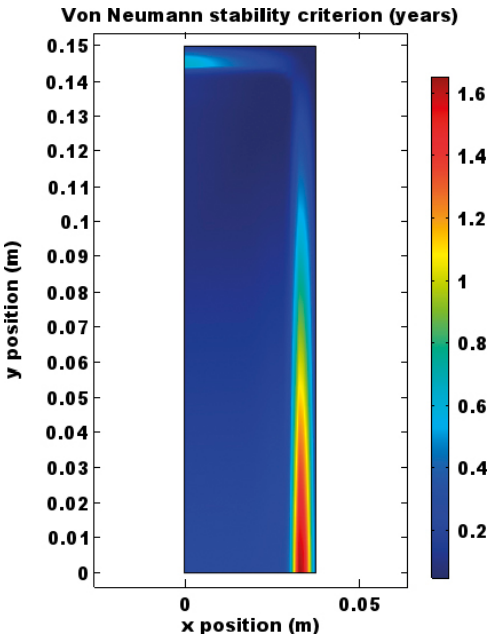

Figure 5-21. *Maximum time steps based on Von Neumann stability criterion (time scale in years).*

The main mechanical properties of concrete and the damage model parameters implemented are shown in Table 5-19. Given the similarity of the concrete mix between these experiments and the SFR construction concrete (Table 5-17), the concrete composition used in the simulations is the same as described in Table 5-6. The parameter β of the model of expansions due to sulphate attack is fitted to experimental data so that similar longitudinal expansions are obtained. The model for expansions is typically very sensitive to this parameter. This has also been observed using the present model. The results based on the longitudinal expansion of the prism conclude that a well calibrated value for β would be 0.36. This value is within the range used to fit other experiments in the literature (see Section 3.2.2).

Table 5-19. Mechanical properties and damage model parameters used in the simulation of the experiments by Lagerblad (1999).

Material properties	Value
Undamaged Young's modulus (GPa)	42.64
Undamaged Poisson's ratio (–)	0.22
Initial porosity (–)	0.11
Initial diffusion coefficient (m^2/s)	1.84×10^{-12}
Mazars' damage model parameters	
ε_0	0.8×10^{-4}
A_t	0.95
B_t	4 200
A_c	1.09
B_c	1 032.1

Figure 5-22 shows the predicted ettringite precipitation after 5 years of sulphate attack. A penetration depth of 3–4 mm from the exposed surfaces may be observed, where ettringite concentration reaches a plateau (0.13 mol/litre$_{medium}$ or 0.092 volume fraction). No secondary ettringite forms within the rest of the sample, where its concentration remains similar to the initial one (approx. 0.01 volume fraction). Figure 5-22 shows the volumetric strain developing due to ettringite precipitation. The volumetric strain starts to decrease near the exposed surface due to the increase in φ^* (defined in Equation 5-12) resulting from dissolution of the main hydrates (portlandite, C-S-H, etc.).

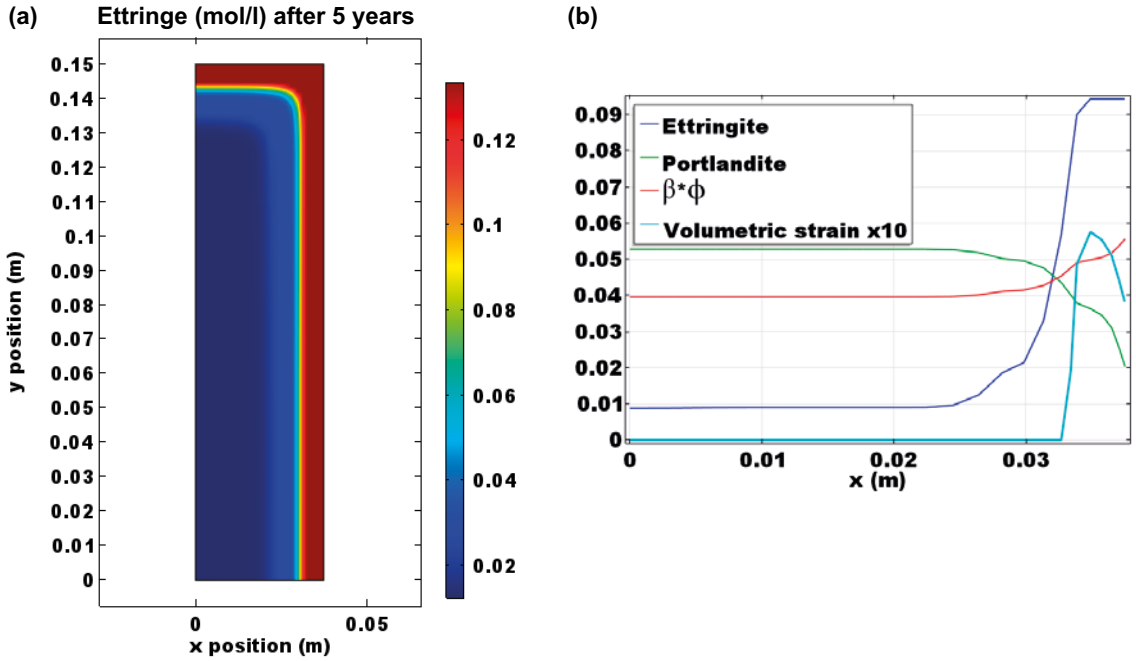

Figure 5-22. *(a) Ettringite precipitation after 1 800 days (precipitation scale in moles/litre of medium). (b) 1D profile at mid height of the domain after 1 800 days showing: ettringite and portlandite volume fractions (–), the term β·φ*, and the volumetric expansion due to ettringite formation (x10 magnification) given in Equation (5-10).*

The results in terms of longitudinal expansions at different times are presented in Figure 5-23. It may be observed that the sensitivity of the model results to variations of the β parameter is relatively high. Comparing simulation and experimental results, in terms of expansions after 1 800 days, yields an adequate match with β equal to 0.36. This comparison is made against the experimental result resulting from the average expansion measured in samples with 0.45 and 0.55 water/cement ratios. The experimental expansion after 1 736 days is 0.301 ‰ while the model yields a value of 0.305 ‰. Therefore, in the simulations presented in Section 7, a value of 0.36 for the β parameter is used.

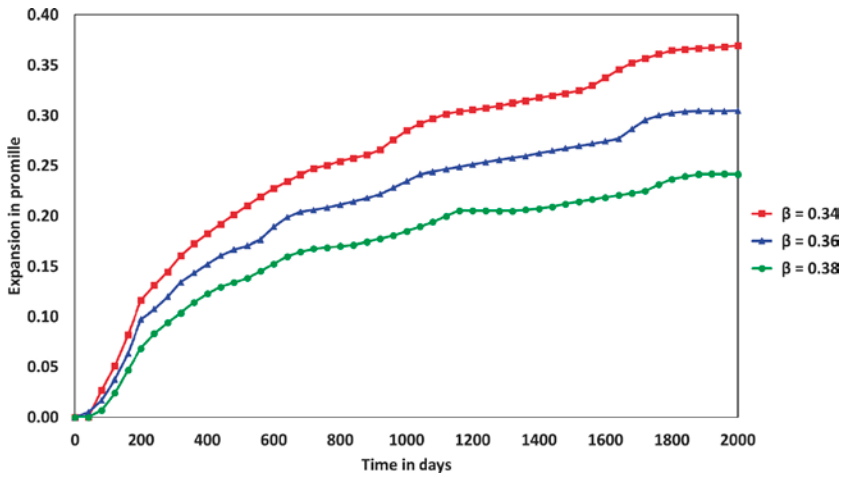

Figure 5-23. *Prisms expansion after 1 800 days with different values of β parameter.*

6 HCM modelling of calcium leaching in the BHK vault

6.1 Description of conceptual model

The groundwater flow and reactive transport models used in the present HCM model for calcium leaching correspond to the Base Case (Case I) in Idiart and Shafei (2019). The 2D geometry corresponds to a cross-section of the BHK concrete vault of the SFL repository. It consists of three domains: the host rock, the concrete backfill, and a waste domain (Figure 6-1). The only difference with the model of Idiart and Shafei (2019) is that the corners of the concrete backfill and waste are rounded to prevent the build-up of stress singularities at these points. The rock domain for the groundwater flow part of the model is identical to Case I in Idiart and Shafei (2019). For the mechanical analysis, a larger rock domain is used to study the impact of in-situ stresses on the BHK vault behaviour. The rock domain is 150×150 m^2, so that the four boundaries of the model are located at approximately 3 times the size of the BHK vault (65 m). The volume of the backfill has been conceptualized as a monolith made of the concrete used in the SFR repository (Höglund 2014). In turn, the radioactive waste domain is simplified as a continuous and homogeneous cementitious material. The only chemically reactive material considered in is concrete.

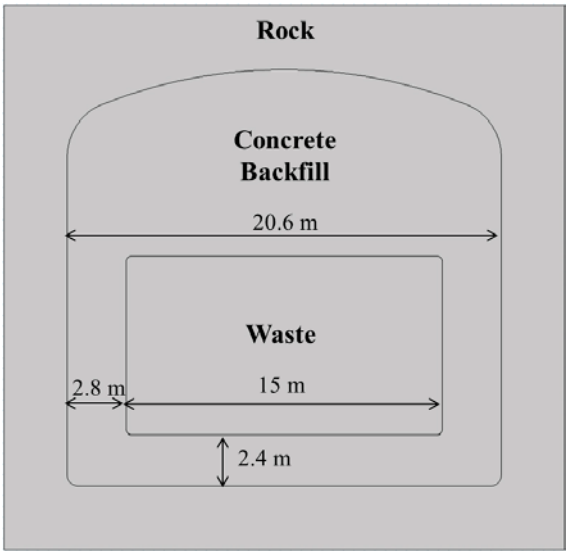

Figure 6-1. *2D cross-section of BHK vault and dimension in metres (m), including three domains: host rock, concrete backfill and waste.*

The chemical analysis is based on the use of the thermodynamic database CEMDATA07 (e.g. Lothenbach et al. 2008). All chemical reactions have been calculated assuming thermodynamic equilibrium. The initial chemical composition of concrete corresponds to the full chemical setup in Idiart and Shafei (2019). The groundwater composition, which is the boundary condition of the reactive transport model, is given in Table 6-1. The initial porewater composition of concrete in the backfill and waste domains is also specified in Table 6-1. The mineralogical phase assemblages and exchanger compositions to represent alkali uptake of the concrete and waste domains are presented in Table 6-2. A full set of minerals that are allowed to dissolve and precipitate in the concrete and waste domains is given in Appendix C.

The groundwater flow considers a constant inlet flow along the left boundary, in order to generate a horizontal flow, and no flow boundary conditions on the top and bottom boundaries.

Material properties for flow and transport of each domain are presented in Table 6-3. Porosity changes due to mineral dissolution/precipitation are considered explicitly, as well as their impact on the hydraulic conductivity and diffusion coefficient (Table 6-3).

Table 6-1. Groundwater composition corresponding to the old meteoric end member (see Pękala et al. 2015) and concrete porewater composition in equilibrium with the mineral phases considered in the full chemistry simulations used for backfill and waste domains.

Porewater compositions	Concrete	Groundwater
pH	12.97	8.64
Temperature (°C)	25	25
Ionic strength (mol/kg water)	0.128	
Species (totals, mol/kg water)		
Al	5.542×10^{-7}	1.210×10^{-6}
C	1.001×10^{-5}	6.910×10^{-4}
Ca	3.684×10^{-3}	5.260×10^{-4}
Cl	5.550×10^{-5}	4.535×10^{-3}
K	8.837×10^{-2}	7.600×10^{-5}
Mg	2.526×10^{-8}	1.480×10^{-4}
Na	2.698×10^{-2}	4.790×10^{-3}
S(6)	3.289×10^{-3}	3.730×10^{-4}
Si	4.522×10^{-5}	1.420×10^{-4}

Table 6-2. Mineral assemblage of concrete and waste domains in the full chemistry simulations. The chemical composition of the minerals and their equilibrium constants are presented in Appendix C.

	Concrete			Waste		
Primary mineral	Concentration (mol/litre$_{medium}$)	Concentration (mol/kg$_{water}$)	Volume fraction (–)	Concentration (mol/litre$_{medium}$)	Concentration (mol/kg$_{water}$)	Volume fraction (–)
CH (portlandite)	1.602	14.56	0.053	0.836	2.787	0.053
CSH_{jen}	1.209	10.99	0.094	0.631	2.104	0.094
Ettringite	0.012	0.111	0.009	0.006	0.021	0.009
Hydrogarnet Si	0.104	0.95	0.015	0.054	0.182	0.015
Thaumasite	0.035	0.318	0.012	0.018	0.061	0.012
Hydrotalcite OH	0.017	0.154	0.004	0.009	0.029	0.004
Porosity	-	-	0.110	-	-	0.300
Inert fraction	-	-	0.704	-	-	0.603
Total	-	-	1.000	-	-	1.000
Exchanger composition	(mol/litre$_{medium}$)	(mol/kg$_{water}$)		(mol/litre$_{medium}$)	(mol/kg$_{water}$)	
CaX_2	0.00037	0.0034		0.00059	0.0020	
KX	0.05354	0.4867		0.07617	0.2539	
NaX	0.00791	0.0719		0.01124	0.0375	

Table 6-3. Physical properties of concrete backfill and waste domains (Idiart and Shafei 2019). Relations between porosity and physical properties are considered similarly to Idiart and Shafei (2019). The value of tortuosity for the waste is valid as long as the effective diffusion coefficient is equal or lower than the diffusion in free solution, which is the case in all simulated cases (a porosity value of 0.458 for the waste would need to be attained).

Domain	Porosity, φ_0	Tortuosity, τ	D_e (m²/s)**	K_0 (m/s)**
Concrete backfill	0.11	0.0318	3.50×10^{-12}	8.30×10^{-10}
Waste	0.3	1.1600	3.50×10^{-10}	1.00×10^{-7}
Rock*	-	-	-	5.00×10^{-9}

** Hydraulic conductivity of the rock is set to obtain groundwater flow velocities in the BHK vault as close as possible to the average value from Abarca et al. (2016).*

** $D_e = \left(\frac{\varphi}{\varphi_0}\right)^{2.5} \tau \varphi_0 D_0$ *with* $D_0 = 1 \times 10^{-9}$ *m²/s and* $K(\varphi) = K(\varphi_0) \frac{(1-\varphi_0)^2}{\varphi_0^3} \frac{\varphi^3}{(1-\varphi)^2}$

The mechanical model is solved using iCP, after the reactive transport simulation. This implies that feedback between mechanical damage and transport properties is not taken into account. This is a valid assumption for the cases where mechanical damage is not significant, as will be showed to be the case for calcium leaching. On the other hand, the impact of chemical damage on transport properties is already considered in the reactive transport simulations via the coupling of these properties with porosity changes.

The mechanical model considers the rock and waste domains as linear elastic media. For the concrete backfill, the HCM model considers mechanical and chemical damage. To this end, the Mazars' mechanical damage model (Section 5.1) is coupled to the multi-scale homogenization model (Section 5.2). The parameters used in the different domains for these models are given in Table 6-4.

The parameters of the concrete backfill are based on the following reference mechanical properties provided by SKB:

- Compressive strength: ~50–60 MPa
- Tensile strength: ~4–6 MPa
- Young's modulus: ~40 GPa
- Poisson's ratio: ~0.2

For the rock mass, the selected values are thought to be representative of Laxemar conditions. A list of values from different studies in Laxemar and Forsmark is given in Table 6-5. A representative value of the Young's modulus for the waste is uncertain. Therefore, a sensitivity analysis is performed to assess the effect of this parameter on the results. The reason to assume a low value (1 GPa) for the Base Case is to consider that the waste does not have a significant load bearing capacity.

Table 6-4. Mechanical properties of the rock, concrete and waste domains used in the mechanical model.

Parameter	Rock	Concrete	Waste
Young's modulus, E (GPa)	70*	42.6	1*
Poisson's ratio, v (–)	0.3	0.22	0.22
Density, ρ (kg/m³)	2700	2400	2560
ε_0	-	0.8×10^{-4}	-
A_t	-	0.95	-
B_t	-	4200	-
A_c	-	1.09	-
B_c	-	1032.1	-

** Values used in the Base Case. Sensitivity analyses are presented in Sections 6.3.2.4 and 6.3.2.5.*

Table 6-5. Mechanical properties of the intact rock reported for Forsmark and Laxemar sites.

Reference	Site	E (GPa)	v (–)
SKB (2009)	Laxemar	60–97	0.26–0.33
SKB (2009)	Laxemar	50–59*	0.3
SKB (2008)**	Forsmark	57–81	0.24–0.27
Fälth and Gatter (2009)	Forsmark	70	0.25
Malm (2012)	Forsmark	70–80 (25)	0.23–0.30
Mas Ivars et al. (2014)	Forsmark	60	0.23
Carlsson et al. (2014)	Forsmark	66–89	0.23–0.35

** Deformation modulus of fractured rock mass; ** Data from FFM06 (Table 7-6 of SKB 2008).*

The active loads considered in the model are the following:

- In-situ stresses of the rock: a perfect contact condition (continuity of the displacement field) between the rock and the concrete backfill is considered
- Self-weight of concrete backfill and waste domain.

The reason to account for a perfect contact between the rock and the concrete backfill is due to the fact that cavern convergence will eventually lead to a similar situation. Moreover, this assumption is conservative in the sense that it is the most unfavourable case for the concrete structure.

Mechanical effects of water pressure are not considered in the model. The reason is that in the long-term pressure gradients will vanish and the concrete structure will be in hydraulic equilibrium with the surrounding rock. Moreover, the Biot's coefficient for concrete is typically below 0.5, reducing the coupling between pore pressure and stress state (see Section 3.1.2). The system is considered fully water saturated and thus no drying shrinkage effects need to be considered.

On the other hand, time-dependent deformations due to constant stresses in the concrete structure (creep) could have a non-negligible impact. However, at this stage, a creep model is not included in the simulations. Creep is also not considered in host rock (fractured granite), although there are indications that long-term convergence of walls of excavated caverns could be non-negligible (e.g. Malan 2012). As stated by Fälth and Gatter (2009), time dependent rock displacements are regularly monitored in the SFR repository at Forsmark. The measured average displacements around the Silo have been of the order of 0.2 mm during the first 20 years of operation.

6.2 Numerical model setup

The conceptual model is implemented using iCP (Nardi et al. 2014). This section presents the details of the numerical implementation.

6.2.1 Finite element meshes

The computational domain has been discretized using triangular elements, as shown in Figure 6-2 and Figure 6-3. Linear elements are used for groundwater flow and solute transport, while the mechanical analysis uses quadratic elements. For flow and reactive transport, the maximum element size is 0.6 m. The total number of elements is 6 180 for flow and 3 782 for reactive transport. For the mechanical analysis, the maximum element size is 10.1 m in the rock and 0.3 m in the vault, with a total number of elements of 21 988, of which 18 014 correspond to the vault.

6.2.2 Temporal discretization

The simulation time is 100 000 years. The temporal discretization used for the iCP communication steps between Comsol and Phreeqc is the same as in Idiart and Shafei (2019), and increases stepwise from time steps of 2 years to 9 years. These time steps were chosen to satisfy the Courant and von Neumann stability criteria. The mechanical analysis is quasi-static, as it does not include time-dependent deformations (creep). Still, deformations due to chemically-induced damage are calculated as a function of time.

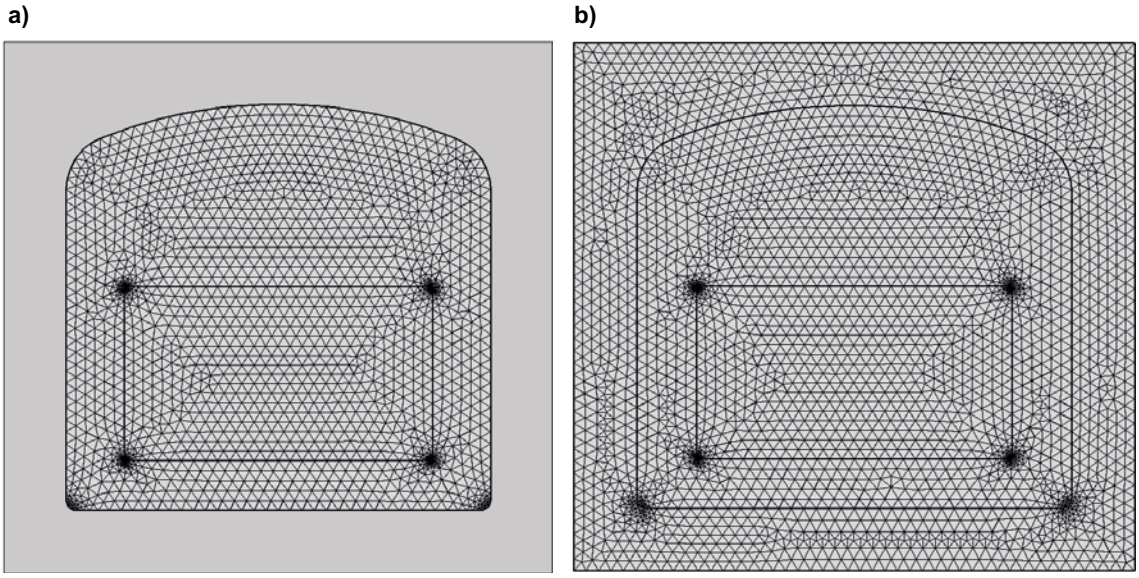

Figure 6-2. *Finite element meshes used for (a) reactive transport and (b) groundwater flow.*

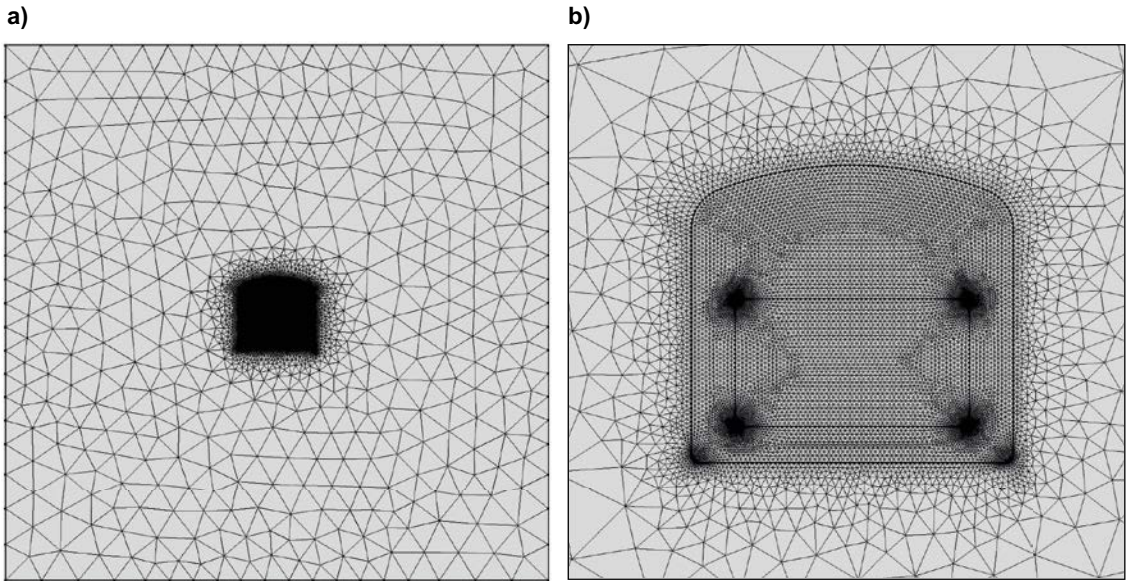

Figure 6-3. *(a) Full finite element mesh used for the mechanical model (size of the domain is 150 x 150 m^2) and (b) zoom around the vault.*

6.2.3 Initial and boundary conditions

6.2.3.1 Groundwater flow

Boundary conditions to simulate groundwater flow correspond to a constant inlet flow along the left boundary of the rock domain (Figure 6-4). This is given by:

$$-n\rho.u = \rho U_0 \qquad (6\text{-}1)$$

In Equation (6-1), U_0 is the normal inflow velocity equal to 1.03×10^{-11} m/s, n is the normal vector to the boundary surface, ρ (kg/m^3) is the fluid density, and u (m/s) is the velocity at the boundary. The inflow velocity value corresponds to an average flow from the results obtained by Abarca et al. (2016). It corresponds to the case in which the SFL repository is located at 500 m depth. The hydraulic conductivity of the surrounding rock has been set to 6×10^{-10} m/s so that the flow in the concrete backfill is mainly given by the boundary condition. Thus, the hydraulic conductivity of the surrounding rock is not necessarily representative of the actual rock. The resulting Darcy velocity field in the 2D cross-section is shown in Figure 6-5.

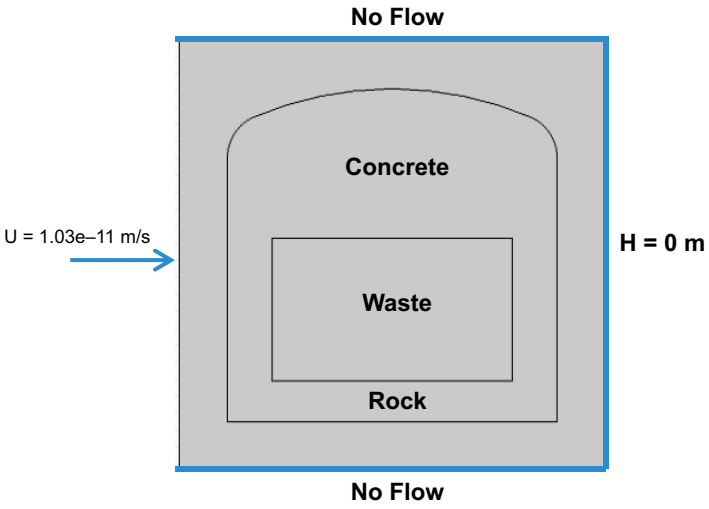

Figure 6-4. *Imposed fluid flow boundary conditions.*

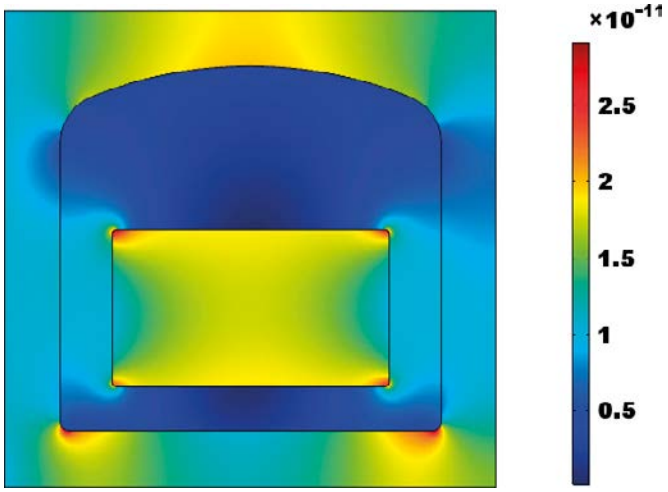

Figure 6-5. *Darcy velocity field (m/s) under constant inlet flow (left) and hydraulic head (right) boundary conditions.*

6.2.3.2 Solute transport

Reactive transport is only solved for in the concrete and waste domains. The rock domain is only used for calculating the groundwater flow field and in-situ stresses. Therefore, the boundary conditions for solute transport are imposed as a fixed concentration along the rock-concrete interface. The assumption of fixed concentration corresponds to a system where reactive transport processes in the repository are mainly driven by diffusion. Note that out-diffusion from the backfill does not affect the composition of groundwater.

6.2.3.3 Mechanical analysis

Depth-dependent in-situ stresses (Equation 4-1 through 4-3) are imposed as boundary loads on the rock contour (Figure 6-6). A roller boundary condition is applied on the lower boundary, while the lower left corner is fixed.

In-situ stresses have been previously estimated by Hakami et al. (2008), were a regional in-situ stress model specific for the Laxemar site was developed. In the Base Case, the repository is aligned with the major horizontal stress. However, two sensitivity cases consider a 15° clockwise and counter clockwise rotation of the BHK vault.

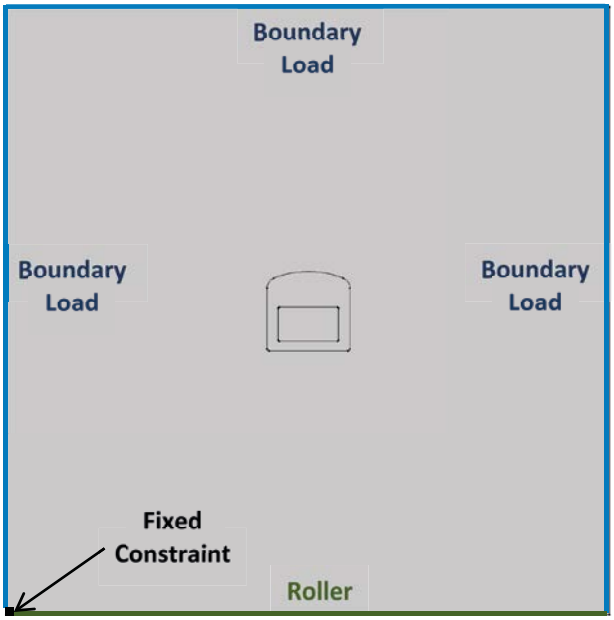

Figure 6-6. *Boundary conditions used for the mechanical analysis. The dimensions of the domain are 150 x 150 m².*

6.2.3.4 Couplings

All the simulations of calcium leaching presented here consider the coupling between dissolution/ precipitation of minerals due to chemical reactions and porosity. The impact of porosity changes on the effective diffusion coefficient and hydraulic conductivity are explicitly taken into account by Archie's law and Kozeny Carman equation, respectively. More details can be found in Idiart and Shafei (2019).

On the other hand, the impact of mechanical damage on the transport properties, as described in Section 3.3, is not considered in the simulations. Therefore, there is a one way coupling between the reactive transport models and the mechanical analysis. This means that reactive transport processes impact the mechanical analysis, provided that chemical damage is accumulated. At the same time, reactive transport processes are considered independent of the level of mechanically-induced damage. As shown in the next section, this is valid for most of the simulation cases presented.

6.3 Results

The results are illustrated as 2D distribution plots at given times and 1D profiles.

6.3.1 Base Case (Case I)

The Base Case of the present study consists of a 2D reactive transport simulation equivalent to the full chemistry simulations performed in Idiart and Shafei (2019). The mechanical analysis considers a repository depth of 500 m and a repository orientation aligned with the maximum horizontal stress.

The main results obtained from the reactive transport model are shown in Figure 6-7. After 100 000 years of calcium leaching, the portlandite dissolution front has advanced almost 1 m into the concrete backfill. C-S-H decalcifies (from CSHjen to CSHtob2) in a smaller region. The impact of dissolution of cement hydrates on porosity is also shown, leading to an increase of porosity at the concrete-rock interface from 0.11 to 0.24. The chemical damage calculated using the homogenization scheme of Section 5.2 increases to around 0.35 near the interface.

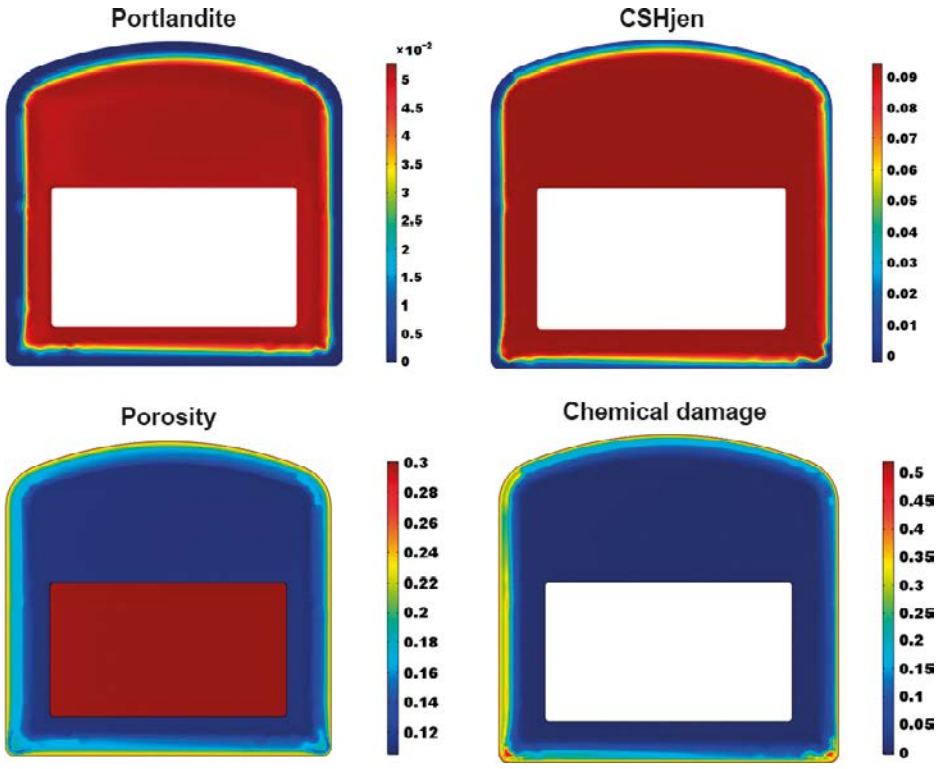

Figure 6-7. *Base Case reactive transport results after 100 000 years: 2D spatial distribution of portlandite and CSHjen volume fractions (top), and porosity and chemical damage (bottom).*

Figure 6-8 and Figure 6-9 show the initial and final Young's modulus and mechanical damage obtained with the HCM model, respectively. Initially, there is a small mechanical damage (up to 0.01, see Figure 6-9) at the corners of the waste domain. This is due to stress concentrations at the corners, even though rounded corners are considered. After 100 000 years, calcium leaching has an important effect on the Young's modulus of the concrete backfill at the interface with the surrounding rock. However, it may be observed that calcium leaching does not impact the structural behaviour of the backfill. This is reflected by the evolution of mechanical damage, which does not increase in the entire simulation time (Figure 6-9).

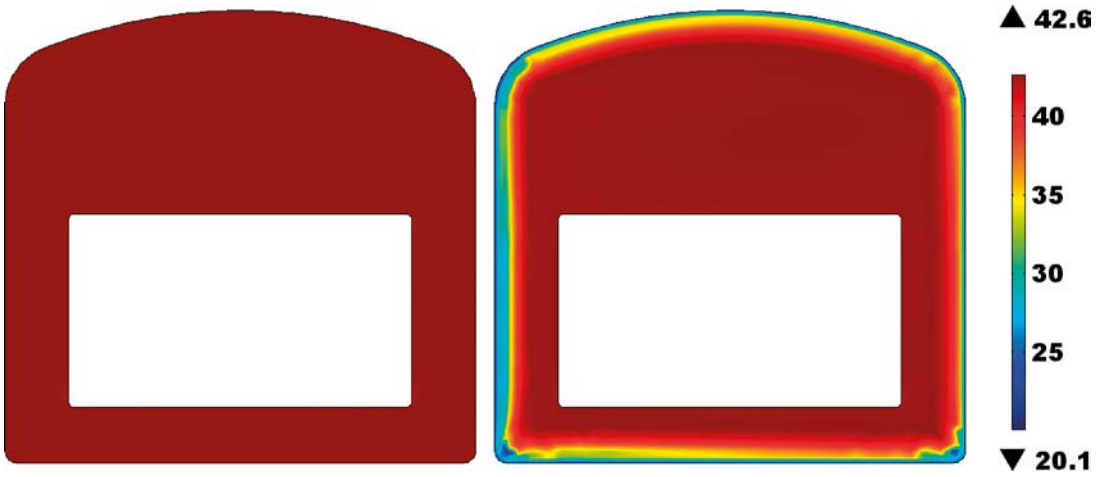

Figure 6-8. *Base Case results: 2D spatial distribution of the Young's modulus (GPa) of the concrete backfill at time zero (left) and after 100 000 years (right).*

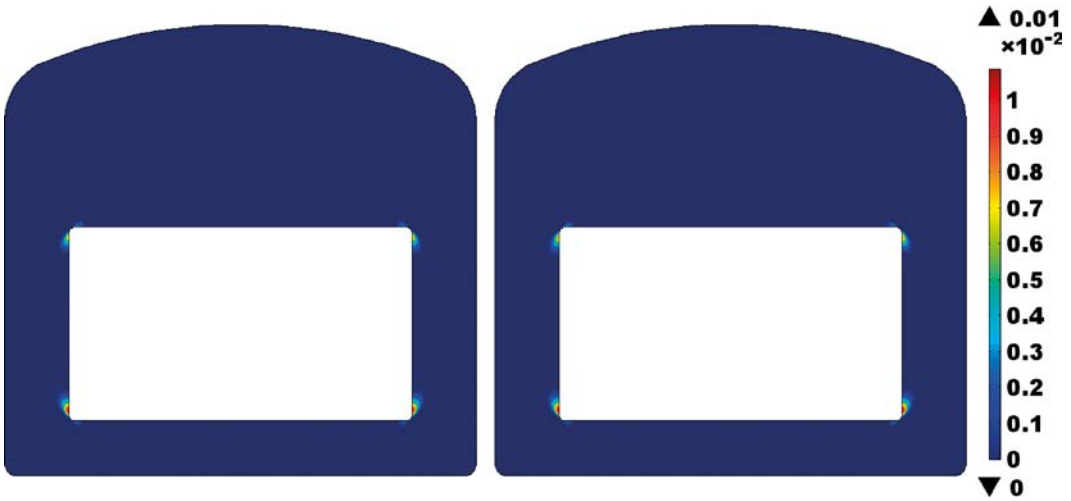

Figure 6-9. *Base Case results: 2D spatial distribution of the concrete mechanical damage initially (left) and after 100 000 years (right).*

The stress field in the BHK vault and the rock surrounding it is presented in Figure 6-10 and Figure 6-11 before and after 100 000 years of calcium leaching due to interaction with groundwater. As expected, very small changes are observed in the stress field. Horizontal and vertical stresses far from the repository in Figure 6-10 correspond to the in-situ stress at 500 m using Equations 4-2 and 4-3 (σ_h = 12.0 MPa and σ_v = 13.5 MPa). The horizontal and vertical stresses in the rock are higher than within the vault due to the difference in stiffness (the rock-concrete ratio is 70 GPa/42 GPa = 1.66). More details about the effect of rock stiffness can be found in Section 6.3.2.5. Within the vault, the waste domain has a very low stiffness (1 GPa, which translates to very small stresses in this domain). As a result, higher vertical stresses in the surrounding concrete backfill are observed at the sides of the waste domain. At the same time, the maximum compressive stresses in the backfill right above and below the waste are small (Figure 6-11).

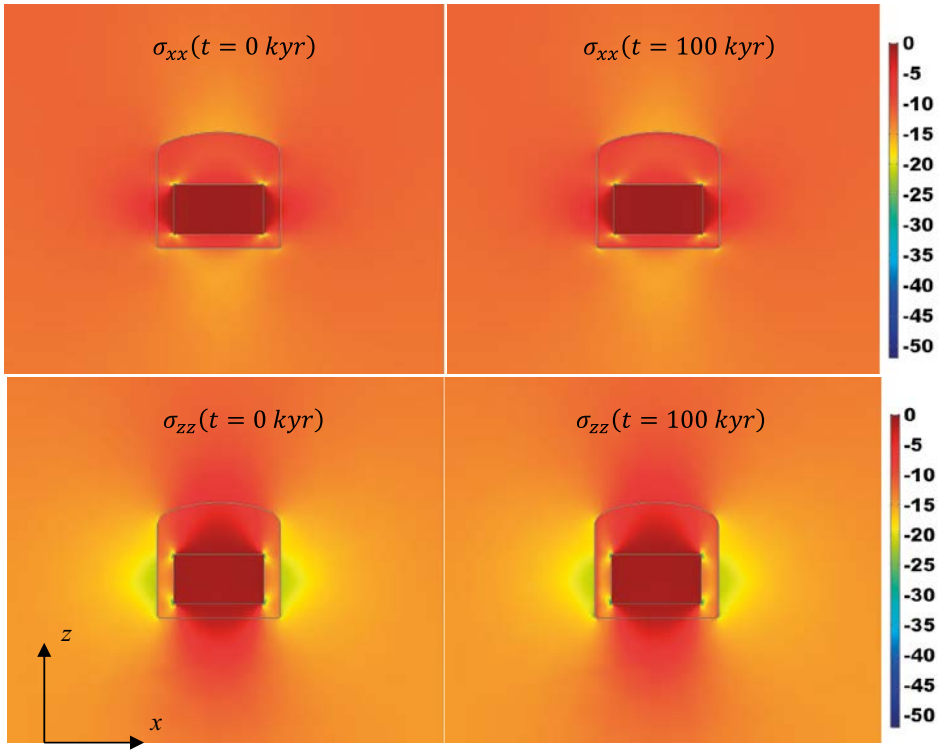

Figure 6-10. *Base Case results: 2D spatial distribution of the x (top) and z (bottom) components of the stress tensor (in MPa) initially (left) and after 100 000 years (right).*

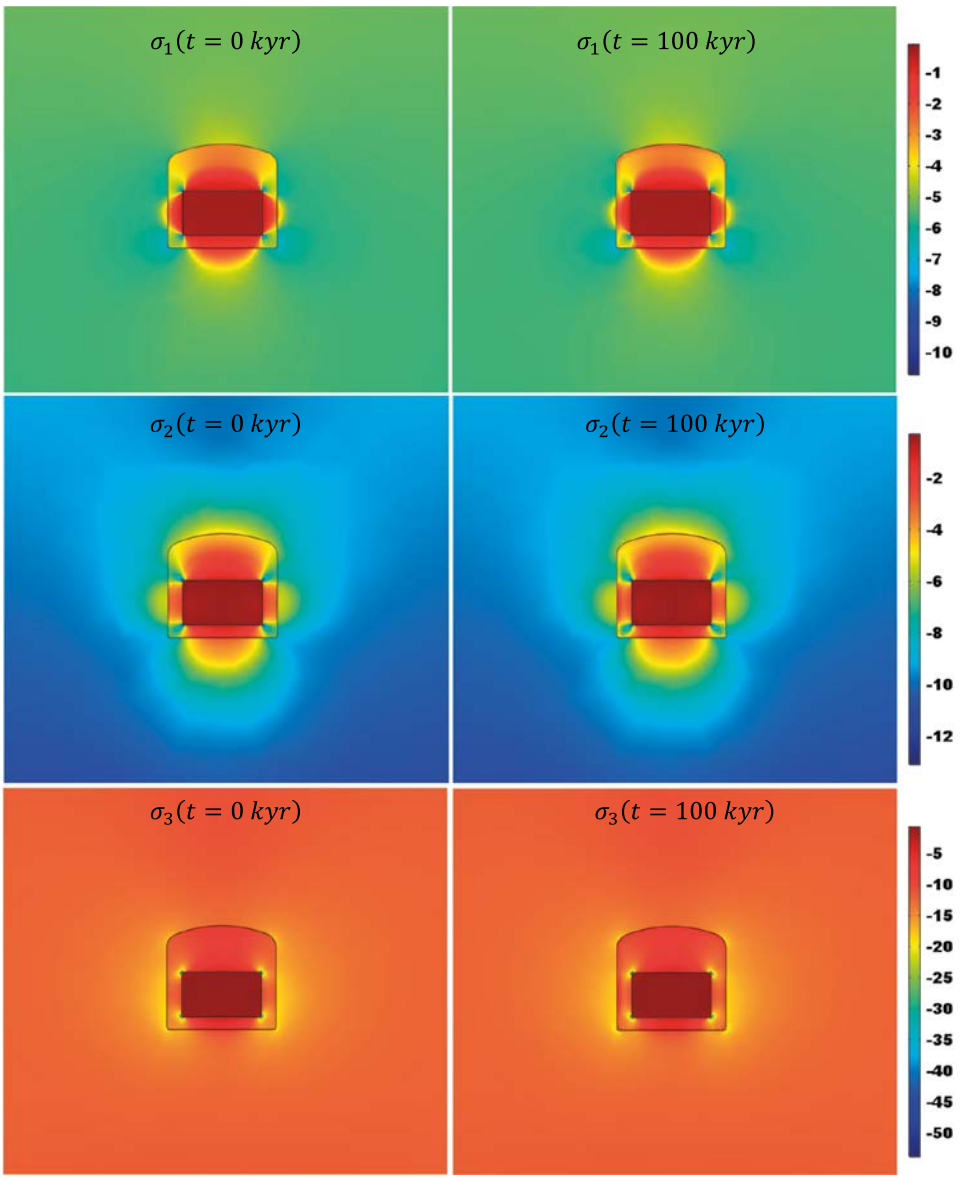

Figure 6-11. *Base Case results: 2D spatial distribution of the first (top), second (middle) and third (bottom) principal stresses (in MPa) initially (left) and after 100 000 years (right). The convention used is $\sigma_1 > \sigma_2 > \sigma_3$ with negative stresses indicating compression.*

After 100 000 years, there is a reduction of the vertical stresses in the concrete backfill near the rock (to the left and to the right) compared to the initial state (Figure 6-10). This is due to the effect of chemical damage, which leads to a concrete layer with an increased capacity to absorb deformations. This has been previously identified as a positive effect by Sellier et al. (2011).

The principal stresses in Figure 6-11 also show negligible changes of the stress field due to calcium leaching, except near the concrete-rock interface. The smallest compressive stresses (σ_1) fall within the waste domain. Interestingly, zones of the concrete backfill with small compressive stresses (> –2 MPa) around the waste domain can be identified. For an unreinforced concrete structure, it is important that tensile stresses are reduced. The maximum principal stress in compression (σ_3) shows values well below the uniaxial strength of concrete (50–60 MPa, Section 6.1).

The effect of calcium leaching on the stress field is more clearly visible in Figure 6-12, which presents vertical stresses across a 1D profile of the concrete backfill at the left of the waste domain. After 100 000 years, the compressive stresses in the chemically damaged zone decrease from 13–14 to 8–10 MPa. This leads to a stress redistribution, which partly translates into an increase in the vertical stress of the sound part of the concrete backfill. In addition, stresses are partly transferred to the rock (not shown).

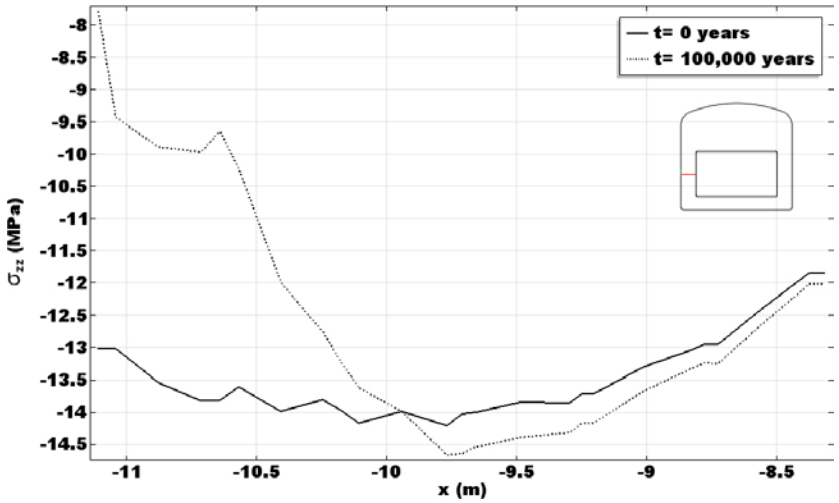

Figure 6-12. *Base Case results: 1D profiles of the initial and final stress on the vertical direction (σ_{zz}, MPa) in the concrete backfill at the left from the waste.*

6.3.2 Sensitivity cases

The sensitivity of the results to different loading conditions is explored in this section. The uncertainty in some of the assumptions of the model is investigated: repository depth, orientation of the vault axis, glaciation stresses, and elastic properties of the waste and rock.

6.3.2.1 Effect of depth of the repository

The depth of the SFL repository is yet to be determined. Therefore, the effect of increasing the depth from 500 to 700 m is explored. Given that in-situ stresses depend linearly on the depth (Equations 4-1 to 4-3), an increase of 200 m in depth will lead to vertical and minimum horizontal stresses of 18.9 and 16.4 MPa, respectively. This represents an increase of 40 % in the vertical stress and 37 % in the minimum horizontal stress.

The mechanical damage before and after 100 000 years of interaction with groundwater is shown in Figure 6-13. Compared to the Base Case (Figure 6-9), the extension of mechanical damage increases, but remains very small and limited to the concrete backfill at the sides of the waste domain. As in the Base Case, the effect of calcium leaching on mechanical damage is negligible and no differences can be observed between the initial and final states.

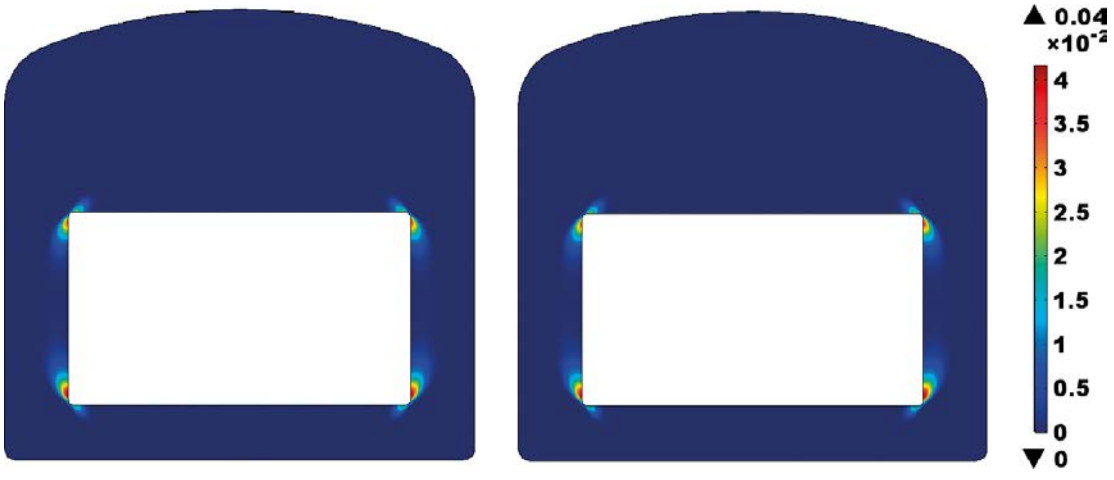

Figure 6-13. *Results corresponding to a repository depth of 700 m: 2D spatial distribution of the concrete mechanical damage initially (left) and after 100 000 years (right).*

Figure 6-14 and Figure 6-15 shows the distribution of stresses. Compared to the Base Case, an increase in vertical stresses is observed. Maximum compressive values (third principal stress) occur in the corners of the waste domain and rise in magnitude (from –64.1 to –80.3 MPa). First principal strains, shown in Figure 6-16, explain the increase in mechanical damage with the appearance of tensile strains in the concrete backfill at the sides of the waste domain.

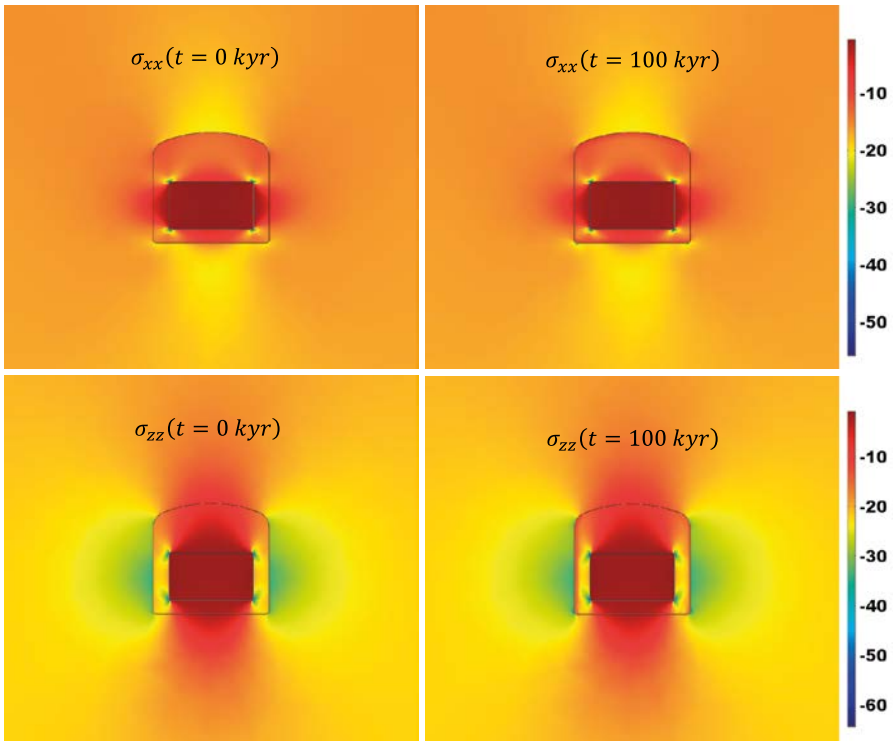

Figure 6-14. *Results corresponding to a repository depth of 700 m: 2D spatial distribution of the x (top) and z (bottom) components of the stress tensor (in MPa) initially (left) and after 100 000 years (right).*

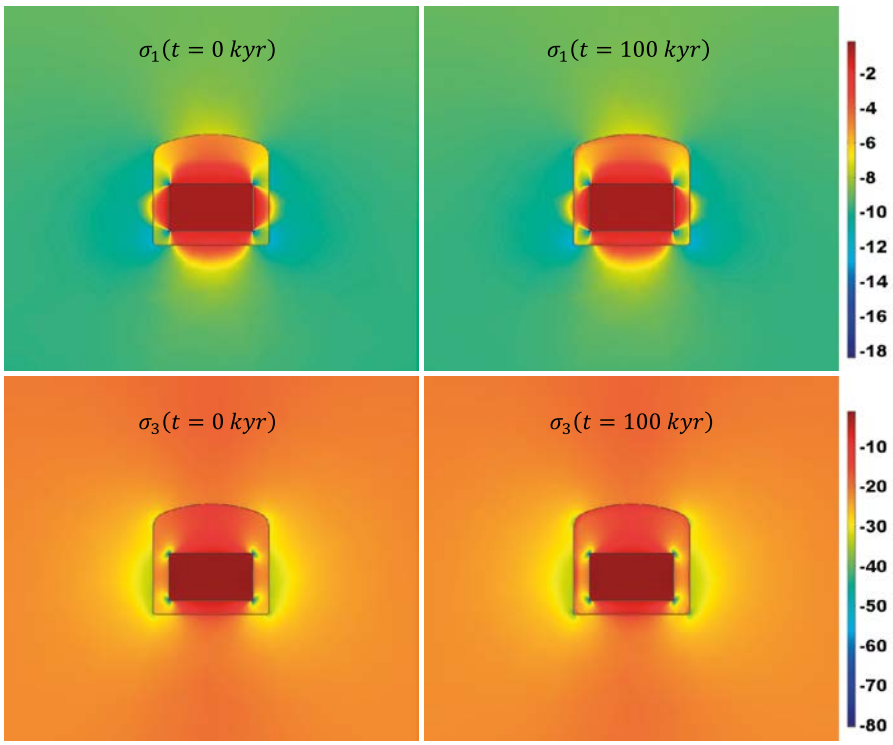

Figure 6-15. *Results corresponding to a repository depth of 700 m: 2D spatial distribution of the first (top) and third (bottom) principal stresses in MPa initially (left) and after 100 000 years (right).*

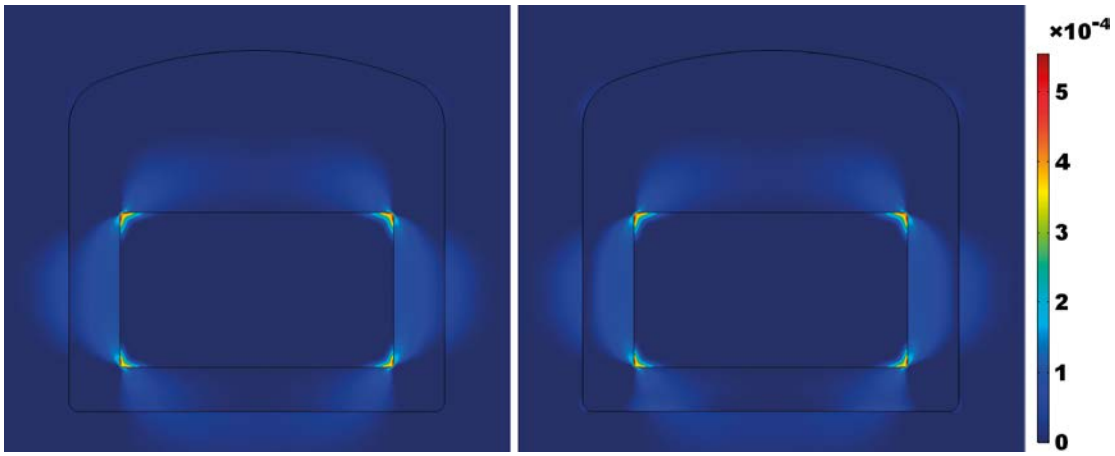

Figure 6-16. *Results corresponding to a repository depth of 700 m: 2D spatial distribution of the first principal strain (–) initially (left) and after 100 000 years (right).*

The vertical stress across a 1D profile of the concrete backfill at the left of the waste domain is presented in Figure 6-17. After 100 000 years, the compressive stresses in the chemically damaged zone decrease from ~19 to ~14 MPa. This reduction partly translates to an increase of vertical stresses in the sound part of the concrete backfill. In addition, stresses are partly transferred to the rock (not shown).

6.3.2.2 Effect of orientation of the repository

From a rock mechanics point of view, the repository orientation is defined in such a way that the maximum horizontal stress is parallel to the vault axis, so that the horizontal stresses perpendicular to the axis are minimized. However, there is an uncertainty in the determination of in-situ stresses and their direction (Section 4.1.2). The magnitude of the rotation considered in this sensitivity study is based on the uncertainty limits defined in Section 4.1.2. The simulations consider the effect of a 15° rotation of the BHK vault axis on the in-situ stresses acting on the structure. The horizontal stress perpendicular to the vault axis (σ_x) is calculated as:

$$\sigma_x = \sigma_h cos\ \alpha + \sigma_H\ sin\ \alpha \qquad (6\text{-}2)$$

where α is the rotation angle. The goal is to assess the mechanical damage associated with an increase in horizontal stresses or confinement level (Figure 4-5). The repository depth considered is 700 m. The results of the case with 0° rotation are presented in Section 6.3.2.1.

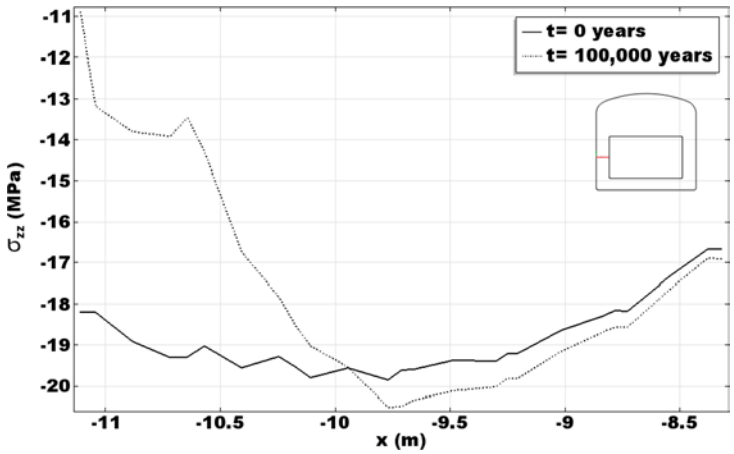

Figure 6-17. *Results corresponding to a repository depth of 700 m: 1D profiles of the initial and final σ_{zz} in the concrete left from the waste.*

The mechanical damage resulting from a 15° rotation can be found in Figure 6-18. An increase in horizontal stress with respect to the non-rotated case results from a 15° rotation. Higher horizontal stresses represent a higher level of confinement at constant vertical stresses, leading to a reduction of mechanical damage at the sides of the waste. However, damage at the corners of the waste domain increases slightly.

The stress state in the rotated case is analysed in the following figures. The effect of such a rotation on the increase of horizontal stresses is clearly seen in Figure 6-19 (top). Maximum compressive stresses in the concrete backfill are –88.4 MPa near the waste corners, instead –80.2 MPa when no rotation is considered (Figure 6-14). Although these values are higher than uniaxial compressive strength of concrete, they are lower than the compressive strength under triaxial compressive conditions. A 1D profile of the concrete backfill at the left of the waste domain is presented in Figure 6-21. After 100 000 years of calcium leaching, vertical stresses redistribute and concentrate on the middle section of the concrete backfill thickness.

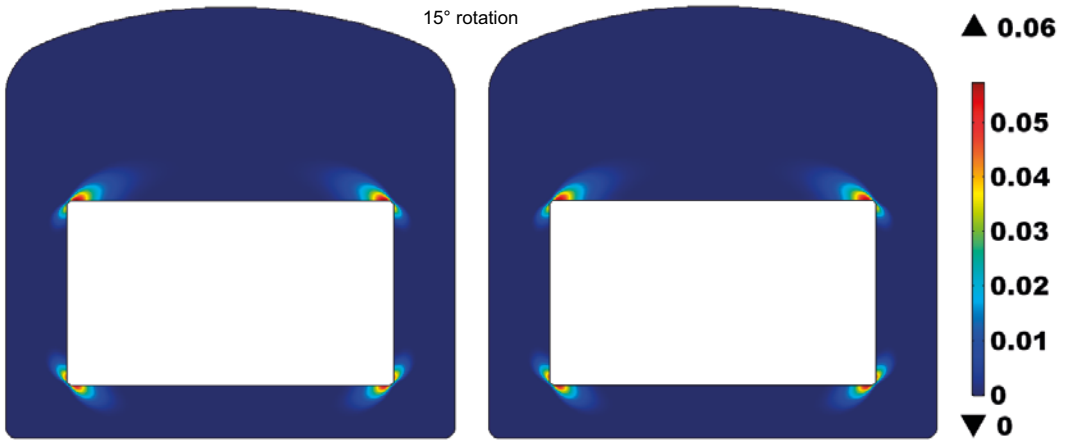

Figure 6-18. *Results for the rotated repository case: 2D spatial distribution of the concrete mechanical damage for 15° rotation initially (left) and after 100 000 years (right).*

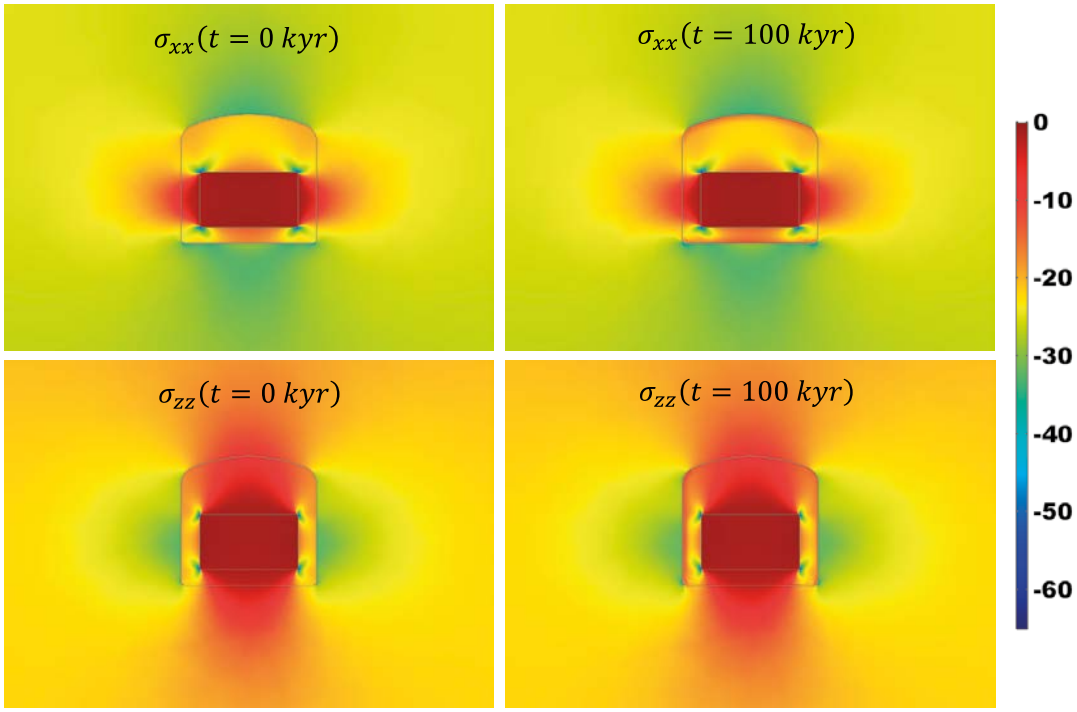

Figure 6-19. *Results for the case with 15° rotated vault axis: 2D spatial distribution of the x (top) and z (bottom) stress tensors in MPa initially (left) and after 100 000 years (right).*

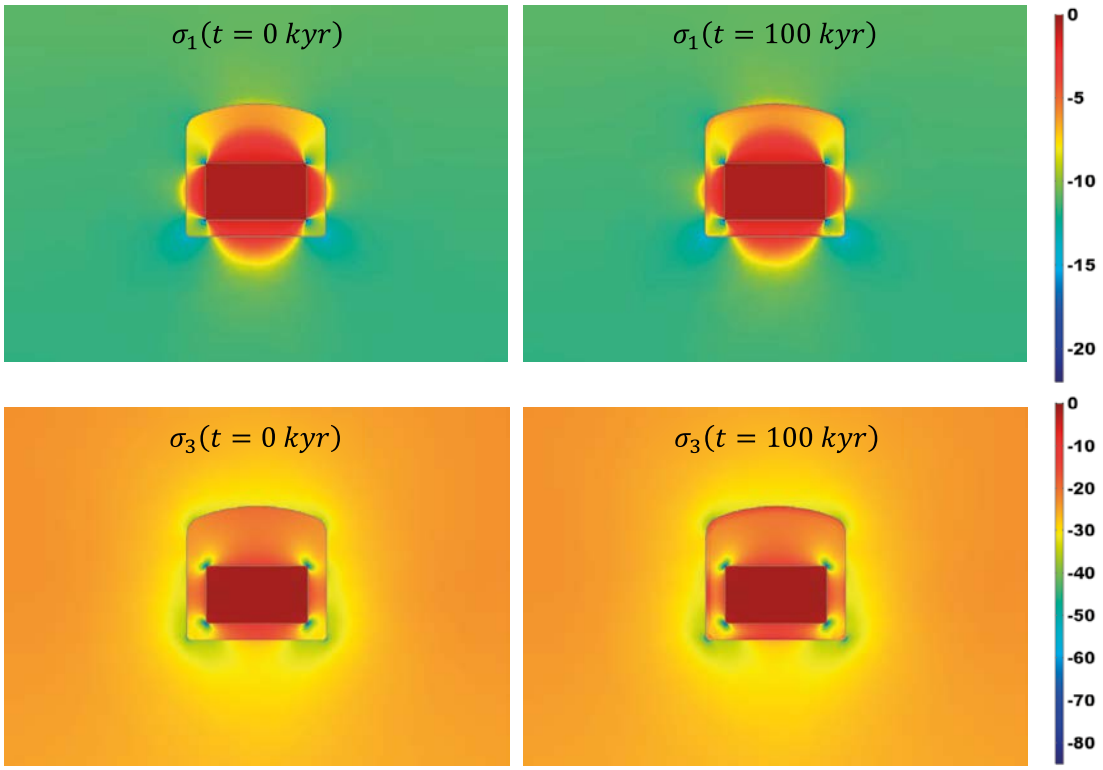

Figure 6-20. *Results for the case with 15° rotated vault axis: 2D spatial distribution of the first (top) and third (bottom) principal stresses in MPa initially (left) and after 100 000 years (right).*

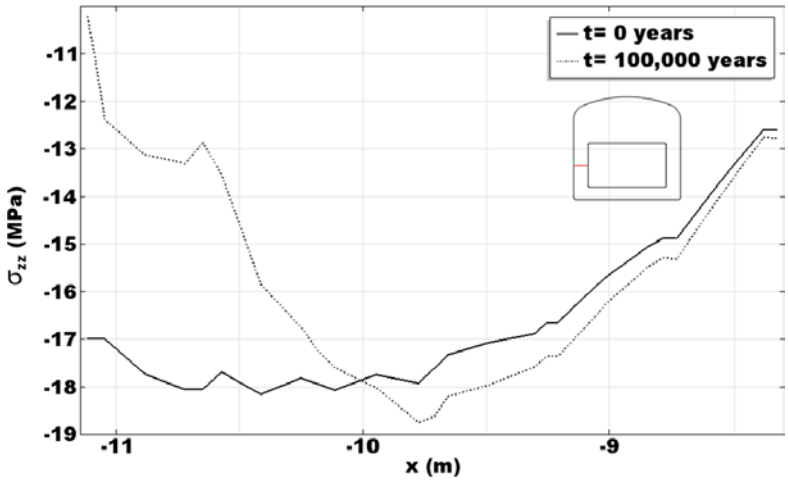

Figure 6-21. *Results for the rotated repository case: 1D profiles of the initial and final σ_{zz} in the concrete left from the waste.*

6.3.2.3 Effect of glaciation-induced stresses

As described in Section 4.1.3, the SFL repository will eventually be affected by a glaciation. In Lund et al. (2009), three-dimensional ice and earth models were used to calculate the response of the Earth to an ice load based on climate reconstructions of the Weichselian glaciation with constraints from geological observations.

In this work, the calculated glaciation-induced horizontal and vertical stresses from formation and melting of ice sheets obtained by Lund et al. (2009) are added to existing in-situ stresses (Equations 4-1 through 4-3). Their results in terms of induced stresses, presented in Figure 4-6, are imposed as boundary conditions to evaluate the potential mechanical damage in the BHK vault. As shown in Figure 4-6,

the effect of a glaciation is shown to have a larger impact on induced vertical stresses than on horizontal ones. In particular, the minimum induced horizontal stresses are the smallest during the stress peaks and even change their sign between the two peaks. This scenario will therefore lead to a reduction of the horizontal confinement level of the vault. It is assumed that the chemical degradation of concrete due to calcium leaching resulting from interaction with groundwater is identical to the Base Case.

Glaciation-induced stresses are added to the in-situ stresses in the model corresponding to a repository at 700 m depth, see Section 6.3.2.1. The reason not to assume a rotation is to minimize the horizontal stresses perpendicular to the vault axis. Given the relative values of the glaciation-induced stresses, this scenario is the most unfavourable for the stability of the vault barriers. The glaciation period was assumed to take place from 30 000 to 100 000 years in the simulation. Thus, the first stress peak from ice formation in Figure 4-6 occurs after 43 000 years, while the second peak takes place after 85 000 years. The results presented in the following correspond to this scenario. However, similar results are obtained if the calcium leaching evolution is decoupled from the glaciation period. Simulations of the effect of glaciation induced stresses without the effect of calcium leaching and with a leaching state corresponding to 100 000 years of interaction with groundwater lead to similar conclusions.

In Figure 6-22, the mechanical damage is presented for different times: initially, at the time of the first and second stress peaks, and after 100 000 years. The stress induced by the ice sheet causes additional damage all around the waste. The maximum value reaches 0.21 around the waste corners. After the first peak stress at 43 000 years, damage accumulates at appreciable levels, especially in the concrete backfill on both sides of the waste. This is due to the low load-bearing capacity of the waste domain resulting from the stiffness value assumed (1 GPa). After the second peak, damage increases from 0.12 to around 0.21.

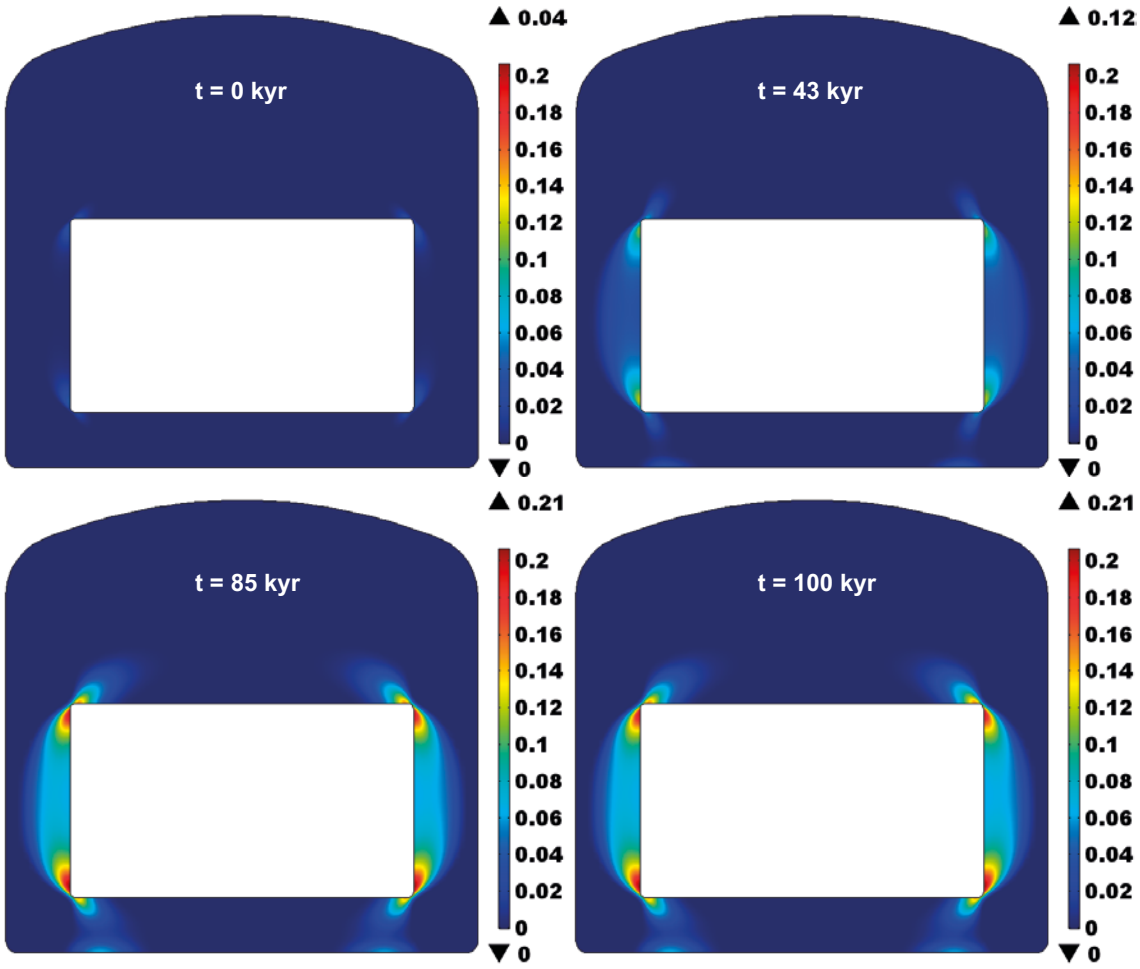

Figure 6-22. *Results for the simulation including glaciation induced stresses: 2D spatial distribution of the concrete mechanical damage at four different times.*

After 43 000 years, values of the first principal stress are almost positive, as shown in Figure 6-23. In turn, Figure 6-25 shows the distribution of compressive vertical stresses at the sides of the waste domain in a 1D profile at four different times. It may be observed how the two glaciation-induced peaks lead to much higher compressive stresses than the initial values. These high stresses (around 42 MPa) are close to the uniaxial compressive strength of the concrete considered in the simulations (50–60 MPa). The second glaciation stress peak is characterized by a significant increase in compressive stresses, as shown in Figure 6-24, with maximum values of –85 MPa at the concrete corners and the rock domain. At these regions, these high compressive stresses could lead to local instabilities and large creep deformations. However, a triaxial compression state is observed at these regions. As stated in Sections 5.1.1 and 5.3.1.2, triaxial stress states do not lead to damage with the present model (Pijaudier-Cabot and Mazars 2001).

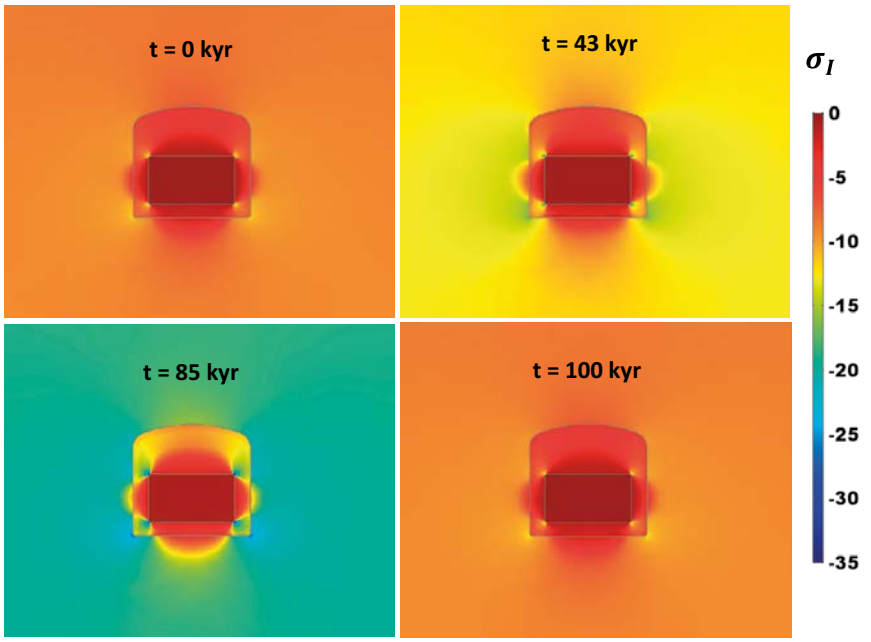

Figure 6-23. *Results for the simulation including glaciation-induced stresses: 2D spatial distribution of the first principal stress (in MPa) at four different times.*

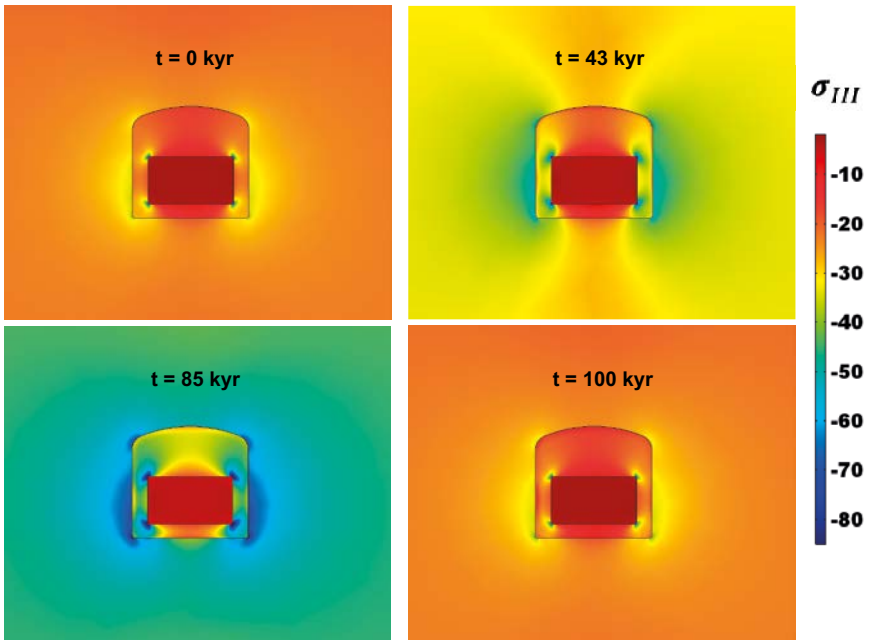

Figure 6-24. *Results for the simulation including glaciation-induced stresses: 2D spatial distribution of the third principal stress (in MPa) at four different times.*

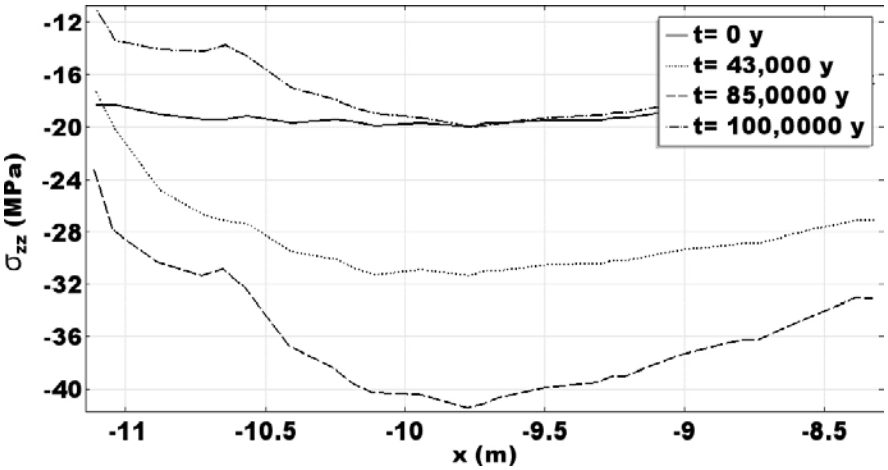

Figure 6-25. *Results for the simulation including glaciation induced stresses: 1D profiles of the σ_{zz} in the concrete left from the waste at four different times.*

6.3.2.4 Effect of the stiffness of the waste domain

In this section, the effect of the stiffness of the waste domain on the mechanical behaviour of the concrete backfill is investigated. The scenario selected is the Base Case, at a depth of 700 m (Section 6.3.2.1). The only modification introduced in the setup is the stiffness (Young's modulus) of the waste domain. A quasi-static analysis of stresses and strains on the BHK vault is considered, with chemical damage after 100 000 years of interaction with groundwater.

The stiffness of the waste domain, E_w, is defined as a linear function of the intact concrete Young's modulus, E_0, as:

$$E_w = k \cdot E_0 \tag{6-3}$$

where k is a proportionality coefficient. A parametric sweep of the relative stiffness k is performed, ranging from 0.001 to 5. Table 6-6 gathers all relative and absolute values of waste stiffness used in the sensitivity simulations. The highest stiffness equals 213 GPa (k = 5), a value that is close to that of steel. The lowest value (0.04 GPa) simulates a case in which the waste domain is extremely soft and the concrete backfill is almost free to deform at the interface. Another important intermediate value is k = 1, where concrete and waste domains have the same stiffness and for which the entire BHK vault cross-section acts as a concrete monolith.

Table 6-6. Relative and absolute values of the Young's modulus of the waste domain for the different studied cases. The relative values are referred to concrete undamaged Young's modulus, E0 = 42.6 GPa.

Case	Relative	Absolute (GPa)
1	5.00	213
2	1.50	64
3	1.00	42
4	0.75	32
5	0.50	21
6	0.25	11
7	0.10	4
8	0.023	1
9	0.001	0.04

Results of the sensitivity analysis are shown as 2D distribution plots with or without deformed configuration, 1D profiles, and time evolution of variables at selected points (see Figure 6-26).

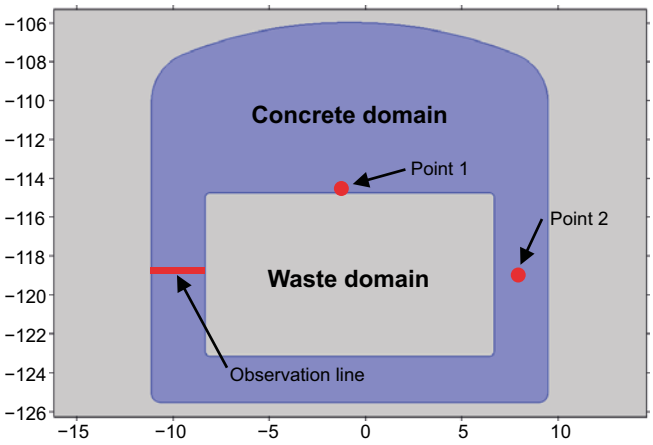

Figure 6-26. *Modelled backfill and waste domains. A 1D profile along the concrete backfill and 2 observation points in the concrete backfill are used for result presentation.*

Figure 6-27 shows the third principal stress (i.e. highest compression) magnitude and direction after 100 000 years for the largest and smallest k values. As expected, the most rigid domain attracts stresses, so that for $k = 5$ high stresses are observed in the waste domain. On the other hand, for $k = 0.001$, stress distributes through the concrete backfill, bypassing the waste domain.

When a high stiffness is assumed for the waste, or at least not lower than that of concrete, the entire vault deforms as a rigid solid (Figure 6-28, left). In that case, very small differences are found between the displacement of the different points of the concrete domain. For lower values of k, deformation increases and the concrete backfill at the sides of the waste start to bend (Figure 6-28, right).

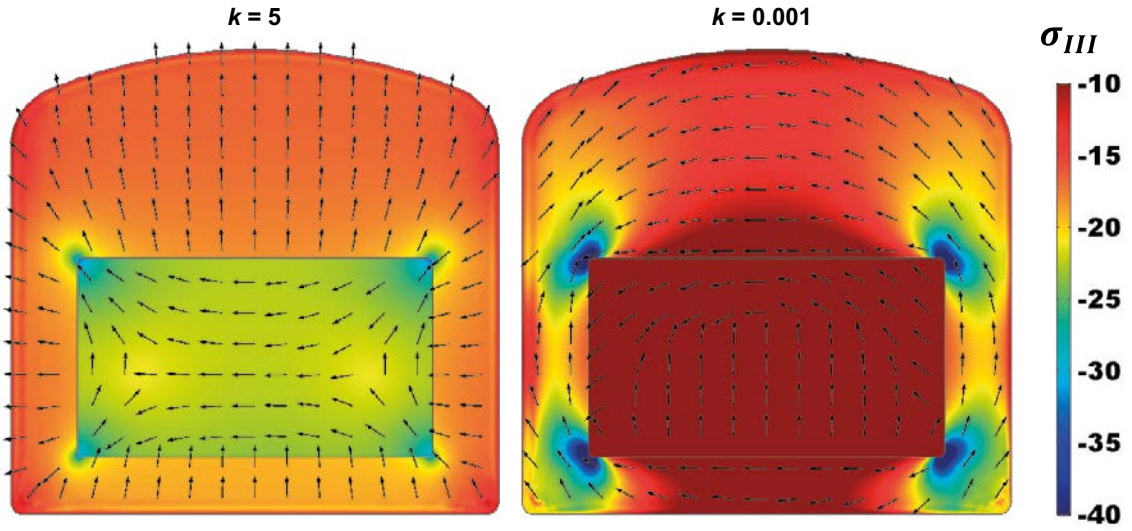

Figure 6-27. *2D spatial distribution of third principal stress magnitude (in MPa) and arrows representing the third principal stress direction, after 100 000 years. Comparison between highest (k = 5, left) and lowest (k = 0.001, right) stiffness of the waste domain.*

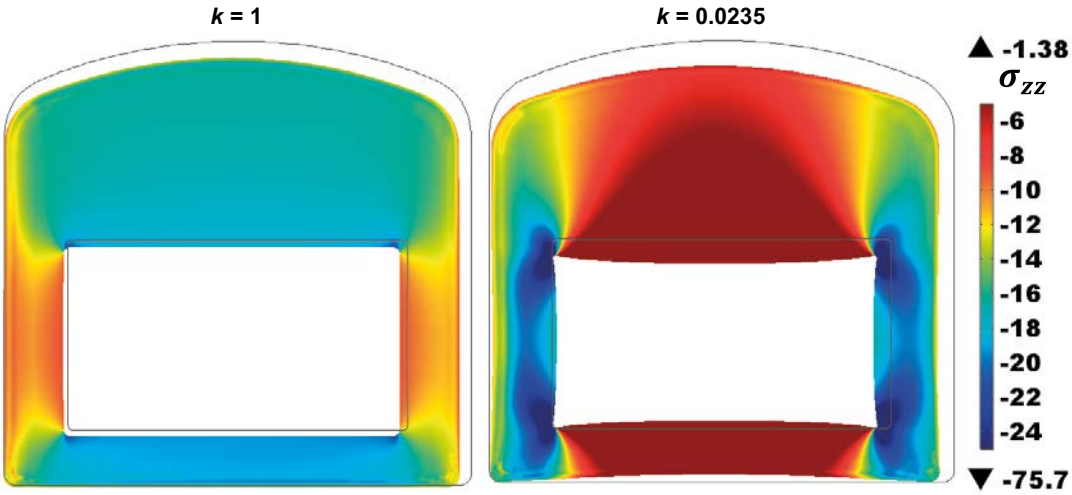

Figure 6-28. *2D spatial distribution of z component of stress tensor (in MPa) after 100 000 years in the deformed configuration (deformed magnification factor of 150). Comparison between different stiffness of the waste domain, k = 1 (42 GPa, left) and k = 0.0235 (1 GPa, right).*

The analysis of stress distribution through concrete backfill at the left of the waste domain is shown in Figure 6-29. As can be observed, a reduction of the stiffness of the waste leads to an increase of vertical stresses in the concrete backfill. The lower bearing capacity of the first 0.5 meters of the wall from the rock interface is explained by the chemical damage due to calcium leaching.

An important analysis when studying unreinforced concrete is the evaluation of the build-up of tensile stresses. This is assessed for the two points shown in Figure 6-26. The main conclusion extracted from this analysis is that tensile stresses appear for low stiffness values of the waste domain. Highest tensile stresses take place in the middle sections of the concrete backfill right above and below the waste (with a total thickness of 0.5 m). These values (up to 0.03 MPa) are still far from the uniaxial tensile strength of concrete (around 5 MPa). When using the lowest value of stiffness, representative of a scenario with no contact between concrete and waste domains, a significant area over the waste is bearing large tensile stresses (Figure 6-31).

Figure 6-30 illustrates the influence of the stiffness of the waste domain on the stress distribution in the concrete backfill. It shows how stresses (horizontal, vertical, and third principal stresses) change when varying the waste domain Young's modulus.

Finally, mechanical damage increases when the waste stiffness is reduced, as shown for example in Figure 6-32 for $k = 0.001$. In conclusion, the effect of low stiffness of the waste domain is to develop small tensile stresses in the concrete backfill and an increase in mechanical damage.

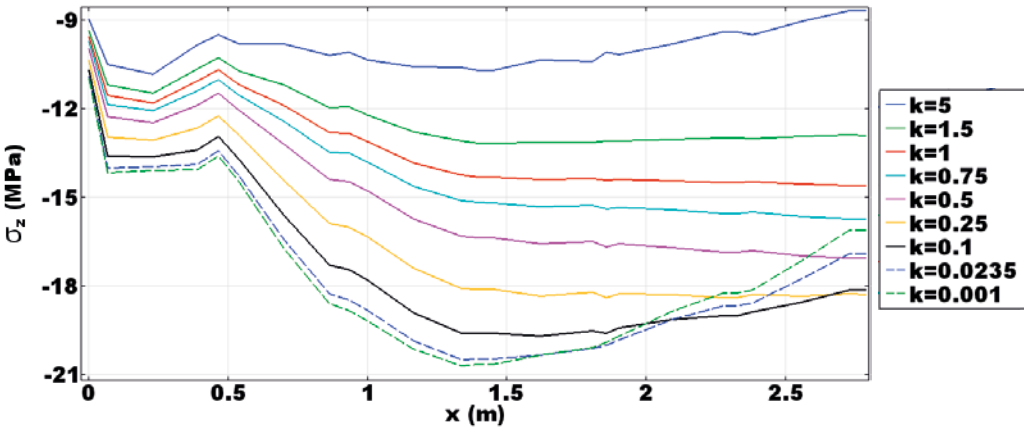

Figure 6-29. *1D profile distribution of vertical stress through concrete backfill at the left of the waste domain after 100 000 years for different values of the stiffness of the waste domain.*

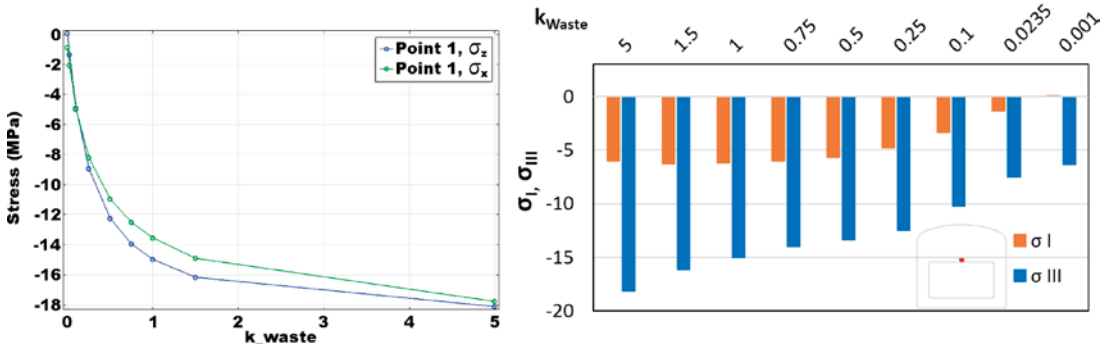

Figure 6-30. *Analysis of horizontal and vertical stresses in two points (Figure 6-26) for different values of stiffness of the waste domain after 100 000 years: z component of stress tensor for point 1 and x component for point 2 (left). Third principal stress on point 1. Results after 100 000 years for different values of stiffness of the waste domain (right).*

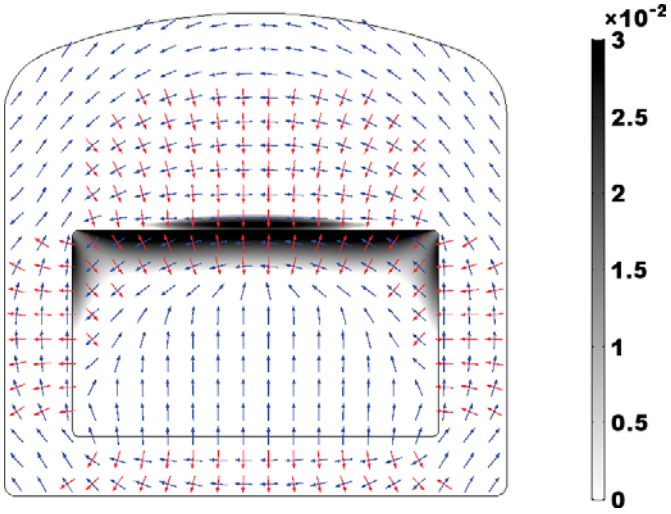

Figure 6-31. *2D spatial distribution of first principal stress magnitude (in MPa) and arrows representing the first (in red) and third (in blue) principal stress direction. Tensile stresses after 100 000 years corresponding to the case with k = 0.001.*

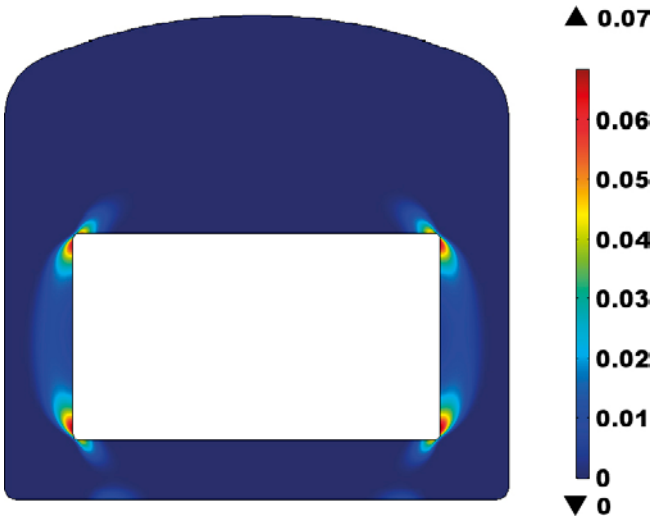

Figure 6-32. *Mechanical damage distribution after 100 000 years for the lowest value of waste domain stiffness.*

6.3.2.5 Effect of the stiffness of the rock

The effect of the rock stiffness on the mechanical behaviour of the concrete backfill is studied in this section. The selected scenario is the Base Case, at a depth of 700 m (Section 6.3.2.1). The quasi-static mechanical analysis is performed at time zero and after 100 000 years of calcium leaching, using different stiffness values for the rock domain, as shown in Table 6-7.

Table 6-7. Young's Modulus values of the rock domain for the different study cases.

Case	Young's modulus (GPa)
1	70
2	60
3	50
4	25

The effect of a reduction in the rock stiffness is an increase in the stresses within the concrete backfill. This is shown in Figure 6-33, where the third principal stress is plotted for each simulation. This is also clearly shown in Figure 6-34, which presents a horizontal profile along the different domains of the third principal stress. The stiffness of the waste domain is very low, and so is its load-bearing capacity. Stresses increase in the concrete backfill, as rock stiffness decreases, especially when the rock is softer than the intact concrete. In that case, stress in the concrete is twice the values in the rock, reaching values that are at least 80 % of the uniaxial compressive strength.

Mechanical damage corresponding to the lowest rock stiffness case is shown in Figure 6-35. The affected regions of the concrete backfill are now clearly visible around the waste domain. Mechanical damage occurs from the concrete-waste interface towards the concrete-rock contact, as opposed to chemical damage that advances from the concrete-rock interface and inwards. The maximum value of mechanical damage in the concrete backfill is 0.17, located in the corners of the waste domain.

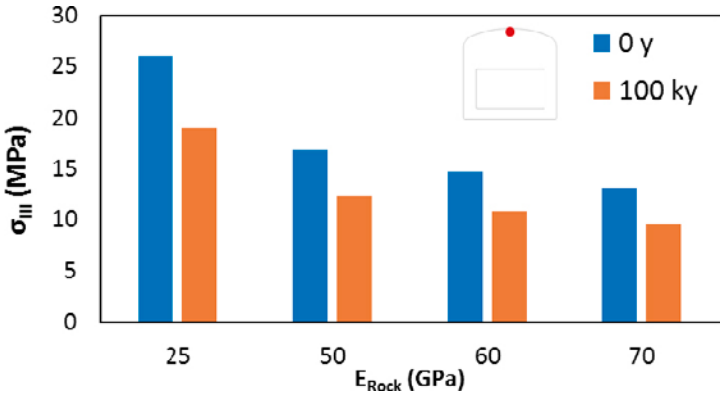

Figure 6-33. *Third principal stress on the highest part of the concrete backfill for different values of the rock stiffness, E_R (GPa). Results at initial time with intact properties of the material and after 100 000 years. Positive values for compression.*

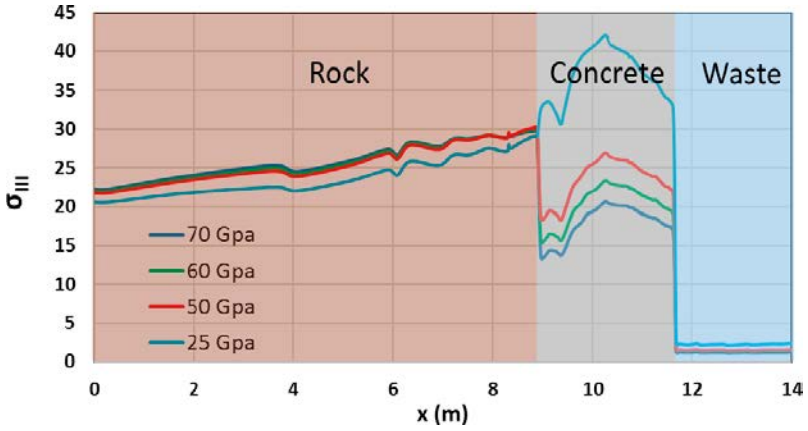

Figure 6-34. *1D profile of third principal stress through the rock, concrete and waste domains for different values of rock Young's modulus. Observation line at middle depth of the repository, positive values for compressive stresses.*

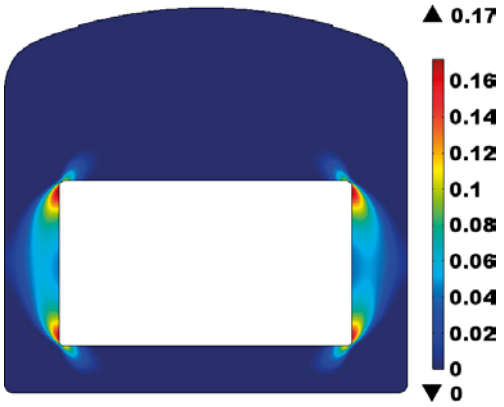

Figure 6-35. *Initial mechanical damage distribution for a rock domain stiffness of 25 GPa.*

6.4 Summary of degradation by calcium leaching

A 2D hydro-chemo-mechanical (HCM) model of the degradation of concrete in the BHK vault of the proposed repository concept for the SFL repository is implemented using iCP (Nardi et al. 2014). In total, a set of 20 simulations are presented (Table 4-1). These simulation cases examine several modelling assumptions related to the mechanical boundary conditions of the host rock and material parameters of the waste and rock domains.

All the calcium leaching HCM models explicitly consider the coupling between chemically-driven porosity changes and the transport properties (i.e. effective diffusion coefficient and hydraulic conductivity). However, the impact of mechanical damage on the transport properties, as described in Section 3.3, is not considered in these simulations. As shown in Section 6.3, this is a valid simplification for most of the simulation cases presented. This is due to the fact that predicted damage values in the concrete backfill are typically below ~0.1 in almost all simulated cases (except in the corners of the waste domain, which locally show larger values). The influence of these mechanical damage levels on transport properties is thought to be small (Section 3.3). The two exceptions are the sensitivity cases studying the effect of glaciation-induced stresses (Section 6.3.2.3) and the effect of a very low rock stiffness (Section 6.3.2.5). In these cases, higher values of mechanical damage are predicted in the concrete backfill, which could have a non-negligible impact on transport properties.

The active loads on the vault considered in the model are self-weight of the structure and in-situ stresses. In some cases, glaciation-induced stresses are also considered. The model does not consider creep deformations of the concrete or the rock. Water pressure is also not explicitly taken into account in the model, which is due to the fact that hydraulic equilibrium conditions are expected in the long-term, as studied in this work.

The main conclusions of each study are summarized below.

Base Case. The Base Case considers a repository depth of 500 m oriented in the direction of the major horizontal stress, using the mechanical properties summarized in Table 6-4. In-situ stresses correspond to those calculated by Hakami et al. (2008) and given by Equations 4-2 and 4-3. The results indicate that mechanical damage only occurs locally in the concrete backfill, at the corners of the waste domain. The rest of the backfill is unaffected by mechanical damage even after 100 000 years of calcium leaching. Chemical degradation leads to an accumulation of chemical damage in the concrete backfill close to the rock. This results in a softer material in that region, with a higher capacity to sustain deformations from the rock, thus having a positive effect on the intact concrete.

Repository depth. Given the depth-dependent nature of in-situ stresses, a sensitivity case that considers an increase of the repository depth from 500 to 700 m is simulated. The increase of 200 m in depth leads to an increase of 40 % in the vertical stress and 37 % in the minimum horizontal stress. Mechanical damage is very similar to the Base Case, with only marginal increases of damage at the sides of the waste domain. Vault stability is not compromised.

Repository orientation. The vault axis will be aligned as close as possible to the maximum horizontal stress direction. However, there is an uncertainty in the direction of horizontal in-situ stresses that has been quantified as ±15° (Hakami et al. 2008). A rotation of the vault of 15° can increase the in-situ horizontal stress in the direction perpendicular to the vault axis. A sensitivity study of the effect of 15° rotation is conducted for a repository depth of 700 m. The results show that such a rotation leads to a higher degree of confinement and a reduced size of the damaged zone in the concrete backfill. In this case, mechanical damage only appears in the corners of the waste domain.

Effect of glaciation-induced stresses. The formation of an extensive ice sheet on top of the rock hosting the repository can significantly impact the in-situ stresses around the vault. The sensitivity study considers the simultaneous action of chemical degradation and time-dependent in-situ stresses induced by a glaciation. The results indicate that mechanical damage can be substantial. This is because the glaciation-induced stresses tend to increase the ratio of vertical to minimum horizontal stresses. In such a case, large tensile and compressive stresses can be observed, approaching the uniaxial tensile and compressive strengths, respectively. Locally, mechanical damage reaches values of up to 0.21, while mechanically damage paths (with values of around 0.07) are formed through the backfill, connecting the rock and waste domains. The effect of mechanical damage on transport properties is potentially important in this case, although not accounted for in the simulations.

Effect of the elastic properties of the waste and rock domains.

Stiffness reduction of the waste and rock domains leads to an increase in the concrete stress state. Assuming a very soft material for the waste domain increases the tensile and compressive stresses in the concrete backfill. The rock stiffness has relatively small effects when ranging from 50 to 70 GPa (or higher). However, if the stiffness is below that of concrete, e.g. to simulating the effect of settlements or rock creep, stresses can increase substantially as does the mechanical damage.

Overall, it may be concluded that even in the most adverse conditions considered in this study, mechanical damage of the concrete backfill in the BHK vault is localized near the waste domain and presents relatively low values, i.e. below ~0.1. This means that the mechanical stability of the repository is not compromised. It also indicates that the impact of mechanical processes on hydraulic conductivity and diffusion coefficient, and therefore on chemical degradation, is not significant. One exception is the case of glaciation-induced stresses with the repository at 700 m. In that case, chemical degradation could be accelerated due to the appearance of mechanical damaged zones in the backfill, connecting the rock and waste domains. The second exception is the case with a very low rock stiffness (Section 6.3.2.5).

7 HCM modelling of sulphate attack in the BHK vault

7.1 Description of the conceptual model

The HCM model for sulphate attack is similar to the model used for calcium leaching described in Section 6.1. The geometry (Figure 6-1), modelled domains and material properties (Table 6-2 through Table 6-5) are identical, as are the initial and boundary conditions for groundwater flow and reactive transport. The main differences with the conceptual model presented in Section 6.1 are:

- The composition of the groundwater used for external sulphate attack simulations, presented in Table 7-1, which is the boundary condition for solute transport.
- The calculation of expansions due to ettringite and thaumasite precipitation as detailed in Section 5.1.3

The composition of groundwater is the same as presented in Table 6-1, adjusted with a high sulphate concentration (0.01 M). This concentration level is among the highest measured in the Laxemar area (Figure 4-7 and Kalinowski 2009).

Table 7-1. Groundwater composition used for the sulphate attack simulations. The sulphate concentration is among the highest concentrations measured at Laxemar (Kalinowski 2009), see Section 4.2. The basis of the groundwater corresponds to the composition in Table 6-1.

	Groundwater
pH	8.64
Temperature (°C)	25
Species (totals, mol/kg water)	
Al	1.21×10^{-6}
C	6.91×10^{-4}
Ca	5.26×10^{-4}
Cl	4.53×10^{-3}
K	7.60×10^{-5}
Mg	5.00×10^{-3}
Na	1.42×10^{-2}
S	1.00×10^{-2}
Si	1.42×10^{-4}

In this section, the mechanical analysis is performed in a fully coupled and a one-way coupling fashion. The one-way coupled model has a similar setup as the HCM models for calcium leaching. This means that mechanical analysis is solved with input from the reactive transport simulation, but mechanical damage does not impact transport properties of the concrete. This assumption is valid when the mechanical damage is low to moderate. Results from the one-way coupled model are presented in Section 7.3.1. The fully coupled scenario explicitly considers in the reactive transport simulation the feedback between mechanical damage and transport properties for sulphate attack. Results are presented in Section 7.3.2.

It should be noted that at present uncertainties in model parameterization are significant due to a lack of knowledge on the development of several key processes. Available models for simulating expansions due to sulphate attack have only been verified under laboratory conditions. These experiments are typically performed using mortar samples immersed in a sulphate solution. Thus, any effects of the simultaneous exposure of concrete to external loads and sulphate-rich solutions are not considered. For instance, a gradual reduction of measured expansions has been reported when increasing the compressive stresses on samples exposed to sulphate attack (Piasta and Schneider 1992, Živica and Szabo 1994). Existing models have only been applied to ettringite precipitation. However, in this study thaumasite also forms. Therefore, the effect of thaumasite formation on expansions is accounted for as a first approximation in the same way as ettringite.

Expansions predicted by existing models are sensitive to a key parameter that usually shows a large scatter. This parameter β (Equation 5-10) determines to a large extent the magnitude of volumetric expansions and is supposed to physically represent the fraction of porosity that needs to be filled before any expansion is observed. Another important source of uncertainty is the effect of mechanical damage on transport properties, as discussed in Section 3.3.

7.2 Numerical model setup

This section presents the details of the numerical implementation using iCP (Nardi et al. 2014).

7.2.1 Finite element mesh

The 2D model domains are discretized using triangular elements, with different discretization for reactive transport (Figure 7-1) and mechanical analyses (Figure 7-2). Maximum element size is 5.5 m in the rock and 0.6 m in the vault. The total number of elements is 15 256, of which 7 356 correspond to the vault, and 6 010 and 1 346 correspond to the concrete and waste domains, respectively. Average element sizes for the rock, concrete backfill, and waste domains are respectively 2.36 m, 0.294 m, and 0.440 m. For the reactive transport simulation, the same finite element mesh as in Figure 7-1 is used for the concrete backfill and waste domain. A finer discretization is used for the reactive transport processes, compared to the HCM models in Section 6, in an attempt to more accurately capture the penetration front of sulphate-bearing phases.

Groundwater flow and reactive solute transport use linear elements, while quadratic elements are used for the mechanical analysis. Moreover, a regularization technique is used for solving the mechanical damage model (Section 5.1.2). This regularization technique is implemented as an additional physics interface in Comsol, coupled to the mechanical analysis physics interface. The discretization used for regularization is the same as the mechanical analysis, although the order to these elements is quartic, which is needed for numerical stability. The characteristic length used in the simulations for the regularization of the damage model is equal to 0.2 m, as proposed by Sellier et al. (2011) for a similar study using a similar finite element size.

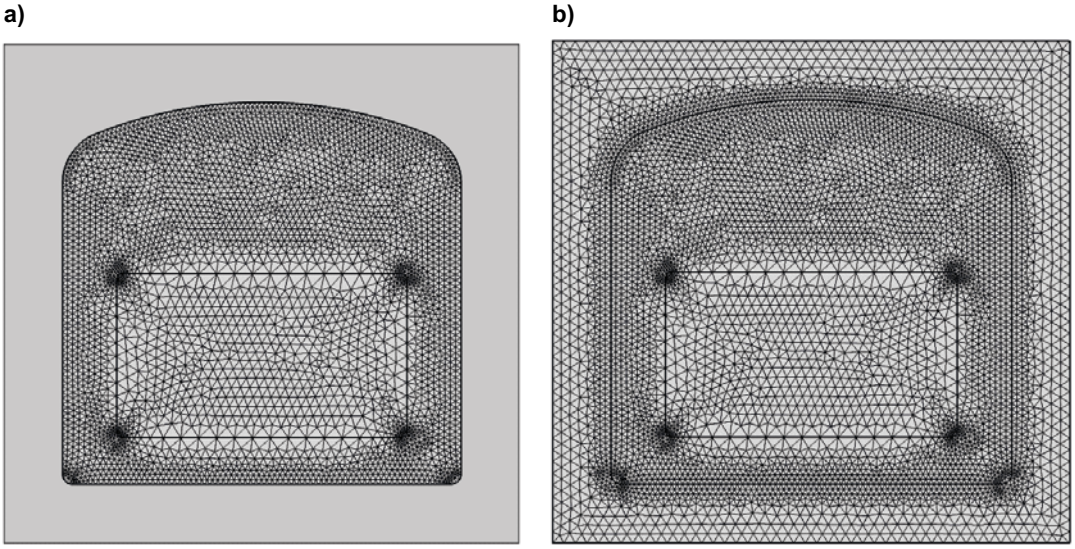

Figure 7-1. *Finite element meshes used for (a) reactive transport and (b) groundwater flow.*

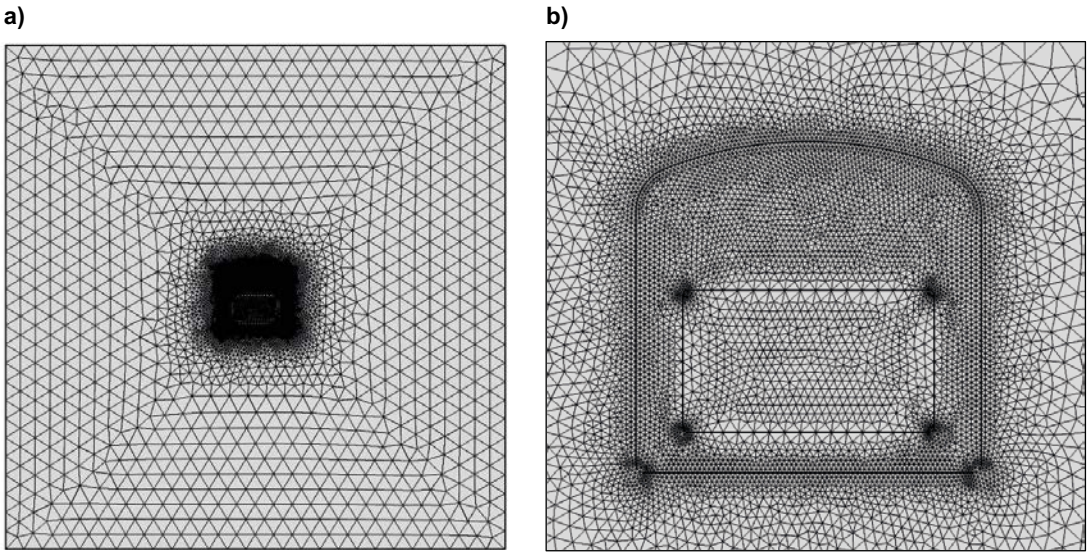

Figure 7-2. (a) Full finite element mesh used for the mechanical model and (b) a zoom in around the vault.

7.2.2 Temporal discretization

The temporal discretization used for the iCP communication steps between Comsol and Phreeqc increases stepwise from time steps of 2 years to 7 years. These time steps sizes satisfy the Courant and von Neumann stability criteria.

7.2.3 Initial and boundary conditions

Groundwater flow, solute transport and mechanical analysis are solved with the same boundary and initial conditions presented in Section 6.2.3. Two cases of in-situ stresses are considered: vault axis aligned with the major horizontal stress, and a 15° clockwise rotation of the vault.

7.3 Results

Results from the simulation of sulphate attack are presented as 2D distribution plots at given times or as 1D profiles, as shown in Figure 7-3. 1D plots are defined along a horizontal line through the concrete backfill, to the left of the waste domain.

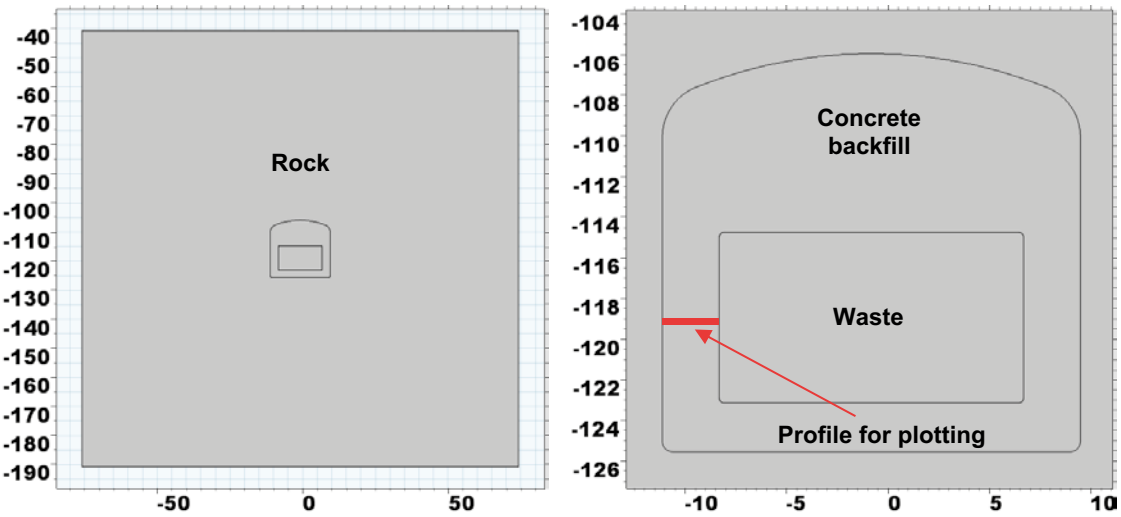

Figure 7-3. Geometry and location of the profile for 1D representation of results.

7.3.1 One-way coupled HCM model

In this case, the effect of mechanical damage on the transport properties of concrete is not considered. However, it is noted that the coupling between porosity changes due to dissolution/precipitation of minerals and transport properties is considered in the simulation.

Sulphates from groundwater react with calcium aluminates in the cement matrix to form ettringite and thaumasite. As shown in Figure 7-4 and Figure 7-5, after 100 000 years the ettringite front in the backfill has reached a depth of 1.25 m on the left side, while thaumasite has precipitated in the first 0.5 m. At the rock-concrete interface, these minerals eventually dissolve. As a result of the precipitation of these sulphate-bearing phases, concrete is subject to localized volumetric expansions, as shown in Figure 7-6.

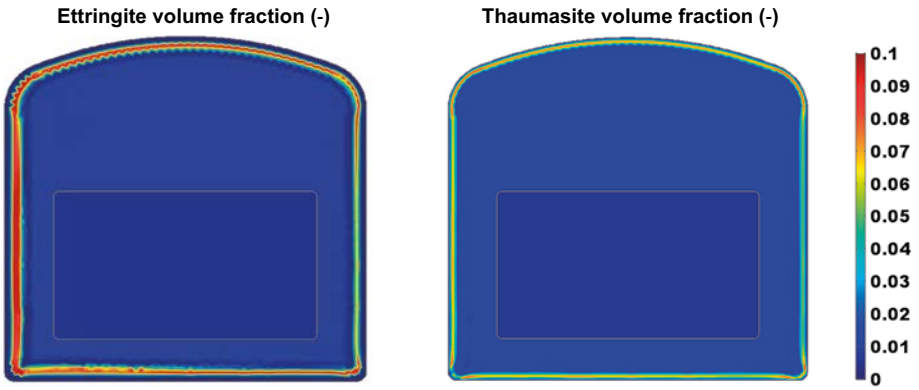

Figure 7-4. One-way coupled HCM model of sulphate attack results: 2D spatial distribution of ettringite (left) and thaumasite (right) volume fractions (–) after 100 000 years.

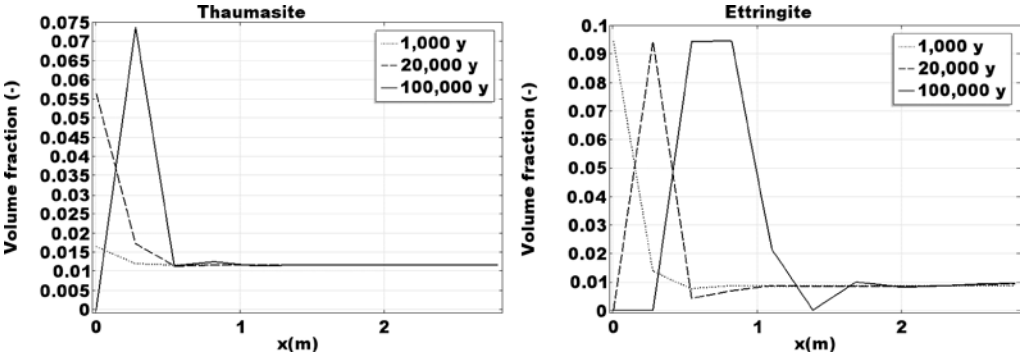

Figure 7-5. One-way coupled HCM model of sulphate attack results: 1D evolution of ettringite and thaumasite volume fraction profiles (–), for 1 000, 20 000 and 100 000 years.

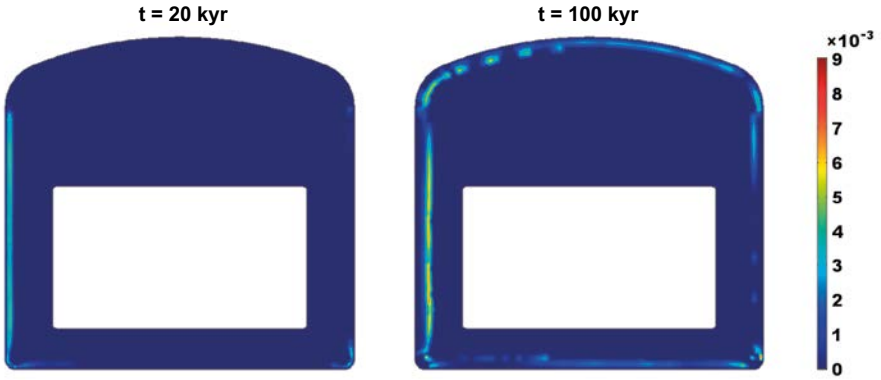

Figure 7-6. One-way coupled HCM model of sulphate attack results: 2D spatial distribution of volumetric expansions from sulphate attack (–) after 20 000 (left) and 100 000 years (right).

As expected, the chemical and mechanical damage are not symmetric. As presented in Figure 7-7, the left side of the vault is preferentially damaged due to the effect of groundwater flow. In this zone, mechanical damage extends over the first ~1.5 meters of the concrete backfill, reaching values close to 1 (full damage) in the first 0.84 m. In turn, chemical damage reaches a maximum value of 0.3 and extends over the first 0.84 m. As a result of chemical and mechanical damage, the Young's modulus is significantly lower than the intact value over the first ~1.5 m, and reaches values close to 0 (i.e. full damage) in the first 0.84 m of the concrete backfill (Figure 7-7).

The evolution of the Young's modulus in the concrete backfill conditions the mechanical behaviour of the system. Its impact is analysed in terms of maximum compressive stresses and development of tensile stresses. The vertical compressive stress distribution in the concrete backfill to the left of the waste domain is shown in Figure 7-8. Compressive stresses are not significant compared to the uniaxial compressive strength. However, after 100 000 years there is a significant redistribution compared to the more uniform stresses before sulphate attack. As a result of accumulated damage in the outer part of the backfill, stresses drop to very low values, while the inner part of the backfill is subject to significantly higher stresses. Tensile stresses are important for unreinforced concrete due to its low tensile strength compared to compressive strength. A study of the first principal stress reveals that no regions in the concrete backfill are subject to positive (i.e. tensile) stresses, throughout the simulated time.

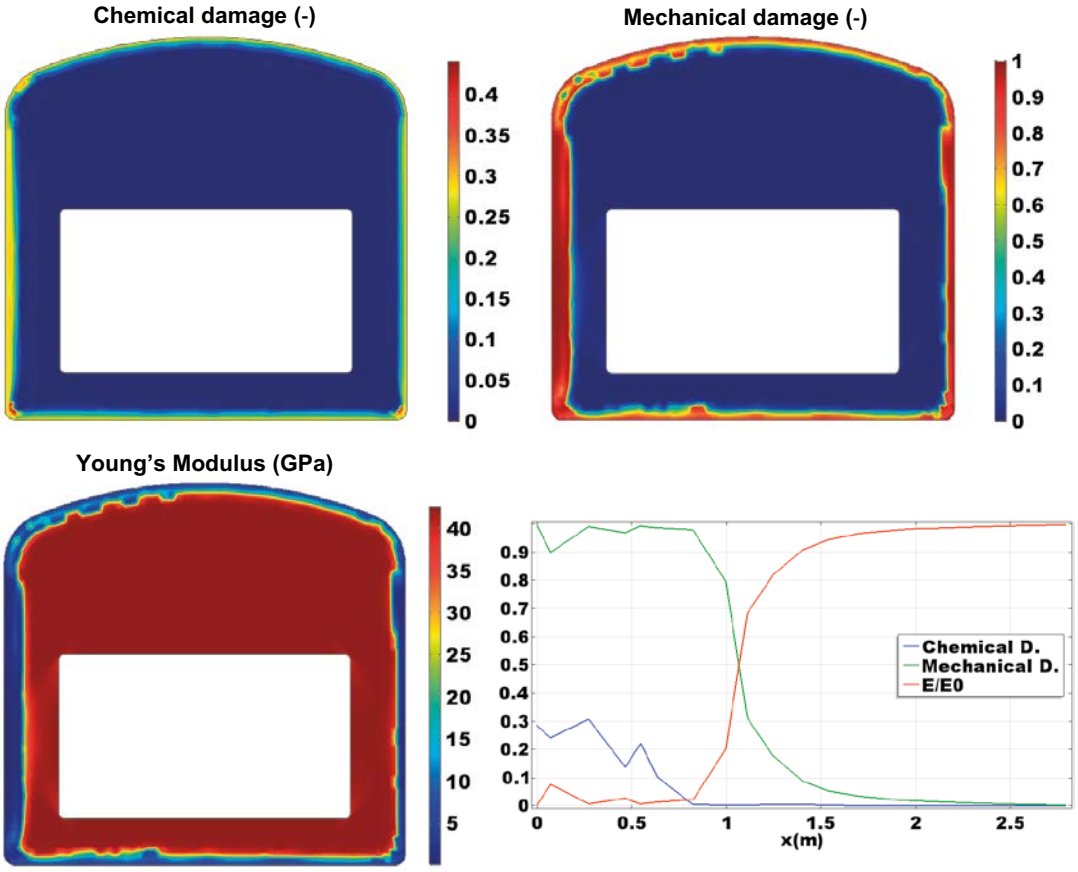

Figure 7-7. *One-way coupled HCM model of sulphate attack results after 100 000 years: 2D spatial distribution of chemical damage (upper left), mechanical damage (upper right) and Young's modulus (lower left). Young's modulus distribution in GPa, maximum value of undamaged material E_0 = 42.642 GPa, minimum modulus in almost completely damaged zone E = 0.1589 GPa. 1D spatial profiles (Figure 7-3) of the 3 variables after 100 000 years (lower right), relative Young's modulus referred to undamaged value.*

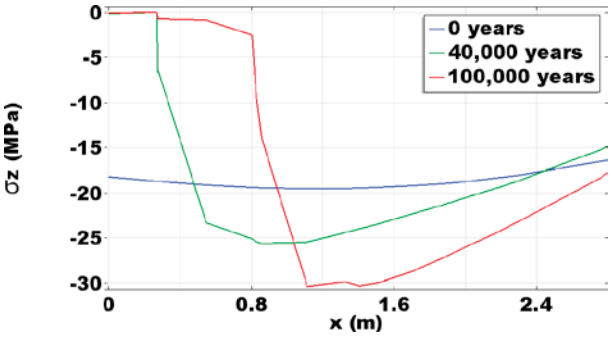

Figure 7-8. *One-way coupled HCM model of sulphate attack results: vertical compressive stress distribution in the concrete backfill to the left of the waste domain.*

As stated above, in the one-way coupled scenario mechanical damage does not impact the transport properties of concrete. This assumption is representative of reactive transport models with no mechanical analysis. However, porosity changes due to mineral reactions are considered, which impact the transport properties. Figure 7-9 shows porosity, effective diffusion coefficient and hydraulic conductivity after 100 000 years. A 1D profile that shows the three variables relative to their initial values is also presented in that figure. It is clear that ettringite precipitation reduces the porosity to values lower than initial (between 0.4 and 1.2 m). Near the boundary, porosity increases up to two times the initial value, when ettringite dissolves and calcium leaching proceeds with the dissolution of the main hydrates. The effective diffusion coefficient and hydraulic conductivity distributions are a consequence of the porosity profile. As with traditional reactive transport models (e.g. Grandia et al. 2010b), the precipitation of ettringite does not lead to higher values of the transport properties when using the one-way coupled HCM model. As a result, the model predicts that the rate of degradation is slower than a more realistic case where mechanical damage enhances the sulphate ingress rate. To remedy this, a coupled HCM model is presented in the next section.

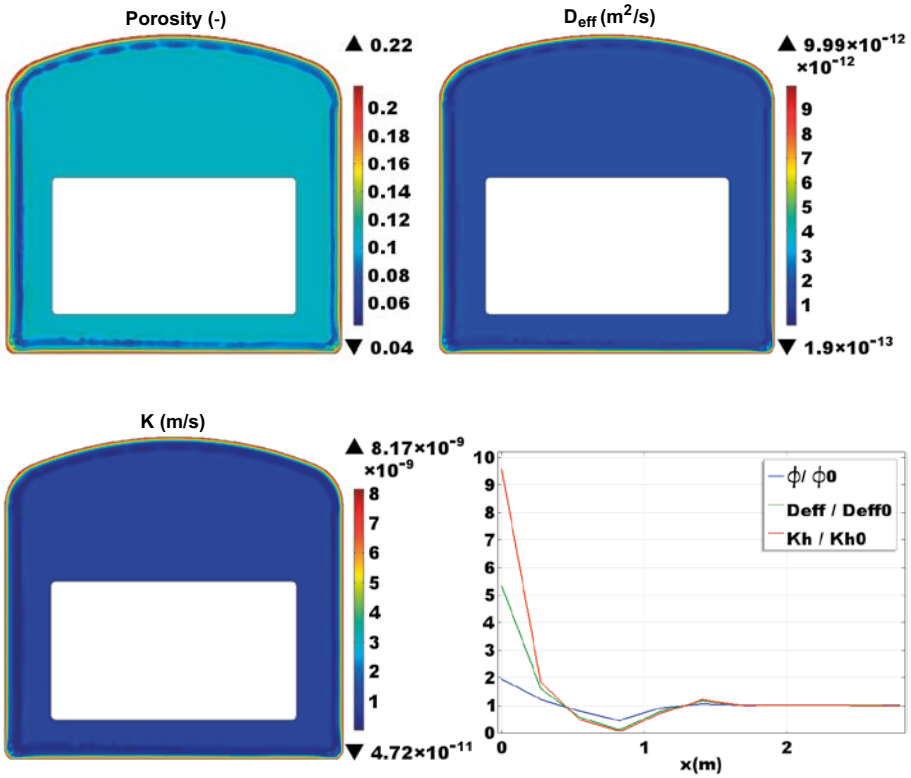

Figure 7-9. *One-way coupled HCM model of sulphate attack results after 100 000 years: 2D spatial distribution of porosity (upper left), effective diffusion coefficient in m^2/s (upper right) and hydraulic conductivity in m/s (lower left).1D spatial profiles of the 3 relative variables, referred to their initial values (lower right). Their initial values are $\varphi = 0.11$ (–), $D_{eff} = 3.50 \times 10^{-12}$ m^2/s, and $K = 8.30 \times 10^{-10}$ m/s.*

7.3.2 Fully coupled HCM model

The coupled HCM model presented in this section explicitly considers the impact of mechanical damage on transport properties (see Section 3.3). As discussed in previous sections, transport properties of concrete are expected to increase substantially if considerable mechanical damage accumulates. The following implementation focuses on the coupling between reactive transport and the mechanical analysis. In this model, concrete transport properties depend on mechanical damage that results from expansions due to mineral precipitation.

In this section, a preliminary implementation of a coupled HCM model for sulphate attack is used to analyse the impact of mechanical damage on transport properties. To this end, several assumptions are introduced. The methodology is to relate mechanical damage obtained in the one-way coupled analysis with volumetric expansions due to ettringite and thaumasite precipitation calculated using Equation 5-10.

The relations introduced in the coupled HCM model are the following:

- Ettringite and thaumasite precipitation vs. volumetric expansion (Section 5.1.3).
- Volumetric expansion and mechanical damage (obtained from the one-way coupled simulation, Section 7.3.1).
- Mechanical damage and permeability (Equation 3-8).
- Mechanical damage and diffusion (Equation 3-9).

With these relations, mechanical damage is calculated directly in the reactive transport simulation as a function of mineralogical changes, updating the transport properties at each time step. In this scheme, the reactive transport step is solved first, explicitly considering the impact of mechanical damage on transport properties. The mechanical step is performed subsequently with input from reactive transport step.

Figure 7-10 and Figure 7-11 present the ettringite and thaumasite volume fractions after 14 500 years of interaction with a sulphate-rich groundwater. The effect of coupling the transport properties with mechanical damage results in a substantial increase of the degradation rate compared to the one-way coupled model results. This is also shown also in Figure 7-12, where ettringite precipitation profiles for fully coupled and one-way coupled models are compared after 10 000 years. Figure 7-13 shows volumetric expansions at two different times, as a result of ettringite precipitation. In Figure 7-14, the impact of sulphate attack on chemical and mechanical damage is shown after 14 500 years. The stiffness of the concrete backfill is also presented in this figure. After 14 500 years, the entire thickness of the bottom-left concrete backfill is totally degraded, and the mechanical analysis stops due to numerical converge issues. At the end of the simulation sound concrete can only be observed in the innermost meter of the backfill (Figure 7-14), while in the bottom left corner of the vault full damage reaches the waste domain.

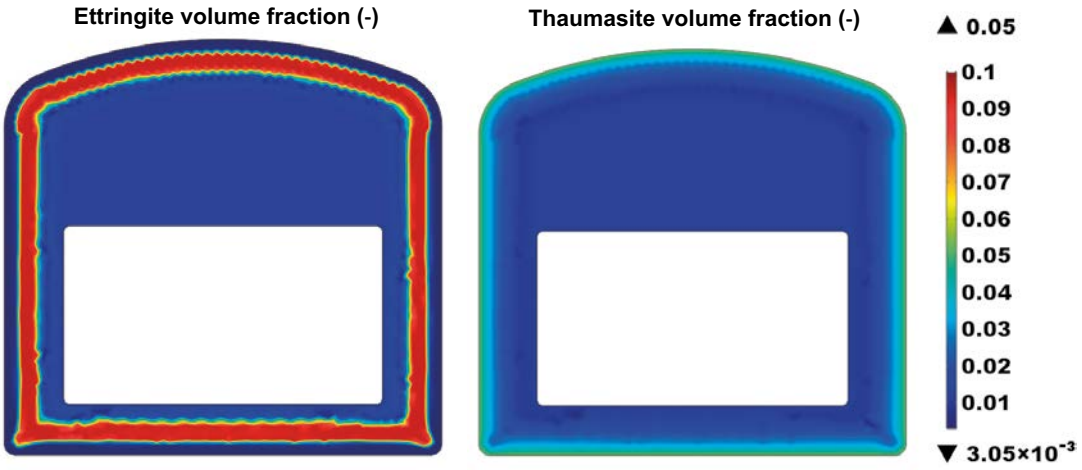

Figure 7-10. *Fully coupled HCM model of sulphate attack results: 2D spatial distribution of ettringite (left) and thaumasite (right) volume fractions (–) after 14 500 years.*

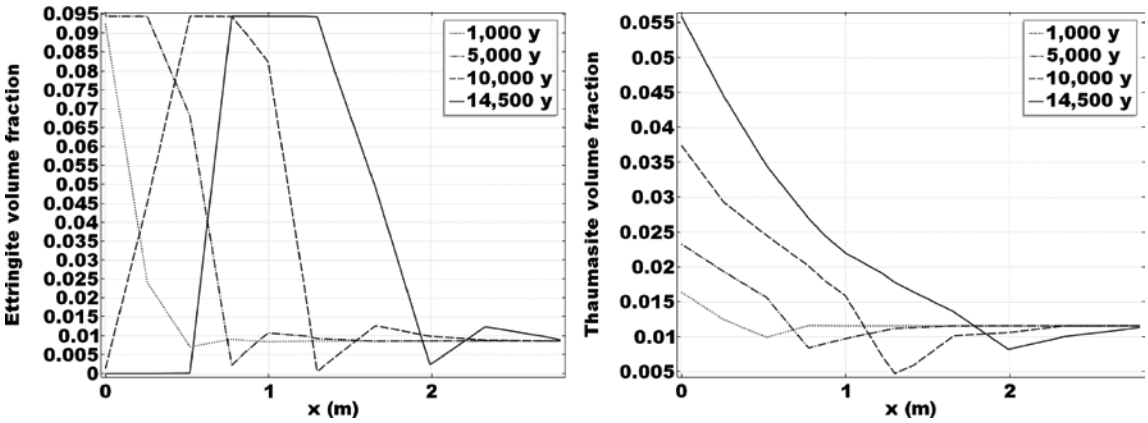

Figure 7-11. *Fully coupled HCM model of sulphate attack results: 1D profiles at different times of ettringite (left) and thaumasite (right) volume fraction.*

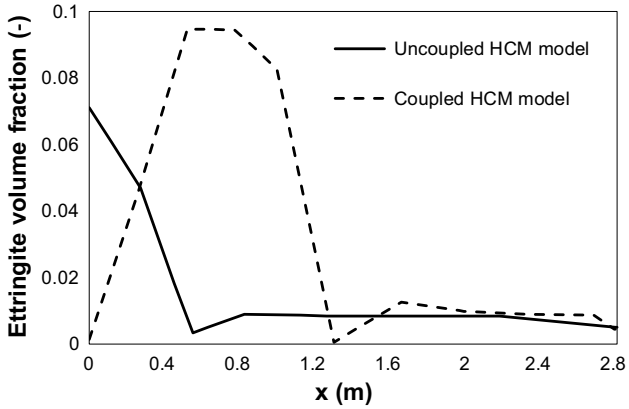

Figure 7-12. *Comparison of fully coupled and one-way coupled HCM models of sulphate attack: 1D profiles after 10 000 years of ettringite volume fraction.*

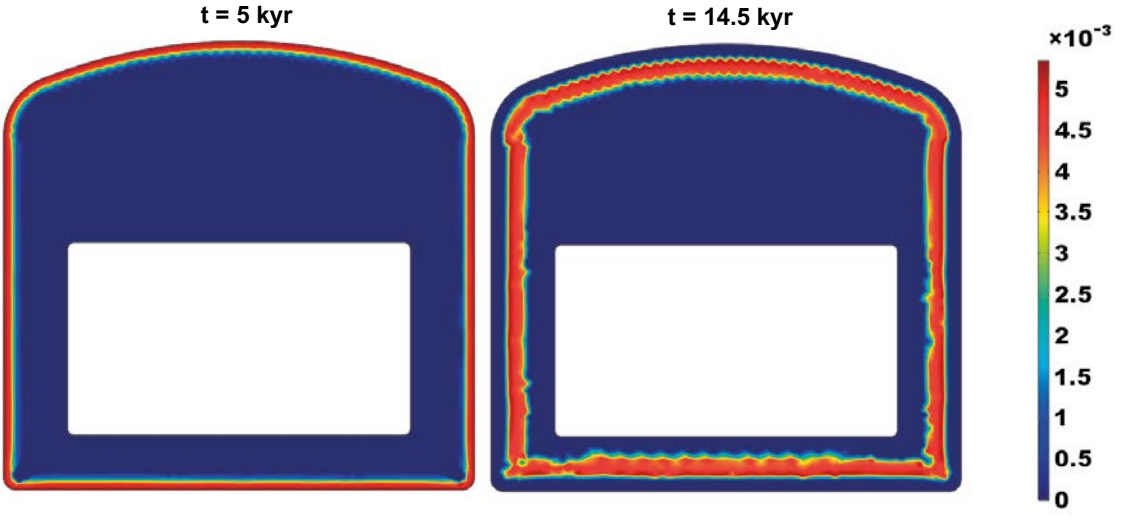

Figure 7-13. *Fully coupled HCM model of sulphate attack results: 2D spatial distribution of volumetric expansions (–) due to sulphate attack after 5 000 (left) and 14 500 years (right).*

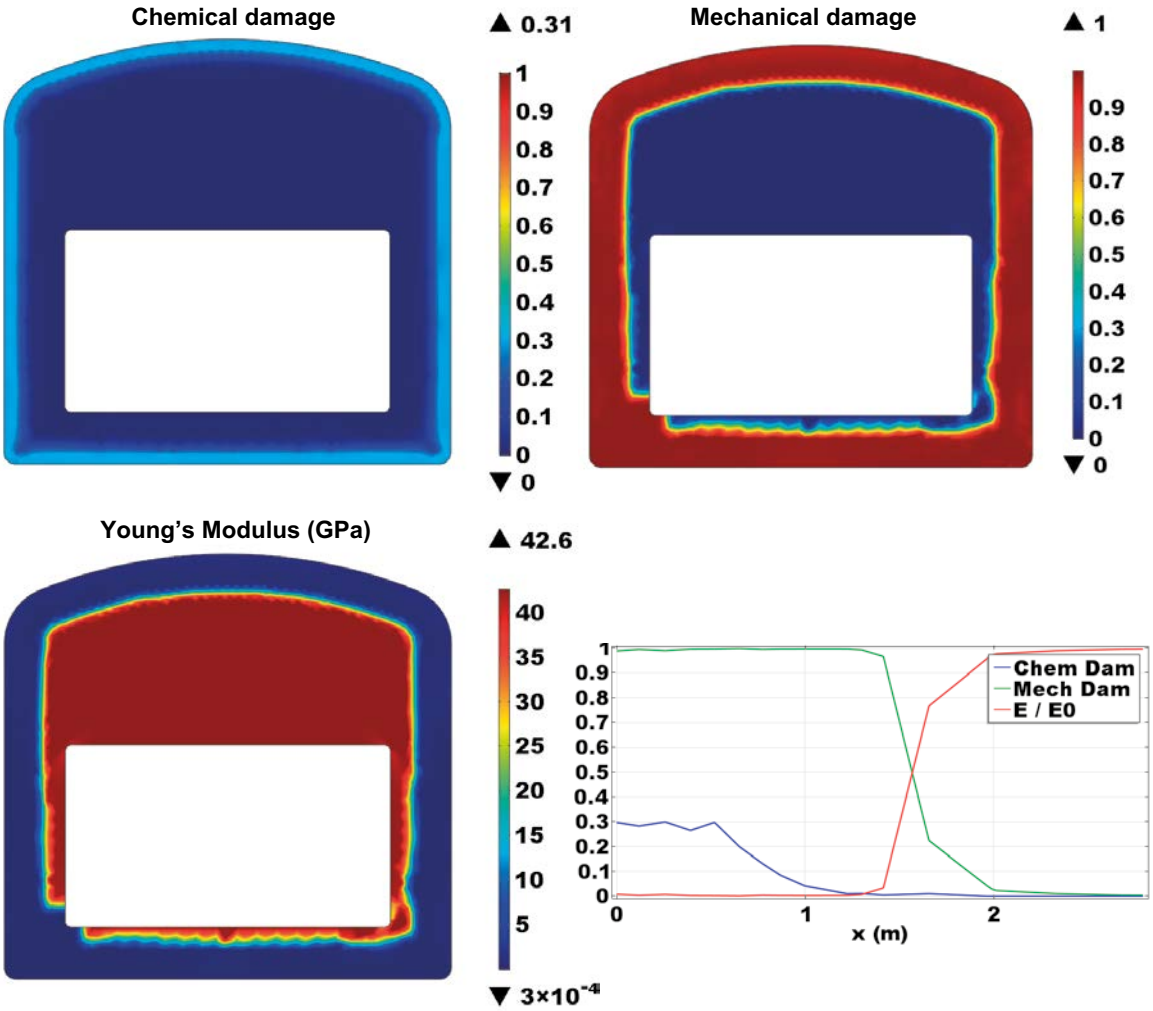

Figure 7-14. *Fully coupled HCM model of sulphate attack results: 2D spatial distribution of chemical damage (upper left), mechanical damage (upper right) and Young's modulus (in GPa, lower left) after 14 500 years. Maximum value of undamaged material E_0 = 42.642 GPa. 1D spatial profiles of the 3 variables after 14 500 years, relative Young's modulus referred to undamaged value (lower right).*

Figure 7-15 shows the transport properties and porosity distribution after 14 500 years of interaction with a sulphate-rich groundwater. Compared to the one-way coupled case (Figure 7-9), the increase in effective diffusivity and hydraulic conductivity is much larger. As a result, sulphate ingress is enhanced and expansions lead to additional damage.

7.4 Summary of degradation by external sulphate attack

A HCM model for sulphate attack has been implemented using iCP and verified against experimental data (Lagerblad 1999). The model is used to analyse the effect of sulphate-rich groundwater composition on the stability of the BHK concrete vault in the SFL repository. Simulation results of a fully coupled and a one-way coupled HCM model setup are presented.

The one-way coupled case shows significant damage due to sulphate attack, affecting ~1.5 m of the concrete backfill after 100 000 years. However, the stability of the vault is not severely compromised. In contrast, the coupling of transport properties with mechanical damage leads to a much faster chemical degradation. In this case, the model predicts severe damage in the concrete backfill after 14 500 years, with the entire thickness of the bottom-left concrete backfill totally degraded.

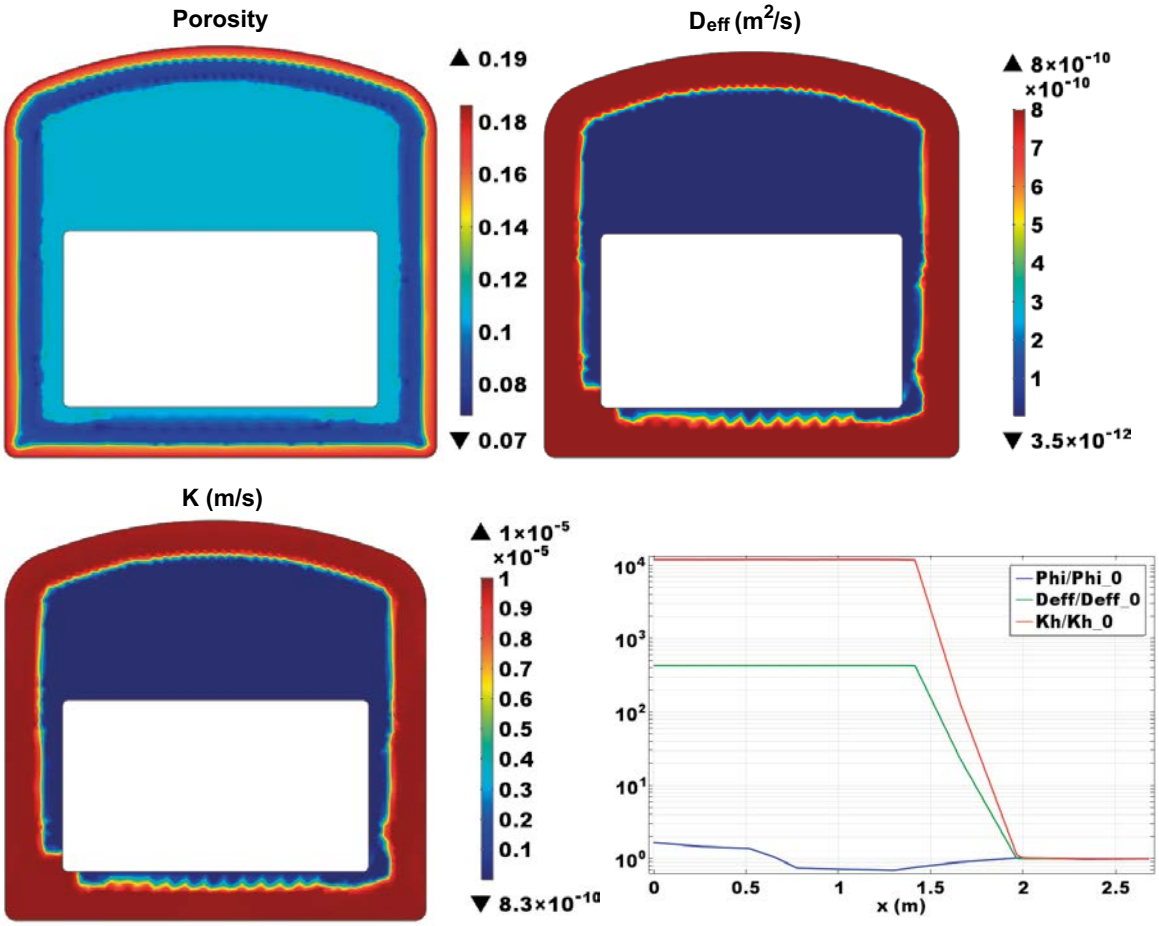

Figure 7-15. *Fully coupled HCM model of sulphate attack results: 2D spatial distribution of porosity (upper left), effective diffusion coefficient (in m^2/s, upper right) and hydraulic conductivity (in m/s, lower left) after 14 500 years. 1D spatial profiles of the 3 variables after 14 500 years, relative to the undamaged values (lower right).*

8 Summary and conclusions

In this study, hydro-chemo-mechanical models are developed to study concrete degradation in the BHK vault of the proposed repository concept for the SFL. The goal is to assess the impact of mechanical processes on the long-term chemo-mechanical performance of the cementitious barriers. To this end, 2D models of a cross-section of the BHK vault are implemented using iCP, similar to Idiart and Shafei (2019).

The chemical degradation processes of concrete that are potentially important in SFL are calcium leaching and sulphate attack. A short literature review of available chemo-mechanical models for these two degradation processes is presented. Based on this review, several constitutive models are selected and implemented using iCP to analyse the key chemo-mechanical couplings. To account for mechanical damage, a regularized version of Mazars' damage model is implemented. Chemical damage due to mineral reactions and porosity changes is considered via a multi-scale homogenization model (see Stora et al. 2010, Bary et al. 2014). Volumetric expansions due to ettringite and thaumasite formation are calculated based on the assumption that the products have a larger volume than the reactants, as considered by most of the available models. The impact of mechanical damage on transport properties is only considered for the sulphate attack study. Empirical relations for hydraulic conductivity and effective diffusivity are used, based on a literature review of available models.

Several verification cases are presented for the regularized Mazars' damage model, calcium leaching processes, and expansions due to sulphate attack. It is concluded that the proposed HCM model is able to reproduce the main features of mechanical and chemical damage of concrete and the coupling between calcium leaching and sulphate attack with mechanical performance.

The HCM model is first used to study calcium leaching processes. A Base Case is defined that is based on Case I of Idiart and Shafei (2019). The repository is assumed to be located at a depth of 500 m and the vault axis is assumed to be parallel to the maximum horizontal stress at Laxemar. Active loads considered are self-weight and in-situ stresses from the rock. A set of sensitivity cases is proposed to analyse the impact of the depth and orientation of the vault, the stiffness of the waste and rock domains, and the impact of glaciation-induced stresses. The results indicate that the mechanical stability of the vault is not compromised due to the coupling of active mechanical loads and calcium leaching. Mechanical damage is expected to be very small in most of the cases, concentrated at the backfill-waste interfaces. An exception is the case that considers glaciation-induced stresses. In that case, mechanical damage can be substantial, extending over large regions of the concrete backfill.

On the other hand, chemical damage always occurs from the rock-concrete interface inwards due to the leaching of the main cement hydrates. As a consequence, the stiffness of the backfill in the leached zone decreases substantially, leading to the development of a more deformable layer between the rock and the intact concrete. This results in a stress redistribution, where stresses in the chemically-damaged zone are transferred to the rock and the intact concrete.

Next, the potential impact of sulphate-rich groundwater in Laxemar on the development of external sulphate attack in the BHK vault is studied with the HCM model. First, a one-way coupled scenario is evaluated, where the impact of mechanical damage on transport properties is not considered. As a result, after 100 000 years there is significant damage in the outer concrete backfill, although the stability of the vault is not severely compromised. In contrast, a simulation case where a fully coupled setup is considered leads to a much faster degradation. In that case, mechanical instabilities occur after 14 500 years. It is noted that these results are based on several assumptions that at present are subject to a high level of uncertainty, as discussed in Section 7.1.

References

SKB's (Svensk Kärnbränslehantering AB) publications can be found at www.skb.com/publications. SKBdoc documents will be submitted upon request to document@skb.se.

Abarca E, Sampietro D, Miret M, von Schenck H, 2016. Initial modelling of the near-field hydrogeology Exploring the influence of host rock characteristics and barrier properties Report for the safety evaluation SE-SFL. SKB R-16-02, Svensk Kärnbränslehantering AB.

Adenot F, Buil M, 1992. Modelling of the corrosion of the cement paste by deionized water. Cement and Concrete Research 22, 489–496.

Babaahmadi A, 2015. Durability of cementitious materials in long-term contact with water. PhD thesis. Chalmers University of Technology, Sweden.

Babaahmadi A, Tang L, Abbas Z, 2014. Mineralogical, physical and chemical characterization of cementitious materials subjected to accelerated decalcification by an electro-chemical method. Nordic Concrete Research 1/2014, 181–198.

Babaahmadi A, Tang L, Abbas Z, Mårtensson P, 2015. Physical and mechanical properties of cementitious specimens exposed to an electrochemically derived accelerated leaching of calcium. International Journal of Concrete Structures and Materials 9, 295–306.

Bary B, 2008. Simplified coupled chemo-mechanical modeling of cement pastes behavior subjected to combined leaching and external sulfate attack. International Journal for Numerical and Analytical Methods in Geomechanics 32, 1791–1816.

Bary B, Bournazel J.P, Bourdarot E, 2000. Poro-damage approach applied to hydro-fracture analysis of concrete. Journal of engineering mechanics, ASCE 126(9), 937–943.

Bary B, Leterrier N, Deville E, Le Bescop P, 2014. Coupled chemo-transport-mechanical modelling and numerical simulation of external sulphate attack in mortar. Cement and Concrete Composites 49, 70–83.

Basista M, Weglewski W, 2009. Chemically assisted damage of concrete: a model of expansion under external sulfate attack. International Journal of Damage Mechanics 18, 155–175.

Bazant Z P, Chern J C, 1985. Concrete creep at variable humidity: constitutive law and mechanism. Materials and Structures 18, 1–19.

Bazant Z P, Hauggaard A B, Baweja S, Ulm F-J, 1997. Microprestress-solidification theory for concrete creep. I. Aging and drying effects. Journal of Engineering Mechanics 123, 1188–1194.

Bourdarot E, 1991. Application of a porodamage model to analysis of concrete dams. Note EDF/NEH.

Brown P, Taylor H, 1998. The role of ettringite in external sulfate attack. In Marchand J, Skalny J P (eds). Materials science of concrete: sulphate attack mechanisms. Westerville, OH: The American Ceramic Society, 73–98.

Carlsson A, Martin D, Christiansson R, 2014. Site Engineering Report – SER – Projekt SFR utbyggnad. SKB R-14-17, Svensk Kärnbränslehantering AB.

Carman P, 1937. Fluid flow through granular beds. Transactions of the Institution of Chemical Engineers 15, 155–166.

Cefis N, Comi C, 2014. Damage modelling in concrete subject to sulfate attack. Fracture and Structural Integrity 29, 222–229.

Cefis N, Comi C, 2017. Chemo-mechanical modelling of the external sulfate attack in concrete. Cement and Concrete Research 93, 57–70.

Christensen R M, Lo K H, 1979. Solutions for effective shear properties in 3 phase sphere and cylinder models. Journal of the Mechanics and Physics of Solids 27, 315–330.

Clifton J R, Pommersheim J M, 1994. Sulfate attack of cementitious materials: volumetric relations and expansions, NISTIR 5390 report, National Institute of Standards and Technology, USA.

COMSOL, 2016. Structural mechanics module. User's guide.

Constantinides G, Ulm F-J, 2004. The effect of two types of C-S-H on the elasticity of cement-based materials: Results from nanoindentation and micromechanical modeling. Cement and Concrete Research 34, 67–80.

Costa A, Appleton J, 1999. Chloride penetration into concrete in marine environment – Part I: Main parameters affecting chloride penetration. Materials and Structures 32, 252–259.

Cuomo M, Nicolosi A, 2006. A poroplastic model for hygro-chemo-mechanical damage of concrete. EURO-C (Computational modelling of concrete structures Conference), Mayrhofen, Austria, 533–542. Available at: https://hal.archives-ouvertes.fr/file/index/docid/874433/filename/A_poroplastic_model_for_hygro-chemo-mechanical_damage_of_concrete.pdf

Dal Pont S, 2004. Lien entre la perméabilité et l'endommagement dans les bétons à haute temperature. PhD thesis. Ecole Nationale des Ponts et Chaussées, France. (In French.)

Damidot D, Glasser F P, 1992. Thermodynamic investigation of the $CaO–Al_2O_3–CaSO_4–H_2O$ system at 50 °C and 85 °C. Cement and Concrete Research 22, 1179–1191.

Djerbi A, Bonnet S, Khelidj A, Baroghel-Bouny V, 2008. Influence of traversing crack on chloride diffusion into concrete. Cement and Concrete Research 38, 877–883.

Djerbi Tegguer A, Bonnet S, Abdelhafid K, Baroghel-Bouny V, 2013. Effect of microcracking on gas permeability and chloride diffusion of concrete. Proceedings of 8th International Conference on Fracture Mechanics of Concrete and Concrete Structures, FraMCoS-8, Toledo, Spain, 10–14 March 2013.

Elfwing M, Evins L Z, Gontier M, Grahm P, Mårtensson P, Tunbrant S, 2013. SFL concept study. Main report. SKB TR-13-14, Svensk Kärnbränslehantering AB.

Faucon P, Le Bescop P, Adenot F, Bonville P, Jacquinot J F, Pineau F, Felix B, 1996. Leaching of cement: Study of the surface layer. Cement and Concrete Research 26, 1707–1715.

Flatt R J, Scherer G W, 2008. Thermodynamics of crystallization stresses in DEF. Cement and Concrete Research 38, 325–336.

Fälth B, Gatter P, 2009. Mechanical and thermo-mechanical analyses of the tapered plug for plugging of deposition tunnels. A feasibility study. SKB R-09-33, Svensk Kärnbränslehantering AB.

Gabet T, Malécot Y, Daudeville L, 2008. Triaxial behaviour of concrete under high stresses: influence of the loading path on compaction and limit states. Cement and Concrete Research 38, 403–412.

Galíndez J M, Molinero J, 2010. Assessment of the long-term stability of cementitious barriers of radioactive waste repositories by using digital-image-based microstructure generation and reactive transport modelling. Cement and Concrete Research 40, 1278–1289.

Gawin D, Alonso C, Andrade C, Majorana C, Pesavento F, 2005. Effect of damage on permeability and hygro-thermal behaviour of HPCs at elevated temperatures: Part 1. Experimental results. Computers and Concrete 2, 189–202.

Gawin D, Pesavento F, Schrefler B, 2006. Hygro-thermo-chemo-mechanical modelling of concrete at early ages and beyond. Part II: Shrinkage and creep of concrete. International Journal for Numererical Methods in Engineering 32, 332–363.

Gawin D, Pesavento F, Schrefler B A, 2008. Modeling of cementitious materials exposed to isothermal calcium leaching, considering process kinetics and advective water flow. Part 1: Theoretical model. International Journal of Solids and Structures 45, 6221–6240.

Gérard B, Pijaudier-Cabot G, Laborderie C, 1998. Coupled diffusion-damage modelling and the implications on failure due to strain localization. International Journal of Solids and Structures 35, 4107–4120.

Gérard B, Le Bellégo C, Bernard O, 2002. Simplified modelling of calcium leaching of concrete in various environments. Materials and Structures 35, 632–640.

Grahm P, Luterkort D, Mårtensson P, Nilsson F, Nyblad B, Oxfall M, Stojanovic B, 2013. SFL Concept study. Technical design and evaluation of potential repository concepts for long-lived low and intermediate level waste. SKB R-13-24, Svensk Kärnbränslehantering AB.

Grandia F, Galíndez J-M, Arcos D, Molinero J, 2010a. Quantitative modelling of the degradation processes of cement grout. Project CEMMOD. SKB TR-10-25, Svensk Kärnbränslehantering AB.

Grandia F, Galíndez J-M, Molinero J, Arcos D, 2010b. Evaluation of low-pH cement degradation in tunnel plugs and bottom plate systems in the frame of SR-Site. SKB TR-10-62, Svensk Kärnbränslehantering AB.

Haecker C-J, Garboczi E J, Bullard J W, Bohn R, Sun Z, Shah S, Voigt T, 2005. Modeling the linear elastic properties of Portland cement paste. Cement and Concrete Research 35, 1948–1960.

Haga K, Shibata M, Hironaga M, Tanaka S, Nagasaki S, 2005. Change in pore structure and composition of hardened cement paste during the process of dissolution. Cement and Concrete Research 35, 943–950.

Hakami E, Fredriksson A, Lanaro F, Wrafter J, 2008. Rock mechanics Laxemar. Site descriptive modelling, SDM-Site Laxemar. SKB R-08-57, Svensk Kärnbränslehantering AB.

Heukamp F H, Ulm F-J, Germaine J T, 2005. Does calcium leaching increase ductility of cementitious materials? Evidence from direct tensile tests. Journal of Materials in Civil Engineering 17, 307–312.

Hu D, Zhou H, Zhang F, Shao J, 2014. Modeling of short- and long-term chemomechanical coupling behavior of cement-based materials. Journal of Engineering Mechanics 140, 206–218.

Höglund L O, 2001. Project SAFE. Modelling of long-term concrete degradation processes in the Swedish SFR repository. SKB R-01-08, Svensk Kärnbränslehantering AB.

Höglund L O, 2014. The impact of concrete degradation on the BMA barrier functions report. SKB R-13-40, Svensk Kärnbränslehantering AB.

Idiart A, Shafei B, 2019. Modelling of concrete degradation – Hydro-chemical processes. Report for the safety evaluation SE-SFL. SKB R-19-11, Svensk Kärnbränslehantering AB.

Idiart A E, López C M, Carol I, 2011. Chemo-mechanical analysis of concrete cracking and degradation due to external sulfate attack: a meso-scale model. Cement and Concrete Composites 33, 411–423.

Ismail M, Toumi A, François R, Gagné R, 2008. Effect of crack opening on the local diffusion of chloride in cracked mortar samples. Cement and Concrete Research 38, 1106–1111.

Jacques D, 2009. Benchmarking of the cement model and detrimental chemical reactions including temperature dependent parameters. Project near surface disposal of category A waste at Dessel. NIRAS-MP5-03 DATA-LT(NF). NIROND-TR 2008–30 E, ONDRAF, Belgium.

Jiang F, Speziale S, Duffy T S, 2006. Single-crystal elasticity of brucite, $Mg(OH)_2$, to 15 GPa by Brillouin scattering. American Mineralogist 91, 1893–1900.

Jirásek M, 2011. Damage and smeared crack models. In Hofstetter G, Meschke G (eds). Numerical modeling of concrete cracking. Vienna: Springer, 1–49.

Kachanov L M, 1958. Time of the rupture process under creep conditions. Izvestiia Akademii Nauk SSSR, Otdelenie Teckhnicheskikh Nauk 8, 26–31.

Kalinowski B E (ed), 2009. Background complementary hydrogeochemical studies. Site descriptive modelling SDM-Site Laxemar. SKB R-08-111, Svensk Kärnbränslehantering AB.

Kormeling H A, Reinhardt H W, 1983. Determination of the fracture energy of normal concrete and epoxy modified concrete. Report 5-83-18, Delft University of Technology, The Netherlands.

Kuhl D, Bangert F, Meschke G, 2004. Coupled chemo-mechanical deterioration of cementitious materials. Part I: Modeling. International Journal of Solids and Structures 41, 15–40.

Kupfer H, Hilsdorf H K, Rusch H, 1969. Behavior of concrete under biaxial stresses. Journal of the American Concrete Institute 66, 656–666.

Lacarrière L, Sellier A, Bourbon X, 2006. Concrete mechanical behaviour and calcium leaching weak coupling. European Journal of Environmental and Civil Engineering 10, 1147–1175.

Lagerblad B, 1999. Long term test of concrete resistance against sulphate attack. In Marchand J, Skalny J P (eds). Materials science of concrete: sulphate attack mechanisms. Westerville, OH: The American Ceramic Society, 325–336.

Lagerblad B, Trägårdh J, 1994. Conceptual model for concrete long time degradation in a deep nuclear waste repository. SKB TR 95-21, Svensk Kärnbränslehantering AB.

Le Bellégo C, Pijaudier-Cabot G, Gérard B, Dubé J-F, Molez L, 2003. Coupled mechanical and chemical damage in calcium leached cementitious structures. Journal of Engineering Mechanics 129, 333–341.

Le Bescop P, Solet C, 2006. External sulphate attack by ground water. Experimental study on CEM I cement pastes. Revue Européenne de Génie Civil 10, 1127–1145.

Liu Q, Li L, Easterbrook D, Yang J, 2012. Multi-phase modelling of ionic transport in concrete when subjected to an externally applied electric field. Engineering Structures 42, 201–213.

Lothenbach B, Matschei T, Möschner G, Glasser F, 2008. Thermodynamic modelling of the effect of temperature on the hydration and porosity of Portland cement. Cement and Concrete Research 38, 1–18.

Lothenbach B, Bary B, Le Bescop P, Schmidt T, Leterrier N, 2010. Sulfate ingress in Portland cement. Cement and Concrete Research 40, 1211–1225.

Lothenbach B, Kunther W, Idiart A, 2012. Thermodynamic modeling of sulfate interaction. In Moyo P (ed). 3rd International Conference on Concrete Repair, Rehabilitation and Retrofitting, ICCRRR-3, Cape Town, South Africa, 3–5 September 2012. Leiden, The Netherlands: CRC Press, 1444–1449.

Lund B, Schmidt P, Hieronymus C, 2009. Stress evolution and fault stability during the Weichselian glacial cycle. SKB TR-09-15, Svensk Kärnbränslehantering AB.

Malan D F, 2012. Manuel Rocha medal recipient simulating the time-dependent behaviour of excavations in hard rock. Rock Mechanics and Rock Engineering 35, 225–254.

Malm M, 2012. Low-pH concrete plug for sealing the KBS-3V deposition tunnels. SKB R-11-04, Svensk Kärnbränslehantering AB.

Mas Ivars D, Veiga Rios M, Shiu W, Johansson F, Fredriksson A, 2014. Long term stability of rock caverns BMA and BLA of SFR, Forsmark. SKB R-13-53, Svensk Kärnbränslehantering AB.

Mazars J, 1986. A description of micro- and macroscale damage of concrete structures. Engineering Fracture Mechanics 25, 729–737.

Mazars J, Hamon F, Grange S, 2015. A new 3D damage model for concrete under monotonic, cyclic and dynamic loadings. Materials and Structures 48, 3779–3793.

Mehta P K, Monteiro P J M, 2006. Concrete: microstructure, properties, and materials. 3rd ed. New York: McGraw-Hill.

Moon J, 2013. Experimental and theoretical studies on mechanical properties of complex oxides in concrete. PhD thesis. University of California, Berkeley, California.

Moon J, Yoon S, Wentzcovitch R M, Monteiro P J, 2014. First-principles elasticity of monocarbo-aluminate hydrates. American Mineralogist 99, 1360–1368.

Mori T, Tanaka K, 1973. Average stress in matrix and average elastic energy of materials with misfitting inclusions. Acta Metallurgica 21, 571–574.

Nardi A, Idiart A, Trinchero P, de Vries L M, Molinero J, 2014. Interface COMSOL-PHREEQC (iCP), an efficient numerical framework for the solution of coupled multiphysics and geochemistry. Computers & Geosciences 69, 10–21.

Neville A M, 2004. The confused world of sulfate attack on concrete. Cement and Concrete Research 34, 1275–1296.

Nguyen T Q, Baroghel-Bouny V, Dangla P, 2006. Prediction of chloride ingress into saturated concrete on the basis of a multi-species model by numerical calculations. Computers and Concrete 3, 401–422.

Nguyen V, Colina H, Torrenti J, Boulay C, Nedjar B, 2007a. Chemo-mechanical coupling behaviour of leached concrete. Part I: Experimental results. Nuclear Engineering and Design 237, 2083–2089.

Nguyen V H, Nedjar B, Torrenti J M, 2007b. Chemo-mechanical coupling behaviour of leached concrete: Part II: Modelling. Nuclear Engineering and Design 237, 2090–2097.

Odler I, Colán-Subauste J, 1999. Investigations on cement expansion associated with ettringite formation. Cement and Concrete Research 29, 731–735.

Peerlings R H J, de Borst R, Brekelmans W A M, de Vree J H P, 1996. Gradient-enhanced damage for quasi-brittle materials. International Journal for Numerical Methods in Engineering 39, 3391–3403.

Pękala M, Olmeda J, Grivé M, Bruno J, 2015. Assessment of redox state and its impact on the solubility and speciation of selected radionuclides in the SFL repository. Final report. Amphos 21. SKBdoc 1533627 ver 1.0, Svensk Kärnbränslehantering AB.

Piasta W G, Schneider U, 1992. Deformations and elastic modulus of concrete under sustained compression and sulphate attack. Cement and Concrete Research 22, 149–158.

Picandet V, 2001. Influence d'un endommagement mécanique sur la permeabilité et sur la diffusivité hydrique des bétons. PhD thesis. Université de Nantes, France. (In French.)

Pichler B, Scheiner S, Hellmich C, 2008. From micron-sized needle-shaped hydrates to meter-sized shotcrete tunnel shells: micromechanical upscaling of stiffness and strength of hydrating shotcrete. Acta Geotechnica 3, 273–294.

Pijaudier-Cabot G, Mazars J, 2001. Damage models for concrete. In Lemaitre J (ed). Handbook of materials behavior models. Vol. 2, Failure of materials. San Diego, CA: Academic Press, 500–512.

Sanahuja J, Dormieux L, Chanvillard G, 2007. Modelling elasticity of a hydrating cement paste. Cement and Concrete Research 37, 1427–1439.

Santhanam M, 2011. Effect of solution concentration on the attack of concrete by combined sulphate and chloride solutions. European Journal of Environmental and Civil Engineering 15, 1003–1015.

Santhanam M, Cohen M D, Olek J, 2002. Mechanism of sulfate attack: a fresh look. Part 1: Summary of experimental results. Cement and Concrete Research 32, 915–921.

Schmidt T, 2010. Sulfate attack and the role of internal carbonate on the formation of thaumasite. PhD thesis. EPFL, Lausanne, Switzerland.

Scholtzová E, Tunega D, Speziale S, 2015. Mechanical properties of ettringite and thaumasite – DFT and experimental study. Cement and Concrete Research 77, 9–15.

Sellier A, Buffo-Lacarrière L, El Gonnouni M, Bourbon X, 2011. Behavior of HPC nuclear waste disposal structures in leaching environment. Nuclear Engineering and Design 241, 402–414.

Sidborn M, Marsic N, Crawford J, Joyce S, Hartley L, Idiart, A, de Vries L M, Maia F, Molinero J, Svensson U, Vidstrand P, Alexander R, 2014. Potential alkaline conditions for deposition holes of a repository in Forsmark as a consequence of OPC grouting. Revised final report after review. SKB R-12-17, Svensk Kärnbränslehantering AB.

Simone A, 2007. Explicit and implicit gradient-enhanced damage models. Revue Européenne de Génie Civil 11, 1023–1044.

Skalny J, Marchand J, Odler I, 2002. Sulfate attack on concrete. London: Spon Press.

SKB, 2006. Climate and climate related issues for the safety assessment SR-Can. SKB TR-06-23, Svensk Kärnbränslehantering AB.

SKB, 2008. Site description of Forsmark at completion of the site investigation phase. SDM-Site Forsmark. SKB TR-08-05, Svensk Kärnbränslehantering AB.

SKB, 2009. Site description of Laxemar at completion of the site investigation phase. SDM-Site Laxemar. SKB TR-09-01, Svensk Kärnbränslehantering AB.

Stora E, 2007. Multi-scale modelling and simulations of the chemo–mechanical behavior of degraded materials. PhD thesis. University of Paris-Est Marne-la-Vallée, France.

Stora E, Bary B, He Q-C, Deville E, Montarnal P, 2009. Modelling and simulations of the chemo–mechanical behaviour of leached cement-based materials: Leaching process and induced loss of stiffness. Cement and Concrete Research 39, 763–772.

Stora E, Bary B, He Q-C, Deville E, Montarnal P, 2010. Modelling and simulations of the chemomechanical behaviour of leached cement-based materials: Interactions between damage and leaching. Cement and Concrete Research 40, 1226–1236.

Tennis P D, Jennings H M, 2000. A model for two types of calcium silicate hydrate in the microstructure of Portland cement pastes. Cement and Concrete Research 30, 855–863.

Tixier R, Mobasher B, 2003. Modeling of damage in cement-based materials subjected to external sulfate attack. I: Formulation. II: Comparison with experiments. Journal of Materials in Civil Engineering 15, 305–322.

Torrenti J M, Nguyen V H, Colina H, Le Maou F, Benboudjema F, Deleruyelle F, 2008. Coupling between leaching and creep of concrete. Cement and Concrete Research 38, 816–821.

Torres S M, Lynsdale C J, Swamy R N, Sharp J H, 2003. Thaumasite formation in limestone filler cement mortar under sulfate and chloride exposure. International Seminar on the thaumasite form of sulfate attack of concrete, University of Sheffield, United Kingdom, 24 June 2003. Available at: https://www.sheffield.ac.uk/polopoly_fs/1.142966!/file/08.pdf

Travis Q B, Mobasher B, 2010. Correlation of elastic modulus and permeability in concrete subjected to elevated temperatures. Journal of Materials in Civil Engineering 22, 735–740.

Wang K, Jansen D C, Shah S P, Karr A F, 1997. Permeability study of cracked concrete. Cement and Concrete Research 27, 381–393.

Wardeh G, Mohamed M, Ghorbel E, 2011. Analysis of concrete internal deterioration due to frost action. Journal of Building Physics 35, 54–82.

Yang C C, Huang R, Yeih W, Sue I C, 1995. Aggregate effect on elastic moduli of cement-based composite materials. Journal of Marine Science and Technology 3, 5–10.

Yokozeki K, Watanabe K, Sakata N, Otsuki N, 2004. Modeling of leaching from cementitious materials used in underground environment. Applied Clay Science 26, 293–308.

Zhang M, Chen J, Lv Y, Wang D, Ye J, 2013. Study on the expansion of concrete under attack of sulfate and sulfate–chloride ions. Construction and Building Materials 39, 26–32.

Zheng J-J, Wong H S, Buenfeld N R, 2009. Assessing the influence of ITZ on the steady-state chloride diffusivity of concrete using a numerical model. Cement and Concrete Research 39, 805–813.

Zheng Q-S, Du D-X, 2001. An explicit and universally applicable estimate for the effective properties of multiphase composites which accounts for inclusion distribution. Journal of the Mechanics and Physics of Solids 49, 2765–2788.

Živica V, Szabo V, 1994. The behaviour of cement composite under compression load at sulphate attack. Cement and Concrete Research 24, 1475–1484.

Zuquan J, Wei S, Yunsheng Z, Jinyang J, Jianzhong L, 2007. Interaction between sulfate and chloride solution attack of concretes with and without fly ash. Cement and Concrete Research 37, 1223–1232.

Appendix A

Elastic properties of cement hydrates

Table A-1. Chemical formula, molar volume and mechanical properties of the minerals included in the reactive transport model and homogenization scheme.

	Chemical Formula	Molar volume [1] (l/mol)	Bulk modulus (GPa)	Shear modulus (GPa)
Portlandite	$Ca(OH)_2$	0.033	40.0[2]	16.0[2]
CSHtob$_2$	$(CaO)_{0.83333}(SiO_2)(H_2O)_{1.3333}$	0.059		
High-density			7.7[2]	4.84[2]
Low-density			1.9[2]	1.21[2]
CSHjen	$(CaO)_{1.666667}(SiO_2)(H_2O)_{2.1}$	0.078		
High-density			18.9[2]	11.9[2]
Low-density			13.9[2]	8.75[2]
Ettringite	$Ca_6Al_2(SO_4)_3(OH)_{12}:26H_2O$	0.707	14.9[2]	8.96[2]
Monosulfoaluminate	$Ca_4Al_2(SO_4)(OH)_{12}:6H_2O$	0.359	40.0[2]	16.0[2]
HydrotalciteOH	$Mg_4Al_2(OH)_{14}:3H_2O$	0.220	18.9[2]	11.9[2]
HydrogarnetOH	$Ca_3Al_2(OH)_{12}$	0.150	14.9[3]	9.0[3]
Calcite	$CaCO_3$	0.037	69.8[2]	30.4[2]
Brucite	$Mg(OH)_2$	0.025	43.2[4]	35.2[4]
SiO2(am)	SiO_2	0.029	36.5[3]	31.2[3]
Hemicarboaluminate	$Ca_4Al_2(CO_3)_{0.5}(OH)_{13}:5.5H_2O$	0.285	15.0[5]	1.1[5]
Monocarboaluminate	$Ca_4Al_2(CO_3)(OH)_{12}:5H_2O$	0.262	56.2[6]	30.5[6]
Thaumasite	$(CaSiO_3)2(CaSO_4)2(CaCO_3)_2(H_2O)_{30}$	0.332	38.4[8]	14.5[8]
HydrogarnetSi	$Ca_3Al_2(SiO_4)_{0.8}(OH)_{8.8}$	0.143	14.9[3]	9.0[3]
HydrotalciteC	$Mg_4Al_2(OH)_{12}CO_3:3H_2O$	0.220	18.9[2]	11.9[2]

(1) Lothenbach et al. (2010).
(2) Bary et al. (2014).
(3) Haecker et al. (2005).
(4) Jiang et al. (2006).
(5) Moon (2013).
(6) Moon et al. (2014).
(7) Scholtzová et al. (2015).

Table A-2. Mechanical properties of the inert phases considered in the homogenization scheme.

	Bulk Modulus (GPa)	Shear Modulus (GPa)
Sand	35.9[1]	25.8[1]
Aggregates	33.33[2]	21.95[2]
Unhydrated Clinker	105.20[1]	44.80[1]

(1) Bary et al. (2014).
(2) Yang et al. (1995).

Appendix B

Homogenization model – implementation details

This appendix contains a more detailed description of the homogenization model in terms of unity volume fractions of the different constituents or phases at different scales of analysis.

B.1 Inner coating

As stated in Table 5-6, the volume fraction of C-S-H (initially given by the mineral CSHjen) in concrete is 0.0943 m^3_{CSH}/m^3_{conc}, and that the volume fraction of inclusions (i.e. all other cement hydrates) is 0.0916 $m^3_{other\ hydrates}/m^3_{conc}$. According to the hydration model of Tennis and Jennings (2000) for cement paste, 0.356 of the C-S-H gel corresponds to high-density C-S-H, which in this model is associated to the inner coating. Thus, the volume fraction of high-density (HD) CSHjen in concrete is 0.0943 m^3_{CSH}/m^3_{conc} ·0.356 $m^3_{CSH\_HD}/m^3_{CSH}$ = 0.0336 $m^3_{CSH\_HD}/m^3_{conc}$. This volume does not include gel pores, as it is calculated with the molar volumes of dried CSHjen and/or CSHtob2 (Table A-1). The C-S-H matrix of the inner layer is assumed to have a gel porosity of 0.26 (Bary et al. 2014). Therefore, the volume fraction of the C-S-H matrix of the inner coating in concrete including gel pores is:

$$\frac{0.0336}{1-0.26} = 0.0454\ \ m^3_{CSH\ matrix\_HD}/m^3_{conc}$$

It is considered in this model that the distribution of inclusions between high and low-density C-S-H matrices is the same as for CSHjen. Thus, 0.356 of the inclusions volume fraction is located to the inner coating (high-density C-S-H) and the remaining 0.644 in the outer coating. Therefore, the volume fraction of inner coating (IC) in concrete is:

$$0.0454 + 0.356 \cdot 0.0916 = 0.0781\ \ m^3_{IC}/m^3_{conc}$$

Thus, the inner coating has a volume fraction of C-S-H matrix of 0.0454/0.0781 = 0.582 $m^3_{CSH\ matrix\_HD}/m^3_{IC}$, of which 0.26 are gel pores (gp), yielding a volume fraction of 0.151 m^3_{gp}/m^3_{IC}. The remaining volume of the inner coating corresponds to other hydrates, with a volume fraction of 0.0418 $m^3_{other\ hydrates}/m^3_{IC}$.

B.2 Outer coating

The outer coating includes not only gel pores but also capillary pores. The volume fraction of low-density (LD) C-S-H in concrete, on the other hand, is 0.0943·0.644 = 0.0607 $m^3_{CSH\_LD}/m^3_{conc}$. The C-S-H matrix of the outer layer is assumed to have a gel porosity (gp) of 0.38 (Bary et al. 2014). Thus, the volume fraction of the C-S-H matrix of the outer coating in concrete including gel pores is:

$$\frac{0.0607}{1-0.38} = 0.0979\ \ m^3_{CSH\ matrix\_LD}/m^3_{conc}$$

There is a 0.0916·0.644 = 0.0589 $m^3_{other\ hydrates}/m^3_{conc}$ volume fraction of inclusions (i.e. other hydrates) embedded in this low-density C-S-H matrix. The total volume fraction of C-S-H and inclusions is thus 0.157. Low-density C-S-H is distributed between the outer layer (0.823) and the interfacial transition zone or ITZ (0.177), as detailed in Section B.3.

From Section 5.2, it is noted that the mortar volume fraction in concrete is 0.654 m^3_{mortar}/m^3_{conc} (Table 5-6), while the volume fraction of hardened cement paste (HCP) in mortar is 0.379 m^3_{HCP}/m^3_{mortar} (Table 5-5). In addition, the volume fraction of outer coating (OC) in HCP is 0.635 m^3_{OC}/m^3_{HCP} (see Section B.4). Consequently, HCP outer coating constitutes a 0.157 of the concrete volume.

The volume fraction of C-S-H matrix in outer coating (OC) is thus:

$$\frac{0.0979 \cdot 0.823}{0.157} = 0.511\ \ m^3_{CSH\ matrix\_LD}/m^3_{OC}$$

of which 0.38 is gel porosity (i.e. 0.194 m^3_{gp}/m^3_{OC}).

The volume fraction of inclusions in outer coating (OC), on the other hand, is:

$\frac{0.0589 \cdot 0.823}{0.157} = 0.308$ $m^3_{other\ hydrates}/m^3_{OC}$

Finally, the capillary porosity (cp) of the outer coating is

1.000–0.511–0.308 = 0.182 m^3_{cp}/m^3_{OC}.

B.3 ITZ

Following Bary et al. (2014), it is considered that the ITZ has a total porosity of 0.64. The volume fraction of low-density C-S-H with its inclusions in concrete is 0.157 m^3_{OC}/m^3_{conc} (Section B.2), while the volume fraction of the low-density C-S-H matrix only (without inclusions) is 0.0979 $m^3_{CSH\ matrix\_LD}/m^3_{conc}$. The volume fraction in ITZ of C-S-H matrix + inclusions, named *x* in the equation below, that yields a total porosity (φ_{tot}) of 0.64 can be calculated with the following expression:

$$\varphi_{tot} = 0.64 = \varphi_{cp} + \varphi_{gp} = (1 - x) + x \cdot 0.38 \cdot \frac{0.0979}{0.157}$$

Solving for *x* yields a value of 0.472. The volume fraction of capillary pores is the remaining volume, that is, 0.528 m^3_{cp}/m^3_{ITZ}. The volume fraction of C-S-H matrix in the ITZ is 0.472·0.0979/0.157 = 0.294 $m^3_{CSH\ matrix\_LD}/m^3_{ITZ}$, with 0.38 of gel porosity (0.112 $m^3_{gp\ matrix\_LD}/m^3_{ITZ}$). The volume fraction of inclusions, on the other hand, is 0.472–0.294 = 0.177 $m^3_{other\ hydrates}/m^3_{ITZ}$.

From Section 5.2, it is noted that the mortar volume fraction in concrete is 0.654 m^3_{mortar}/m^3_{conc} (Table 5-6), while the volume fraction of ITZ in mortar is 0.09 m^3_{ITZ}/m^3_{mortar} (Table 5-5). In turn, 0.472 of the ITZ volume fraction is constituted by C-S-H plus other hydrates (inclusions). Therefore, the fraction of the low-density C-S-H matrix, with inclusions, that corresponds to the ITZ is:

$\frac{0.654 \cdot 0.09 \cdot 0.472}{0.157} = 0.177$

The remaining 0.823 corresponds to the outer coating of HCP (Section B.2).

B.4 HCP

The cement hydration model developed by Tennis and Jennings (2000), assuming a water-to-cement ratio of 0.47 (Höglund 2001) gives a volume fraction of unhydrated clinker (UC) in HCP of 0.0494 m^3_{UC}/m^3_{HCP}. The volume fraction of inner coating (IC) in concrete is 0.0781 m^3_{IC}/m^3_{conc} (Section B.1), while 0.654 of concrete is mortar (Table 5-6), and 0.379 of the mortar is HCP (Table 5-5). With these data, the volume fraction of inner coating in HCP is calculated as:

$\frac{0.0781}{0.654 \cdot 0.379} = 0.315$ m^3_{IC}/m^3_{HCP}

The remaining volume fraction corresponds to outer coating: 1.000–0.0494 – 0.315 = 0.636 m^3_{OC}/m^3_{HCP}.

Gel porosity is calculated from both the inner and outer coatings, using the volume fraction of C-S-H matrix obtained for each coating (see Table 5-1 and Table 5-2). This yields:

$0.26 \cdot 0.315 \cdot 0.582 + 0.38 \cdot 0.636 \cdot 0.511 = 0.171$ m^3_{gp}/m^3_{HCP}

Capillary porosity is only part of the outer coating:

$0.636 \cdot 0.182 = 0.116$ m^3_{cp}/m^3_{HCP}

which yields a total porosity of HCP of 0.287 $m^3_{tot\ porosity}/m^3_{HCP}$.

Appendix C

Saturation indices for groundwater and concrete porewater

Saturation indices for meteoric groundwater and concrete porewater compositions used in the BHK vault simulations are given in the table below, together with the equilibrium constant of the mineral (log K) and its chemical formula.

Mineral	Saturation indices for groundwater	Saturation indices for concrete porewater	log K	Dissolution reactions used to calculate solubility products log K
Brucite	–3.56	–0.17	16.84	$Mg(OH)2$
Calcite	0.12	–0.30	1.85	$CaCO_3 \rightarrow Ca^{2+} – H^+ + HCO^{3–}$
CSH_{jen}	–10.15	0.00	–13.16	$(CaO)_{1.6667}(SiO_2)(H_2O)_{2.1} \rightarrow 1.6667Ca^{2+} + SiO(OH)_3^- + 2.3333OH^- – 0.5667\ H_2O$
CSH_{tob2}	–3.50	–0.83	–8.00	$(CaO)_{0.8333}\ (SiO_2)(H_2O)_{1.3333} \rightarrow 0.8333Ca^{2+} + SiO(OH)_3^- + 0.6667OH^- – 0.5H_2O$
Ettringite	–20.43	0.00	–44.84	$Ca_6Al_2(SO_4)_3(OH)_{12}{\cdot}26H_2O \rightarrow 6Ca^{2+} + 2Al(OH)_4^- + 3SO_4^{2–} + 4OH^- + 26H_2O$
Gypsum	–2.48	–1.60	–4.58	$CaSO_4{\cdot}2H_2O \rightarrow Ca^{2+} + SO_4^{2–} + 2H_2O$
Hemicarboaluminate	–26.22	–4.14	–29.12	$Ca_4Al_2(CO_3)_{0.5}(OH)_{13}{\cdot}5.5H_2O \rightarrow 4Ca^{2+} + 2Al(OH)_4^- + 0.5CO_3^{2–} + 5OH^- + 5.5H_2O$
Hydrogarnet OH	–23.24	–5.43	–20.84	$Ca_3Al_2(OH)_{12} \rightarrow 3Ca^{2+} + 2Al(OH)_4^- + 4OH^-$
Hydrogarnet Si	–13.97	0.00	–29.87	$Ca_3Al_2(SiO_4)_{0.8}(OH)_{8.8} + 2.4H_2O \rightarrow 3Ca^{2+} + 2Al(OH)_4^- + 0.8\ SiO(OH)_3^- + 3.2OH^-$
Hydrotalcite C	–3.50	–8.48	–51.14	$Mg_4Al_2(OH)_{12}CO_3{\cdot}3H_2O \rightarrow 4Mg^{2+} + 2Al(OH)_4^- + CO_3^{2–} + 4OH^- + 3H_2O$
Hydrotalcite OH	–4.43	0.00	–56.02	$Mg_4Al_2(OH)_{14}{\cdot}3H_2O \rightarrow 4Mg^{2+} + 2Al(OH)_4^- + 6OH^- + 3H_2O$
Monocarboaluminate	–20.98	–3.60	–31.46	$Ca_4Al_2(CO_3)(OH)_{12}{\cdot}5H_2O \rightarrow 4Ca^{2+} + 2Al(OH)_4^- + CO_3^{2–} + 4OH^- + 5H_2O$
Monosulfoaluminate	–21.91	–3.21	–29.24	$Ca_4Al_2(SO_4)(OH)_{12}{\cdot}6H_2O \rightarrow 4Ca^{2+} + 2Al(OH)_4^- + SO_4^{2–} + 4OH^- + 6H_2O$
Portlandite (CH)	–8.98	0.00	22.81	$Ca(OH)_2 \rightarrow Ca^{2+} – 2H^+ + 2H_2O$
SiO_2 am	–1.17	–5.98	1.48	$SiO_2 + 1OH^- + 1H_2O \rightarrow SiO(OH)_3^-$
Thaumasite	–9.22	0.00	–49.36	$Ca_6(SiO_3)_2(SO_4)_2(CO_3)_2{\cdot}30H_2O \rightarrow 6Ca^{2+} + 2H_3SiO_4^- + 2SO_4^{2–} + 2CO_3^{2–} + 2OH^- + 26H_2O$

Arkitektkopia AB, Bromma, 2019

SKB is responsible for managing spent nuclear fuel and radioactive waste produced by the Swedish nuclear power plants such that man and the environment are protected in the near and distant future.

skb.se